ACTA UNIVERSITATIS UPSALIENSIS
Uppsala Dissertations from the Faculty of Science
24

PRODUCTION OF HEAVY HYPERNUCLEI IN ANTIPROTON ANNIHILATION – STUDY OF THEIR DECAY IN THE FISSION CHANNEL

by
Göran Ericsson
CERN LIBRARIES, GENEVA

UPPSALA 1988

ACTA UNIVERSITATIS UPSALIENSIS
Uppsala Dissertations from the Faculty of Science
24

PRODUCTION OF HEAVY HYPERNUCLEI IN ANTIPROTON ANNIHILATION – STUDY OF THEIR DECAY IN THE FISSION CHANNEL

by

Göran Ericsson

UPPSALA 1988

Doctoral thesis at Uppsala University, 1988
ISSN 0346-6485
ISBN 91-554-2301-9

ABSTRACT

Ericsson, G., 1988, Production of heavy hypernuclei in antiproton annihilation – study of their decay in the fission channel. Acta Univ. Ups., *Uppsala Dissertations from the Faculty of Science* 24, 170 pp. Uppsala. ISBN 91-554-2301-9.

A strange lambda-particle bound to an atomic nucleus forms a so called hypernucleus. The introduction of a new kind of particle in addition to the ordinary protons and neutrons in the nucleus gives a unique possibility to study many effects connected both to the surrounding nuclear medium and to the lambda-particle itself. This thesis presents the first experimental results on the lifetimes of hypernuclei in the mass region of bismuth and uranium.

Antiprotons from the Low Energy Antiproton Ring at CERN, Geneva, were brought to rest in thin targets of ^{209}Bi and ^{238}U where they annihilated. A detector system, designed according to the so called recoil-distance technique, recorded the positions of single and coincident heavy fragments emitted in the annihilation reactions. By a careful selection procedure, clean samples of fission events were selected. The geometrical arrangement of the detectors made a clear separation of prompt and delayed fission events possible. A delayed fission activity, with a yield of $2 - 6 \cdot 10^{-4}$ per stopped antiproton was observed, both with bismuth and uranium targets. Using the least-squares method, the lifetimes for the delayed fission activity were found to be $(0.24\ ^{+0.06}_{-0.05} \pm 0.02)$ ns and $(0.120\ ^{+0.025}_{-0.020} \pm 0.020)$ ns for bismuth and uranium, respectively. Because of the yields, the lifetimes, the high-energy mode of fission and the fact that delayed fission activity was found for both targets, the observation was interpreted as the formation and decay of heavy hypernuclei. The results obtained in this experiment are compared to predictions made in theoretical studies and also to previous measurements on light hypernuclear systems.

An analysis of the antiproton induced, prompt fission events shows that modern intranuclear-cascade calculations are well suited to describe the gross features of antiproton annihilation on complex nuclei. The fission probabilities in antiproton annihilation were found to be 0.116 ± 0.017 and 1.15 ± 0.17 for ^{209}Bi and ^{238}U, respectively.

Göran Ericsson, Department of Radiations Sciences, Uppsala University, Box 535, S-751 21 Uppsala, Sweden

Printed in Sweden 1988 by Graphic Systems AB, Göteborg 1988

To my Parents

Karin and Göte

PS177 Collaboration

Centre d'Etudes Nucléaires de Grenoble, BP 85X, F-38041 Grenoble Cedex, France
J.P. BOCQUET
M. MAUREL
E. MONNAND
H. NIFENECKER
P. PERRIN
C. RISTORI

Centre d'Etudes Nucléaires de Saclay, F-91191 Gif-sur-Yvette, France
J. MOUGEY

Department of Radiation Sciences, P.O. Box 535, S-751 21 Uppsala, Sweden
G. ERICSSON
T. JOHANSSON
G. TIBELL

GSI, Postfach 110541, D-06100 Darmstadt, Fed. Rep. Germany
S. POLIKANOV

Laboratoire René Bernas du CSNSM, BP 1, F-91406 Orsay, France
M. EPHERRE-REY-CAMPAGNOLLE

NIKHEF, P.O.Box 4395, NL-1009 AJ Amsterdam, The Netherlands
J. KONIJN

Warsaw University, Branch in Bialystok, PL-15-424 Bialystok, Poland
T. KROGULSKI

CONTENTS

Chapter 1 : INTRODUCTION.

A dominating part of our knowledge of atomic nuclei comes from accelerator based research. The results of experiments concerning various aspects of the behaviour of nuclei and nuclear constituents are essential for the development of nuclear theory and the models which can be conceived from such a theory. Using the models one can hopefully predict the outcome of future experimental studies. If a model does not stand the test of a particular study, it has to be changed within the limits of the underlying theoretical basis. Even the basis has to be modified at times, now within the limitations of the still more fundamental laws of nature.

For the understanding of the properties of nuclei it is of course essential to know the characteristics of their constituents, the nucleons, i.e., protons and neutrons. However, it does not seem possible to predict the exact behaviour of nuclei from the properties of individual nucleons. The interactions between two constituents change in the presence of other nucleons.

Many-body forces come into play, and it has been fruitful for the description of nuclei to represent the medium by some potential, like is done in the nuclear shell model, for instance.

On the other hand, it does not seem necessary to include all the collected knowledge about the nucleons into nuclear models. To mention one example, it has so far been difficult to find any clear cut case where the fact that nucleons are in turn made of quarks and gluons plays any essential rôle in a model intended for describing nuclear behaviour.

Technical innovations hold an important position in the continuing dialogue between theory and experiment. As higher particle energies are attained new thresholds for particle production can be reached. Higher particle intensities make possible studies of reactions with very low probabilities and greater precision gives more detailed results, just to mention a few obvious examples.

Accelerators which give access to a new kind of probes of nuclei belong to the category of technical innovations with which new approaches may be made. Storage rings, equipped with cooling facilities are yet another means of progress in this respect. For these reasons it was very important that at CERN, the European Organization for Nuclear Research, a new facility was put at the disposal of experimental nuclear and particle physics. This storage ring, the Low Energy Antiproton Ring (LEAR), had many

interesting features. It stored antiprotons which could either be accelerated to energies which were high enough to produce new particles or decelerated to low energies for experiments using stopped antiprotons. In addition, the improvement in energy resolution, brought about by the cooling device, made it possible to increase the stop rate also in very thin targets.

These features were crucial for the decision to propose the experiment presented here. This project, the 177:th experiment to be accepted by the CERN committee for the Proton Synchrotron facilities, was given the name PS177. This name will sometimes be used in this thesis which contains the following main parts.

Chapter 1 is an introduction and also gives the outline of this thesis.

Chapter 2 gives a short description of the physics involved. The main part is devoted to hypernuclear physics, and in particular to the present knowledge, both experimental and theoretical, concerning hypernuclear lifetimes. Some physics aspects of antiproton annihilation and nuclear fission are each given a shorter treatment. They are mainly used as tools in the present study. This chapter should not be considered as a part of the work done by this author. It is included to give the reader part of the necessary background.

Chapter 3 gives the detailed design of the experimental apparatus. Parts describing the experimental technique, the data acquisition system and the electronics are also included.

The performance of the various parts of the detector system is treated in chapter 4. The response to different types of particles is discussed and in particular, the procedure to select fission events is carefully described.

The analysis of the experimental data is treated in some detail in chapter 5. Both delayed and prompt fission events were examined, and a set of new results could be extracted.

Chapter 6 gives a summary of the final results obtained in chapter 5 and discusses them in view of previous knowledge. The conclusions which can be drawn from these results are also given.

Three appendices are included. Appendix A is a summary of the least-squares method for parameter estimation. Many of the results obtained in this work rely on this method. Appendices B and C are reprints of two papers, published in Physics Letters, where the preliminary results of the PS177 experiment were presented for the first time.

Chapter 2 : PHYSICS BACKGROUND.

2.1 Antiproton-nucleus interactions.

Some of the basic properties of antiproton annihilation on complex nuclei are reviewed. Only aspects with relevance to this thesis are treated; in particular, the strangeness content of low-energy antiproton annihilation is given some attention.

2.1.1 Annihilation.

An antiproton stopped in a target will form an antiprotonic atom with one of the target nuclei. An electromagnetic cascade towards the atomic ground state is initiated, and when the overlap between the antiproton wave function and the nucleus becomes appreciable annihilation start to occur. This process is usually quite peripheral, taking place where the nuclear density is low. An example of the radial distribution of annihilation sites is shown in Fig. 2.1, taken from the calculation of Iljinov et al. (Ilj 82). By studying the charged particle multiplicity after annihilation at rest, it has been estimated that about 93% of all annihilations occur in a region where the nuclear density is less than 75% of its central value (Pir 86).

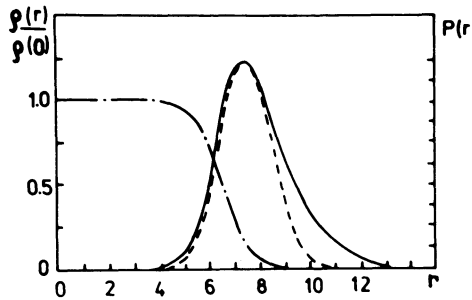

Fig. 2.1 The annihilation probability (solid and dashed curves) compared to the nuclear matter density (dot-dashed curve) for ^{208}Pb. From Ilj 82. The r-scale is in fm.

Due to their peripheral nature, most annihilations proceed through the elementary antiproton-nucleon interaction. This process is well studied for stopped antiprotons. More than 90% of the interactions lead to purely pionic final states, the number of pions ranging from 2 to 8 with a mean multiplicity of $\langle n \rangle_\pi \approx 5$ (Ghe 74). The energy of the pions is in general 100 - 300 MeV, i.e., in the region of the Δ-resonance. The next lightest type of meson, the strange kaon, is produced in about 7% of all annihilations at rest (Arm 69).

Many of the features of low-energy antiproton annihilation on complex nuclei can be explained as a succession of two-body interactions between the primary pions and the nucleons in the residual nucleus, as has been shown by many groups (see, e.g., Ilj 82, Clo 82 and Cug 85). The most important processes in such an intranuclear cascade (INC) are the formation and decay of the Δ as well as πN- and NN-scattering. Fig. 2.2 shows the nice agreement between such an INC calculation and the experimental momentum spectrum for pions and protons emitted in the annihilation of 608 MeV/c antiprotons on ^{238}U (McG 86). The two-bumped structure in the pion spectrum is well described by the model. The wide structure for momenta larger than about 300 MeV/c comes from non-interacting pions, directly produced in the annihilation on a nucleon on the nuclear surface. The narrow peak around 200 MeV/c is due to pions which have interacted with the residual nucleus and thereby transferred some of their energy.

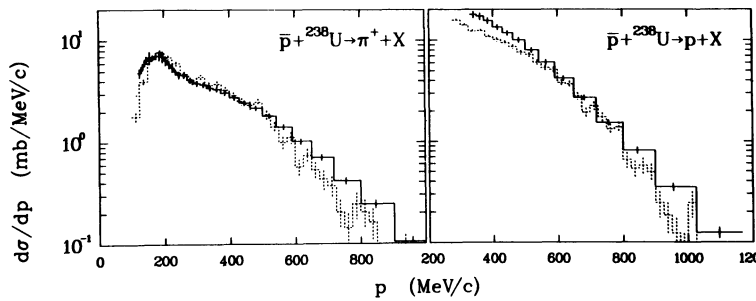

Fig. 2.2 : The inclusive momentum distributions for π^+ and protons from 608 MeV/c antiproton annihilations on ^{238}U. The solid histograms are the experimental data, the dashed histograms show the result of the INC calculation. From McG 86.

The scheme presented above indicates that, although the energy released in the annihilation is large, 1.88 GeV, only part of that will normally be transferred to the residual nucleus. Calculations have shown that for heavy nuclei, 0.4 - 1 GeV is transferred from the pion system (Clo 82, Cug 87b). The energy deposited decreases with the mass of the target nucleus and it is also strongly dependent on the position of the primary annihilation ; antiprotons which penetrate further into the nucleus will deposit more energy.

The different stages in the deexcitation of the residual nucleus are schematically shown in Fig. 2.3. The primary pions can induce direct knock-

out reactions whereby nucleons or nuclear clusters are emitted. The average energy of different light particles, emitted after antiproton annihilation, has been measured for a wide range of targets. The corresponding average momenta are almost independent of particle type and very close to the expected mean pion momentum (Egi 87). The deexcitation then proceeds through particle evaporation, where mostly neutrons but also some protons can be emitted. For heavy nuclei, decay through the fission channel is also possible. What is left are radioactive, neutron-deficient nuclei, distributed over a wide range in mass.

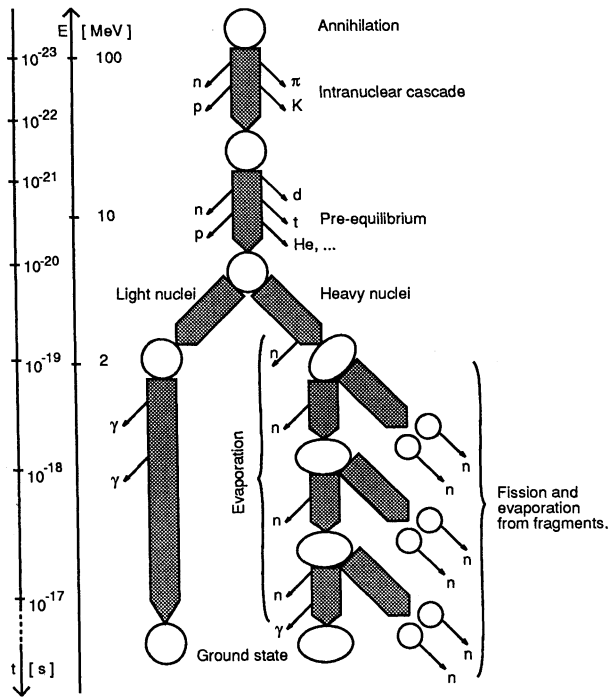

Fig 2.3 : Schematic picture of the different stages of nuclear deexcitation after antiproton annihilation on a complex nucleus. Note that the scales to the left are only very approximate.

Measurements of the gamma emission from the more long-lived nuclei (Mos 86, Egi 88) have shown that more than 30 nucleons may be emitted from ^{98}Mo and up to 50 from ^{165}Ho after the annihilation of stopped antiprotons. On average, about 10 - 20 nucleons are lost for these targets. The

experiments also include a study of the residual nuclei found after antiproton annihilation in ^{238}U. No nuclei with mass close to 238 were found, the range of nuclear masses being mainly from A = 97 to A = 126. The fission process is clearly dominant in this case. The mass yields in the case of ^{98}Mo have been satisfactorily explained using an INC approach in combination with a simple evaporation model (Cug 87b).

2.1.2 Strange particle production.

In the elementary $\bar{p}N$-reaction at rest, the only strange particles which can be produced are kaons, having a mass of about 495 MeV. They are produced in about 7% of all annihilations at rest (Arm 69).

However, it has been known for many years that low-energy antiproton annihilation on deuterium produces Λ-particles at a rate which exceeds what is expected from rescattering of the normal annihilation products (Roy 75). Some more recent experiments have confirmed this observation and also extended the measurements to heavier nuclei. For low-energy antiprotons, targets such as C, Ti, Ta and Pb (Con 84) and Ne (Bal 87) have given Λ-production rates close to 2%. An experiment with 4 GeV/c antiprotons impinging on Ta has given a similar result (Miy 84).

Naively, one might think that no hyperons could be produced in low-energy antiproton annihilation since the threshold momentum for the elementary process $\bar{p}\,p \rightarrow \bar{\Lambda}\,\Lambda$ is 1435 MeV/c. One approach to explain the enhanced Λ-production, studied by Mandelkern et al. (Man 83), has been to include the double-scattering of a $\bar{K}$, produced in the annihilation on a single nucleon. The calculation gives a large contribution from the double-scattering process but it still underestimates the Λ-production rate by a factor of two or so.

A quite different mechanism, namely the annihilation on more than one nucleon, was proposed by Rafelski (Raf 80) and has been studied in more detail by Cugnon and Vandermeulen (Cug 84). In this model, the encounter between the antiproton and a nucleon creates a fireball with baryon number B = 0 and with a short, but finite lifetime. This object may collide with other nucleons before decaying, thereby forming a $B \geq 1$ system. The calculation shows that the decay of the B = 1 fireball leads to an enhancement of the channels involving strangeness, and especially those with S = -1 baryons (Λ or Σ) produced in association with S = 1 kaons. Cugnon and Vandermeulen predict that 8.8% of all B = 1 annihilations will produce a hyperon. Using

this type of model in the analysis of antiproton-deuteron interactions, both for the Λ–production and the $\bar{p}\,d \rightarrow \pi^- p$ branching ratio, leads to a B = 1 rate of about 10% (Cug 84 and Gua 88).

One can conclude that, whatever the mechanism behind the large Λ-production, strangeness is clearly produced at significant rates in low-energy antiproton annihilations.

2.2 Hypernuclei.

2.2.1 Introduction.

A hypernucleus is an atomic nucleus where one or more nucleons have been replaced by one or more hyperons. The lightest hyperon is the neutral Λ -particle, with a mass of 1115.6 MeV, spin-parity $J^\pi = \frac{1}{2}^+$, isospin I = 0 and strangeness S = -1. Hypernuclei with a single Λ-particle attached to the nuclear core are those best studied so far, even though the field of Σ - hypernuclei has attracted quite some attention lately. Some observations of double-Λ hypernuclei have also been reported.

The notation used for hypernuclei follows the ordinary scheme. Hence, hypercarbon, ${}^{12}_{\Lambda}C$, consists of a Λ-particle bound to a nuclear core of 6 protons and 5 neutrons.

There are excellent reviews on the subject of hypernuclei : the series of articles written by B.Povh have been of great value to this author (See, e.g., Pov 87, Pov 88). The latest results in the field, both experimentally and theoretically, can be found in the proceedings of the 1986 INS International Symposium on Hypernuclear Physics (Ban 86) and the 1987 International Symposium on Strangeness in Hadronic Matter (Spe 88).

There are several reasons why hypernuclear physics is of interest. First, the introduction of the hyperon as a distinguishable probe into the nuclear medium offers the possibility to study the interactions of a single baryon with the remaining nucleons, without the complications introduced by the Pauli exclusion principle. Thus one can test models for nuclear structure, e.g., the shell model, even for the most deeply bound states.

Furthermore, direct scattering experiments on the low-energy hyperon-nucleon interaction are not easily performed and the study of hypernuclear systems has so far contributed most of the information on this topic. By investigating the properties of Λ -, Σ -, and in the future even Ξ - and Ω - hypernuclei, new knowledge on the fundamental baryon-baryon force can

be gained (Dov 82). The double-Λ hypernuclei even open up the possibility to investigate the Λ-Λ-interaction (See, e.g., Bod 87 and the review Bre 86).

Moreover, it has been suggested that hyperons in nuclei might reveal unique information about the effects of quark degrees of freedom on the nuclear physics level (Yam 87, Hay 88).

Finally, the Λ-hypernuclei present a good laboratory to test our understanding of the fundamental baryon-baryon weak interaction (Bar 86, Bar 88). This last topic has received renewed attention in the last few years, much as a consequence of the new, high-quality data available (see subsection 2.2.4 for a review of the experimental situation). It is the aim of the PS177 experiment to add some further information in this field.

2.2.2 Hypernuclear production.

In practice, there are two types of processes whereby strange baryons can be produced. The first is the so called associated production, in which pairs of particles with opposite strangeness are created :

$$\pi + N \rightarrow K + Y \qquad (2.1),$$
$$\gamma + N \rightarrow K + Y \qquad (2.2),$$

where N is a nucleon (n or p)
Y is a hyperon (Λ or Σ).

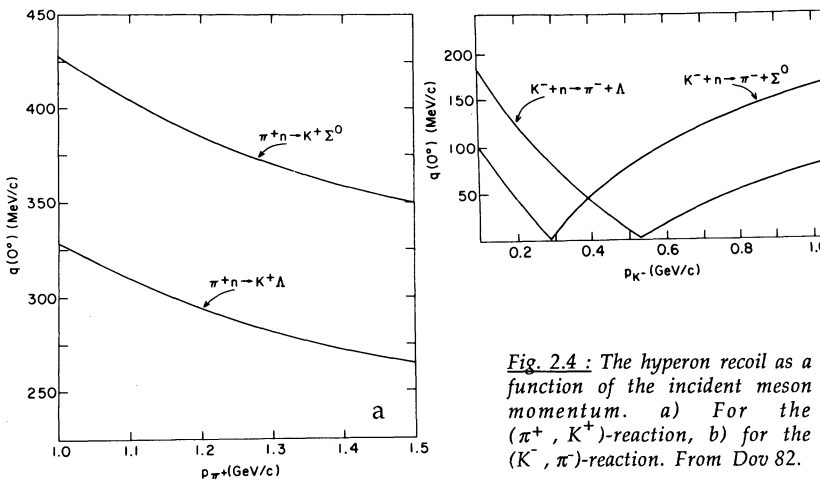

Fig. 2.4 : The hyperon recoil as a function of the incident meson momentum. a) For the (π^+ , K^+)-reaction, b) for the (K^- , π^-)-reaction. From Dov 82.

The second mechanism is the strangeness exchange reaction :

$$K + N \rightarrow \pi + Y \qquad (2.3).$$

This latter reaction has been extensively used in hypernuclear research (Wal 88), mainly through the process :

$$K^- + {}^{A}Z \rightarrow \pi^- + {}^{A}_{\Lambda}Z \qquad (2.4)$$

i.e., utilizing the elementary reaction

$$K^- + n \rightarrow \pi^- + \Lambda + 178\ [MeV] \qquad (2.5).$$

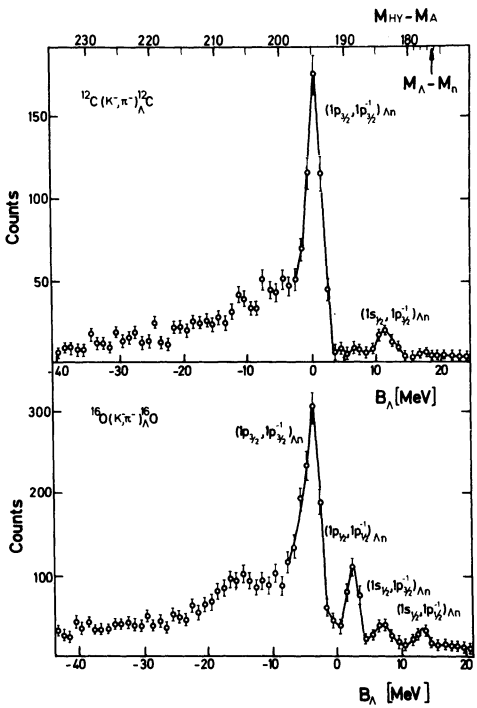

Fig. 2.5 : Production of the hypernuclei ${}^{12}_{\Lambda}C$ and ${}^{16}_{\Lambda}O$ through the (K^-, π^-)-reaction. The kaon momentum was 715 MeV/c. The shell model assignments are indicated for each peak. From Brü 78.

The exothermic process of eq. 2.5 possesses a very attractive kinematical property. Detecting the outgoing π^- at zero degrees in the laboratory, there exists a "magic" incident K^- momentum for which the Λ is produced with no recoil momentum. This recoil-less production is obtained for a K^-

momentum of 530 MeV/c. Even for momenta close to the "magic" 530 MeV/c (Fig. 2.4) and at higher angles for the π^-, the Λ recoil momentum remains very low.

In the recoil-less reaction the Λ is preferentially produced in so called substitutional states, with the Λ in the same orbital as the n it replaces. In the language of a Λ-hypernucleus shell model : the (K^-, π^-)-reaction at zero degrees populates mainly (Λ, n^{-1})-states with $\Delta L=0$. Detecting the outgoing π^- at higher angles makes it possible to select states with higher ΔL-values. Fig. 2.5 shows a typical hypernuclear production spectrum, where the (K^-, π^-)-reaction has been used (Brü 78). In Fig. 2.6 are the neutron and Λ potential wells schematically depicted.

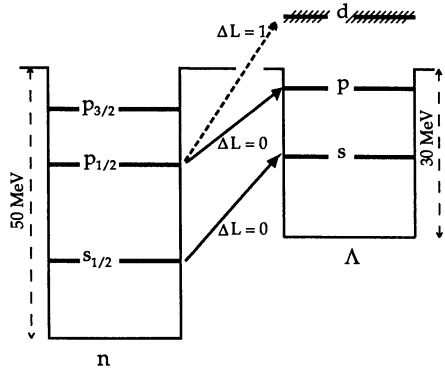

Fig. 2.6 : Schematic picture of the n and Λ potentials, with a few n→Λ-transitions indicated. Full drawn arrows are for substitutional transitions, dashed arrows indicate transitions with angular momentum change.

The (π^+, K^+)-reaction has recently been successfully used for hypernuclear studies at the Brookhaven National Laboratory (BNL) (Chr 88). Such studies are also under preparation at the KEK laboratory in Japan (Has 86). This reaction has no "magic" momentum; rather, the Λ is produced with a quite high momentum in the laboratory. Therefore, the (π^+, K^+)-reaction depends more on the high-momentum components of the nuclear wave-functions and thus preferentially excites high-spin states where these components are relatively large (Ros 88).

The (γ, K^+)- and the (π^+, K^+)-reactions are in many aspects similar, although the former seem to populate $\Delta L=1$ states while the latter preferentially excite states with $\Delta L=0$.

In the PS177 experiment a more exotic mechanism for hypernuclear production is exploited, namely that through antiproton annihilations. From sub-section 2.1.2 it is clear that strange particles, both kaons and hyperons, are produced in antiproton annihilations on nuclei. The processes which could lead to the formation of hypernuclei are :

1) Secondary interactions of kaons. About 7% of the annihilations at rest are accompanied by kaon production. These kaons are produced with momenta which are favourable to hypernuclear formation, as can be seen by comparing the kaon phase-space momentum spectrum with the "magic" kinematics of the (K^-, π^-)-reaction as shown in Fig. 2.7. In effect, the antiproton annihilation acts as a kaon factory on the surface of, or even inside, the nucleus. Additionally, since no spectroscopy is performed in the present experiment, strangeness exchange reactions involving neutral mesons can also contribute.

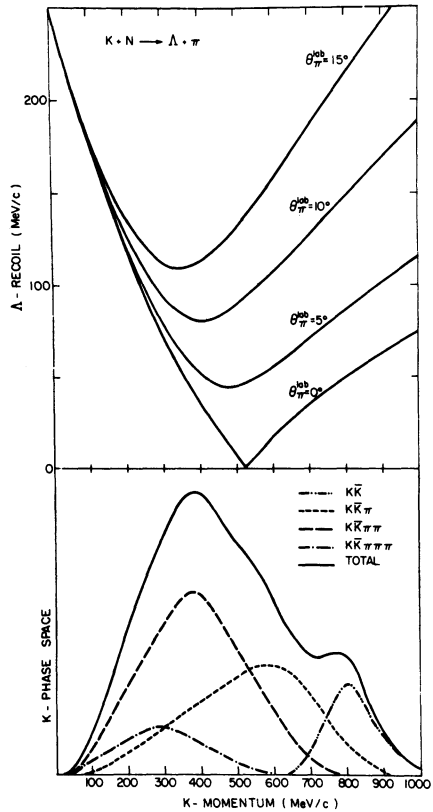

Fig. 2.7 : The phase-space momentum spectrum of the reaction $p + \bar{p} \rightarrow K + \bar{K} + n\cdot\pi$, for different number of accompanying pions, n (lower part), is compared with the kinematics of the (K, π)-reaction (upper part). From Joh 84.

2) Secondary interactions of pions. The large number of pions produced in antiproton annihilations makes it interesting to study the (π, K)-reactions in this context. However, the threshold for the elementary process, eq. 2.1, is about 900 MeV/c for Λ-production. This is at the very high-momentum tail

of the pion spectrum emitted from low-energy antiproton annihilations (Fig. 2.2). Therefore, the contribution from this process can not be expected to be very significant for annihilations at rest.

3) Attachment of directly produced Λ- or Σ-particles. The strong enhancement of the direct Λ production in low-energy antiproton annihilations, observed experimentally by several groups, makes this process an interesting candidate for hypernuclear formation.

Only very crude estimates of the expected hypernuclear production rates can be made, based on the limited knowledge of the three processes described above. Using the available information for the two-step strangeness exchange (SE) reaction, $\bar{p} + N \rightarrow \bar{K} + X$, $\bar{K} + N \rightarrow \pi + \Lambda$, one can estimate the contribution from process 1) as :

$$P_{\Lambda Z}^{(1)} = P_{\bar{p}N}^{\bar{K}} \cdot \Omega \cdot P_{SE} \cdot P_{stick} \qquad (2.6)$$

where
- $P_{\bar{p}N}^{\bar{K}}$ is the probability of producing kaons in antiproton annihilations at rest,
- Ω is the part of the solid angle covered by the residual nucleus,
- P_{SE} is the probability for a strangeness exchange reaction,
- P_{stick} is the probability that the produced Λ is bound to the nucleus.

The kaon production probability has already been given in subsection 2.1.2 as about 7% and the Ω is of the order 20%. The elementary strangeness exchange reaction, eq. 2.3, has a cross-section of about 4 mb for both the (K^-, π^-)- and the (K^-, π°)-reaction at 400 MeV/c (Fla 83). The cross-sections for the $\bar{K}^\circ$ are here assumed to be of a similar size. Scaling with the number of effective nucleons in a heavy nucleus, estimated to be about 8 (Ber 83), and normalizing to the nuclear disc area gives a $P_{SE} = 2\%$. Hsiao and Cotanch (Hsi 83) have calculated the sticking probability in ^{208}Tl. They obtain a 10% sticking probability for the (γ, K^+)-reaction with a hyperon recoil of about 250 MeV/c and this value is adopted here. Collecting the different factors gives :

$$P_{\Lambda Z}^{(1)} = 0.07 \cdot 0.02 \cdot 0.1 \cdot 0.2 = 0.3 \cdot 10^{-4} \qquad (2.7)$$

per stopped antiproton from the strangeness exchange reaction alone.

Additionally, the process 3) gives a contribution which can be written as :

$$P^{(3)}_{\Lambda Z} = P_{\Lambda} \cdot P_{stick} \tag{2.8}$$

where P_{Λ} is the probability for direct Λ production,
P_{stick} is the probability that the Λ is bound to the nucleus.

The value of $P_{\Lambda} = 1.9\%$, as given by both Condo et al. (Con 84) and Balestra et al. (Bal 86), has been adopted here. The calculation performed by Hsiao and Cotanch shows that the sticking probability drops with a factor of about two when the hyperon recoil is increased from 250 to 300 MeV/c. An experiment on antiproton annihilation on deuterium (Roy 75) has given a mean Λ recoil-momentum of 426 MeV/c. Hence, the sticking probability can be expected to be on the percent level, and a value of 2% is used here.

$$P^{(3)}_{\Lambda Z} = 0.019 \cdot 0.02 = 3.8 \cdot 10^{-4} \tag{2.9}$$

Adding the contributions from the two processes finally yields an order-of-magnitude estimate for the total hypernuclear production rate per stopped antiproton as :

$$P^{TOT}_{\Lambda Z} = P^{(1)}_{\Lambda Z} + P^{(3)}_{\Lambda Z} = 4.1 \cdot 10^{-4} \tag{2.10}$$

There is no way, however, in the PS177 experiment to study the individual mechanisms involved in antiproton induced hypernuclear production. The considerations presented here are only meant to show the plausibility of the argument : hypernuclei can indeed be formed in antiproton annihilations on nuclei.

2.2.3 Properties of Λ-hypernuclei.

The main part of this sub-section is devoted to the phenomenology of hypernuclear weak decay. However, a few other properties of hypernuclei are reviewed initially.

From the systematics of Λ-hypernuclear ground state binding energies, Fig. 2.8, it has been calculated that the Λ potential is about 30 MeV deep, only 2/3 of the nucleon potential depth. Another striking feature of the Λ-nucleon potential is the small, if not vanishing, spin-orbit interaction. A detailed analysis of the splitting between the $p_{3/2}$ - and $p_{1/2}$ - states in $^{16}_{\Lambda}O$

gives a spin-orbit splitting of 0.8 ± 0.7 MeV, to be compared with the nucleon spin-orbit splitting of 6.3 MeV (Bou 80). This situation has already been indicated in Fig. 2.6. Furthermore, since the Λ has isospin I = 0 one cannot have any one-pion exchange in the strong ΛN-interaction. Hence, the spin-spin and the tensor forces are also expected to be small (Pov 87).

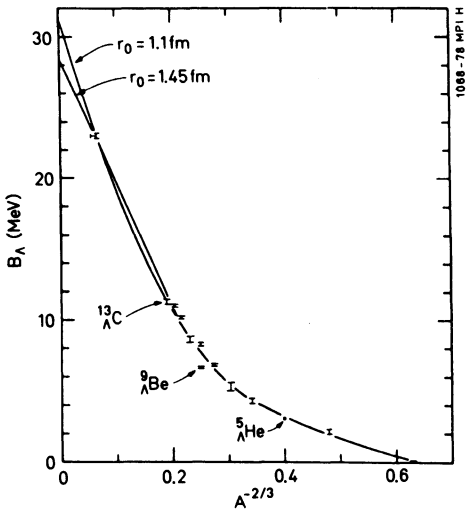

Fig. 2.8 : Binding energies of the Λ-particle plotted against $A^{-2/3}$ for hypernuclear ground states. The solid lines are fits for two different r_0 parameters in the square well potential, as indicated in the figure. From Pov 87.

The free Λ-particle decays with a lifetime of $\tau_\Lambda = (2.632 \pm 0.020) \cdot 10^{-10}$ s, mainly through the mesonic channels :

$$\Lambda \rightarrow p + \pi^- \qquad (64.2\ \%) \qquad (2.11)$$

$$\Lambda \rightarrow n + \pi^\circ \qquad (35.8\ \%) \qquad (2.12).$$

Additionally, a small part of the decays go through semi-leptonic channels : $\Lambda \rightarrow p + l^- + \bar{\nu}_l$, but they are not of interest here.

A Λ bound to a nucleus will in a very short time, about 10^{-16} s, make electromagnetic transitions down to the 1s ground state. In this environment, the presence of the surrounding nucleons opens up the non-mesonic decay channels, giving the complete set of possibilities as :

$$\Lambda \rightarrow p + \pi^- + 38\ [\text{MeV}] - (B_\Lambda - B'_p) \qquad (2.13)$$

$$\Lambda \rightarrow n + \pi^\circ + 41\ [\text{MeV}] - (B_\Lambda - B'_n) \qquad (2.14)$$

$$\Lambda + p \rightarrow n + p + 176\ [\text{MeV}] - (B_\Lambda + B_p) \qquad (2.15)$$

$$\Lambda + n \rightarrow n + n + 176\ [\text{MeV}] - (B_\Lambda + B_n) \qquad (2.16)$$

where B_Λ is the initial state binding energy of the Λ,
B'_N is the final state binding energy of the outgoing nucleon,
B_N is the initial state binding energy of the nucleon.

The final state nucleons in the non-mesonic decay are considered unbound due to the large energy release (notation according to Szy 87).

It is worth noting that the process $\Lambda N \rightarrow NN$ is one of the few weak, four-baryon interactions readily observed experimentally.

The lifetime of a heavy hypernucleus is given by the four decay rates associated with the different elementary processes of eqs 2.13-16 :

$$\tau = \frac{h}{2\pi \cdot \Gamma_{TOT}} \qquad \text{where} \qquad \Gamma_{TOT} = \Gamma_{\pi^-} + \Gamma_{\pi^\circ} + \Gamma_n + \Gamma_p \qquad (2.17).$$

As is shown in Fig. 2.9, already for hypernuclear masses around A=5 the non-mesonic channels are as likely as the mesonic. With increasing A the ratio rapidly changes in favour of the non-mesonic decay. The reasons for the dying off of the mesonic decay rate are, firstly, that the increased binding energy of the Λ - particle restricts the phase-space for the outgoing nucleon, and secondly, that fewer states are available to the slowly recoiling nucleon in a heavy nucleus, due to the Pauli principle. The non-mesonic rate is at the same time favoured by the increasing nuclear density, enhancing the overlap between the Λ and the nucleon wave functions.

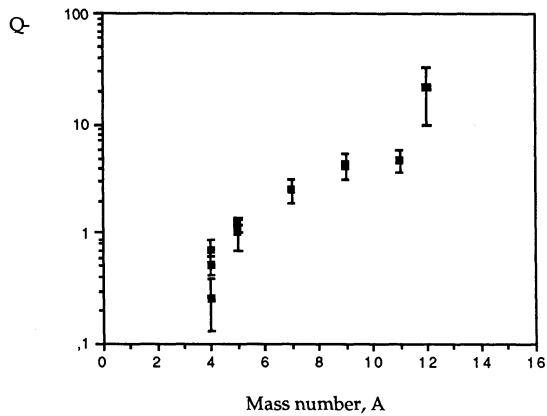

Fig. 2.9 : The ratio Q^-, of the non-mesonic decay probability to the probability for a decay via π^- emission, as a function of the hyper-nuclear mass, A. Data from the compilation in Dov 82 and from Szy 87.

For hypernuclear systems of mass A≈100 or heavier, the mesonic decay rate can be expected to be on the percent level, at most. Such systems therefore offer a good testing ground for predictions about the non-mesonic weak Λ-decay.

2.2.4 Lifetimes of hypernuclei - the experimental situation.

Experimental data on hypernuclear lifetimes are scarce. The earliest experiments of this type, made in the 1960s and early 1970s, were performed with K^- beams striking stacks of nuclear emulsions or bubble chambers. This resulted in a number of estimates for the lifetimes of the lightest hypernuclei, such as ${}^{3}_{\Lambda}H$, ${}^{4}_{\Lambda}H$, ${}^{4}_{\Lambda}He$ and ${}^{5}_{\Lambda}He$ (See, e.g., Pre 64, Kan 65 and Phi 69). The poor statistics, in combination with the particular experimental difficulties, such as the ambiguous identification of the decaying nucleus, made the errors in these measurements large. The most recent of these early experiments gave lifetimes close to the free Λ lifetime.

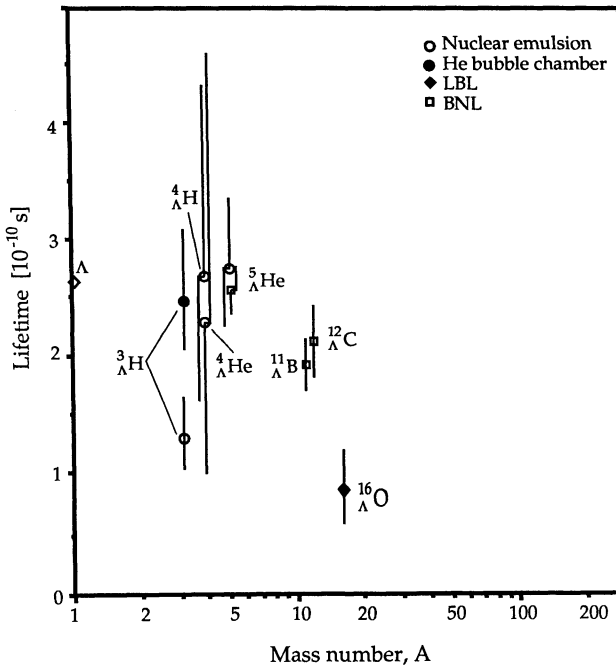

Fig 2.10 : The most recent measurements of lifetimes for the hypernuclei studied prior to this experiment. See Table 2.1 for the numerical values.

A completely different approach to the problem was taken by a Tuscon group in 1976 (Nie 76). This group, working at the heavy ion accelerator at the Lawrence Berkeley Laboratory (LBL), used a 2.1 GeV beam of ^{16}O to bombard a polyethylene target. By triggering on the decay of a K^+, as a signature for associated production of strangeness, they hoped to select events involving $^{16}_{\Lambda}O$ production. The decay in flight of these hypernuclei was then registered in a gas spark chamber. A total of 22 events gave a lifetime estimate of $0.86\ ^{+0.33}_{-0.26} \cdot 10^{-10}$ s for the $^{16}_{\Lambda}O$ hypernucleus.

Hyper-nucleus	Target	Lifetime [$\cdot 10^{-10}$ s]	Reference
$^{3}_{\Lambda}H$	Nucl.emulsion	$1.28\ ^{+0.35}_{-0.26}$	Boh 70a
	He bubble ch.	$2.46\ ^{+0.62}_{-0.41}$	Key 73
$^{4}_{\Lambda}H$	Nucl.emulsion	$2.68\ ^{+1.66}_{-1.07}$	Phi 69
$^{4}_{\Lambda}He$	Nucl.emulsion	$2.28\ ^{+2.33}_{-1.29}$	Phi 69
$^{5}_{\Lambda}He$	Nucl.emulsion	$2.74\ ^{+0.60}_{-0.50}$	Boh 70b
	^{6}Li	2.56 ± 0.21	Szy 87
$^{11}_{\Lambda}B$	Scintillator (CH)	1.92 ± 0.22	Gra 85
$^{12}_{\Lambda}C$	Scintillator (CH)	2.11 ± 0.31	Gra 85
$^{16}_{\Lambda}O$	Polyethylene (CH_2)	$0.86\ ^{+0.33}_{-0.26}$	Nie 76
$\approx {}^{209}_{\Lambda}Bi$	^{209}Bi	27 ± 5	Nog 86

Table 2.1 : Experimentally measured hypernuclear lifetimes. The compilation is not complete, for the lighter nuclei several other experiments have been performed, see, e.g., Gra 86 and Dov 82. The measurement on $^{16}_{\Lambda}O$ used a ^{16}O beam and the $^{209}_{\Lambda}Bi$ experiment used the (e, e')-reaction. All the other measurements were made with K^- beams.

During the 1980s a group working at BNL has produced a series of high-precision lifetime measurements on different light and medium-heavy hypernuclei. By detecting the energetic proton or pion, emitted in the hypernuclear decay, in coincidence with the (K^-, π^-) -production reaction and using high-quality timing scintillators they have been able to make direct lifetime measurements on the hypernuclei ${}^{5}_{\Lambda}$He, ${}^{11}_{\Lambda}$B and ${}^{12}_{\Lambda}$C (Gra 85, Szy 87).

Quite recently, a group working at the Kharkov linear electron accelerator reported delayed-fission lifetimes of 2.7 ± 0.5 ns, obtained while bombarding a ^{209}Bi target with high energy electrons (Nog 86). The delayed-fission events, only visible for electron energies above the Λ-K-electroproduction threshold, are interpreted by the authors as a signal for the decay of heavy hypernuclei in the bismuth mass region. Later, this group has also found evidence for a second lifetime component in the same delayed-fission decay (Nog 88), where the new channel has a significantly shorter lifetime than that presented above.

The results from some of the hypernuclear lifetime measurements are collected in Table 2.1, and also shown in Fig. 2.10. Except for the result obtained by the Kharkov group, the tendency of the data is that $\tau_{\text{hypernuclei}} < \tau_{\Lambda}$. This compilation is not complete ; only the latest results for each hypernuclear species are shown.

2.2.5 Lifetimes of hypernuclei - theory and calculations.

The decay of a Λ-particle is governed by the weak decay through the V-A coupling. On the quark level the weak interaction amplitude is proportional to a matrix element (Ait 82) given by :

$$Q_{V\text{-}A} = \bar{u}\gamma_\mu (1 - \gamma_5) s \; \tilde{D}^{\mu\nu} \bar{d}\gamma_\nu (1 - \gamma_5) u \qquad (2.18)$$

where u, d and s are the quark spinors,
$\tilde{D}^{\mu\nu}$ is the intermediate propagator.

It is now a well-established fact that the weak interactions are mediated by the vector bosons W^+, W^- and Z°, as is depicted in Fig. 2.11 for the weak decays of the Λ. However, for low-energy interactions where the momentum transfer is small eq. 2.18 reduces to the Fermi point-like, weak interaction :

$$H^{F}_{V\text{-}A} = \frac{G_F}{\sqrt{2}} \sin\theta_c \cos\theta_c \; \bar{u}\gamma_\mu (1 - \gamma_5) s \; \bar{d}\gamma^\mu (1 - \gamma_5) u \qquad (2.19)$$

where G_F $= 1.02 \cdot 10^{-5} \cdot m_p^{-2}$ is the Fermi coupling constant,
m_p is the proton mass,
θ_c $\approx 13.3°$ is the Cabibbo angle.

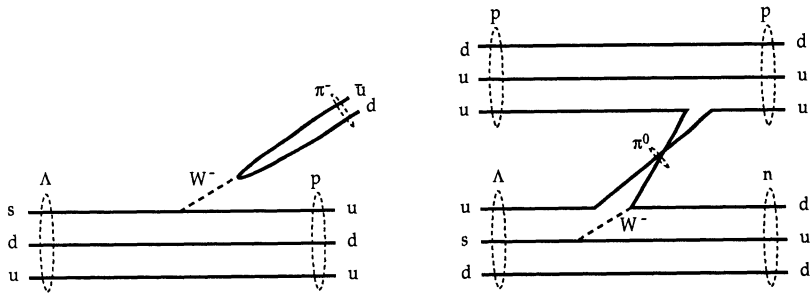

Fig. 2.11 : Quark-line diagrams of mesonic and non-mesonic Λ decay.

A problem with a Hamiltonian of the form given by eq. 2.19 is that it includes amplitudes of 1/2 unit of isospin change ($\Delta I=1/2$) and 3/2 units of isospin change ($\Delta I=3/2$) of equal strength. Empirically, hyperon decay data have shown that the $\Delta I=1/2$ - amplitude is greatly enhanced, by a factor of twenty or so. This fact is usually referred to as the "$\Delta I=1/2$ - rule". As an example one can consider the final state isospin channels of free Λ decay. For an amplitude relation $A_{\Delta I=3/2} << A_{\Delta I=1/2}$, the Clebsch-Gordan coefficients give the branching ratio :

$$R_{CG} = \frac{B(\Lambda \rightarrow p + \pi^-)}{B(\Lambda \rightarrow n + \pi^\circ)} = 2 \qquad (2.20),$$

in close agreement with the experimental ratio:

$$R_{Exp} = \frac{B(\Lambda \rightarrow p + \pi^-)}{B(\Lambda \rightarrow n + \pi^\circ)} = 1.8 \qquad (2.21).$$

Correcting for phase-space factors makes the agreement even better. The branching ratios of Σ- and Ξ-decays confirm this "rule", even though the situation for the Ω-decays casts some doubt on its universality.

Some theoretical efforts have recently been made to explain the "$\Delta I=1/2$ - rule" by calculating so called penguin diagrams and other QCD effects (Bur 88), i.e., including distortions due to the strong interaction in an effective weak Hamiltonian. It is claimed that these calculations can reproduce the observed $\Delta I=1/2$-enhancement to within 25%.

In the context of hypernuclear decay-rate calculations an earlier attempt, made by Gilman and Wise, to construct such an effective weak Hamiltonian is of interest (Gil 79). Including both "penguin" diagrams and gluon radiative corrections this calculation gives :

$$H_{Eff}^{\Delta S=1} = \frac{G_F}{\sqrt{2}} \sin\theta_1 \cos\theta_2 \cos\theta_3 \sum_j c_j Q_j \qquad (2.22)$$

where Q_j are the fundamental current-current matrix elements of the type in eq. 2.18,

c_j are the so called Wilson coefficients.

Only the first two coefficients in the sum over j in eq. 2.22 are significant, corresponding to the operators :

$$Q_1 = \bar{d}\gamma_\mu (1-\gamma_5) s \;\; \bar{u}\gamma_\nu (1-\gamma_5) u \quad \text{with } c_1 = -0.87 \qquad (2.23),$$

$$Q_2 = \bar{u}\gamma_\mu (1-\gamma_5) s \;\; \bar{d}\gamma_\nu (1-\gamma_5) u \quad \text{with } c_2 = +1.51 \qquad (2.24).$$

As the authors point out, the ratio of coefficients $(c_2 - c_1)/(c_2 + c_1)$ gives a measure of the $\Delta I=1/2$-enhancement. It is in this case 3.6, which is a step in the right direction but far from the experimental ratio of about 20.

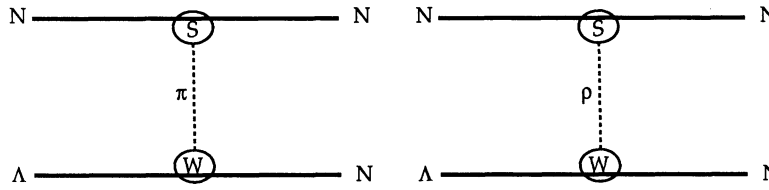

Fig. 2.12 : The weak Λ decay in the meson exchange picture. The strong and weak interaction vertices are indicated by S and W, respectively.

The results of Gilman and Wise have been used in one of the works on hypernuclear weak decay, presented below, for the short-range part of the interaction. However, most groups performing such calculations have chosen to work in the more conventional framework of meson exchange, as illustrated by Fig. 2.12. The connection to the fundamental quark-level processes is indicated in Fig. 2.11. In the meson-exchange picture the effective weak NΛπ-vertex Hamiltonian is given by :

$$H^{W}_{Eff} = G_F \; m_\pi^2 \; A \; \bar{\Psi}_N (1 + \lambda \gamma_5) \bar{\tau} \cdot \Psi_\Lambda \; \phi_\pi \qquad (2.25),$$

where m_π is the pion mass,
A, λ are empirical constants, given by a fit to Λ-decay data as
$|A| = 1.05, \lambda = -6.87$.

The $\Psi_\Lambda = \begin{pmatrix} 0 \\ \Phi_\Lambda \end{pmatrix}$ is the Λ spurion field, introduced to accommodate the "$\Delta I=1/2$-rule".

Another interesting idea in the field of hypernuclear lifetimes has been put forward by Bychkov (Byc 84). He proposes that a Λ bound to a heavy nucleus experiences a potential of the form

$$U(r) = \alpha \rho(r) + \beta \rho^2(r) \qquad (2.26),$$

where $\alpha < 0$ and $\beta > 0$ are constants,
$\rho(r)$ is the nuclear density distribution.

This has the effect that, in addition to the normal volume potential well, a narrow potential well at the nuclear surface is created. By carefully selecting the parameters, α and β, Bychkov can reproduce the found Λ binding energies and at the same time obtain a bound surface state. Since the nuclear density drops drastically at the surface, and the non-mesonic decay rate is expected to be roughly proportional to the density (see the next paragraph), Bychkov estimates that the lifetime for the Λ surface state will be more than twice that of the normal volume state. It is pointed out that the suppression of the π^- decays of heavy hypernuclei does not contradict the possibility of a surface state ; the Pauli blocking effect is still present. The author also notes that the localization of the Λ to the nuclear surface would affect the surface tension and thereby be especially important for the fission process.

In the following paragraphs, five calculations of the decay rate for heavy hypernuclear systems are reviewed. Four of these (McK 84, Ose 85, Hed 86 and Dub 86) have been performed during the 1980s, using the ingredients briefly described above. However, more than 20 years ago Dalitz (Dal 64) made an estimate of the lifetime of heavy hypernuclei and this work is presented first. The results of the various calculations are collected in Fig. 2.16.

2.2.5.1 *The Dalitz calculation.*

In his work Dalitz (Dal 64) approximates the non-mesonic decay rate by the simple expression :

$$\Gamma_{nm} = \bar{R}_{NS}({}_{\Lambda}Z) \cdot \rho_A \qquad (2.27)$$

where N and S are nucleon and spin indices, respectively,
$\bar{R}_{NS}({}_{\Lambda}Z)$ is the spin and charge averaged $\Lambda N \rightarrow NN$ transition rate for the particular hypernucleus,
ρ_A is the mean nucleon density at the Λ position.

Only initial systems in a relative s-state are included, which is a reasonable assumption considering the low ΛN relative momenta expected for hypernuclei, and the Λ decay on different nucleons is treated as independent. Dalitz argues that interference effects will generally be small and will cancel out when the decay rates are summed over all final states. Consequently, the possible $\Lambda N \rightarrow NN$ decay rates can be schematically written R_{p0}, R_{p1}, R_{n0} and R_{n1}, where the indices p and n denote the nucleon involved in the non-mesonic decay, and the indices 0 and 1 indicate opposite or parallel initial state ΛN-spins, respectively.

For the lightest hypernuclei, the $\bar{R}$ varies quite drastically, depending on the different number of nucleons in the 1s-shell. For ${}^{4}_{\Lambda}H$ it has the form

$$\bar{R}\left({}^{4}_{\Lambda}H\right) = \frac{1}{6}\left(2R_{p0} + 3R_{n1} + R_{n0}\right) \cdot \Gamma_{\Lambda} \qquad (2.28)$$

while for ${}^{4}_{\Lambda}He$ it is

$$\bar{R}\left({}^{4}_{\Lambda}He\right) = \frac{1}{6}\left(3R_{p1} + R_{p0} + 2R_{n0}\right) \cdot \Gamma_{\Lambda} \qquad (2.29).$$

Here, the Γ_{Λ} denotes the decay rate of the free Λ particle.

However, from ${}^{5}_{\Lambda}He$ and on, all 1s-orbitals are filled and, according to eq. 2.27, the decay rate depends only on ρ_A, the mean nucleon density at the Λ position. The averaged transition rate is then given by

$$\bar{R} = \frac{1}{8}\left(3R_{p1} + R_{p0} + 3R_{n1} + R_{n0}\right) \cdot \Gamma_{\Lambda} \qquad (2.30).$$

The ρ_A was calculated by Dalitz for the lightest systems, and his result was $\rho_4 = 0.019$ fm^{-3} and $\rho_5 = 0.038$ fm^{-3}.

From existing ${}^{5}_{\Lambda}$He and ${}^{4}_{\Lambda}$H data, and from the restrictions $R_{n0} = 2\,R_{p0}$ and $R_{n1} \leq 2\,R_{p1}$, imposed by the "ΔI=1/2-rule", Dalitz extracted the following set of values for the different R_{NS} :

$$R_{p0} = (\ 3.3 \pm 1.1\ ) \cdot \Gamma_\Lambda \quad [\text{fm}^{-3}] \tag{2.31}$$
$$R_{p1} = (\ 8.6 \pm 3.0\ ) \cdot \Gamma_\Lambda \quad [\text{fm}^{-3}] \tag{2.32}$$
$$R_{n0} = (\ 6.6 \pm 2.1\ ) \cdot \Gamma_\Lambda \quad [\text{fm}^{-3}] \tag{2.33}$$
$$R_{n1} = (\ 17.2 \pm 6.0\ ) \cdot \Gamma_\Lambda \quad [\text{fm}^{-3}] \tag{2.34}.$$

Inserting these numbers into eq. 2.30, and making use of the calculated ρ_5, Dalitz gives a total non-mesonic decay rate for ${}^{5}_{\Lambda}$He :

$$\Gamma_{nm}({}^{5}_{\Lambda}\text{He}) = 0.45\,\Gamma_\Lambda \qquad \text{(calculation)} \tag{2.35}.$$

This is in good agreement with the very recent experimental value

$$\Gamma_{nm}({}^{5}_{\Lambda}\text{He}) = 0.44\ {}^{+0.15}_{-0.31}\,\Gamma_\Lambda \quad \text{(experiment)} \tag{2.36}$$

reported by Szymanski (Szy 87).

Scaling with the increasing nuclear density, where $\rho_{13} \approx 3 \cdot \rho_5$ and $\rho_{100} \approx 4 \cdot \rho_5$, Dalitz obtains the values

$$\Gamma_{nm}({}^{13}_{\Lambda}\text{C}) = 1.5\,\Gamma_\Lambda \tag{2.37}$$

$$\Gamma_{nm}({}_{\Lambda}A \approx 100) = 2.0\,\Gamma_\Lambda \tag{2.38}.$$

The value of eq. 2.37 is again quite consistent with the experimental findings of the BNL-group (Gra 86), given as

$$\Gamma_{nm}({}_{\Lambda}A = 11,12) = (\ 1.32 \pm 0.12\ )\,\Gamma_\Lambda \tag{2.39}.$$

2.2.5.2 *The hybrid quark-hadron model calculation.*

A hybrid quark-hadron model was first developed by Cheung, Heddle and Kisslinger for Λ decay in nuclear matter (Che 83) and later applied to finite nuclei by Heddle and Kisslinger (Hed 86).

The amplitude for the $\Lambda N \rightarrow NN$ process is calculated in two parts. For separation distances of less than $r_0 \approx 1$ fm the interaction is described in

terms of the fundamental quarks, gluons and weak bosons. For larger distances a conventional one-pion exchange model is used.

The inner-part calculation makes use of the massless quark wave functions from the MIT bag model. The interaction Hamiltonian is taken according to the Gilman and Wise results, eqs 2.23-24. In addition to using the values for c_1 and c_2 from the original calculation, a fit to reproduce the "$\Delta I=1/2$-rule" is also performed, yielding $c_1 + c_2 = 0.32$. The contribution to the decay rate from the quark part of this model is :

$$\frac{\Gamma_Q^{nm}}{\Gamma_\Lambda} = 2.73\ (c_1 + c_2)^2 \cdot P_i^{6q} \cdot F \qquad (2.40)$$

where P_i^{6q} is the initial state six-quark probability,
F is a function of the chosen quark wave functions.

In the calculation for nuclear matter, the P_i^{6q} cannot be calculated directly. Guided by electron scattering data on ^3He, a previous calculation with the hybrid quark-hadron model has given a P_i^{6q} of about 15%. Evaluating F and using the c_1 and c_2 values consistent with the "$\Delta I=1/2$-rule", the numerical result for the quark contribution is :

$$\frac{\Gamma_Q^{nm}}{\Gamma_\Lambda} = 0.73 \qquad (2.41).$$

For the outer, pion-exchange part of the calculation the phenomenological form of the interaction Hamiltonian according to eq. 2.25 is used. Taking into account initial and final state correlations and using a pion propagator of the form :

$$\tilde{D}_{eff}^{\pi} = \frac{1}{q^2 + \tilde{m}_\pi^2} \cdot \frac{\Lambda_\pi^2}{q^2 + \Lambda_\pi^2} \qquad (2.42)$$

where $\Lambda_\pi^2 = 20\ m_\pi^2$,
$\tilde{m}_\pi = 107$ MeV is the effective pion mass,
the authors arrive at a "best" pionic contribution of :

$$\frac{\Gamma_\pi^{nm}}{\Gamma_\Lambda} = 0.77 \qquad (2.43).$$

Combining the pionic and the quark contributions their final result for the Λ decay in nuclear matter is :

$$\frac{\Gamma_{TOT}^{nm}}{\Gamma_\Lambda} = 3.0 \qquad \text{(HQH model)} \qquad (2.44).$$

Using the pure V-A-form, eq. 2.18, or the original c_1 and c_2 coefficients, eqs 2.23-24, for the calculation of the inner, quark part gives a factor 2 - 3 higher non-mesonic decay rates. For the finite hypernucleus $^{12}_{\Lambda}C$ the hybrid quark-hadron model predicts :

$$\frac{\Gamma^{nm}_{TOT}}{\Gamma_{\Lambda}} = 1.3 \qquad \text{(HQH model)} \qquad (2.45)$$

which, as the authors point out, is in excellent agreement with the experimental result (Gra 85) :

$$\frac{\Gamma^{nm}_{TOT}}{\Gamma_{\Lambda}} = (1.25 \pm 0.18) \qquad \text{(experiment)} \qquad (2.46),$$

if the mesonic decay rate is small.

2.2.5.3 *The McKellar - Gibson calculation.*

McKellar and Gibson (McK 84) make use of a pure meson-exchange model of the type depicted in Fig. 2.12. Their calculation takes into account π- and ρ-meson contributions and includes tensor forces and nuclear correlations.

For the pionic contribution, an effective weak Hamiltonian of the form in eq. 2.25 is combined with a conventional $\bar{\sigma} \cdot \bar{q}$ - coupling at the strong vertex. Thus, the amplitude of the pion contribution is :

$$M_{\pi}(\bar{q}) = G_F \mu^2 A \left[1 + \lambda \frac{(\bar{\sigma}_{\Lambda} \cdot \bar{q})}{2m} \right] \frac{1}{\bar{q}^2 + \mu^2} \times$$

$$\times \, i \frac{f}{\mu} (\bar{\sigma}_N \cdot \bar{q}) (\bar{\tau}_{\Lambda} \cdot \bar{\tau}_N) \Phi_{\pi}(\bar{q}) \qquad (2.47)$$

where
- m is nucleon mass,
- μ is the pion mass,
- $\Phi_{\pi}(\bar{q})$ is the product of the strong and weak vertex form factors.

The authors have adopted a form factor of the form

$$\Phi_{\pi}(\bar{k}^2) = \frac{\Lambda_{\pi}^2 - \mu^2}{\Lambda_{\pi}^2 + \bar{k}^2} \qquad (2.48)$$

where $\bar{k}$ is the momentum transfer.

For the ρ-contribution, the weak vertex cannot be determined from experiment. The authors use the ansatz :

$$H_{eff}^{w} = \frac{G_F}{\sqrt{2}} m_\rho^2 \bar{\Psi}_N \left\{ \alpha \gamma^\mu + i \beta \frac{\sigma^{\mu\nu} k_\nu}{2m} + \varepsilon \gamma^\mu \gamma_5 \right\} \frac{\bar{\tau}}{2} \Psi_\Lambda \cdot \bar{\rho}_\mu \qquad (2.49)$$

and put in a strong vertex of the form :

$$\Gamma^{s}_{\mu,i} = g_\rho \left[F_1 \gamma_\mu + \frac{F_2}{2m} \sigma_{\mu\nu} k^\nu \right] \frac{\tau_i}{2} \qquad (2.50)$$

where F_1 and F_2 are form factors, obeying the relation :

$$\frac{F_1(\bar{q}^2)}{F_2(\bar{q}^2)} = \frac{\Lambda_\rho^2 - m_\rho^2}{\Lambda_\rho^2 - \bar{q}^2} \qquad (2.51).$$

The unknown weak Hamiltonian coefficients α, β and ε in eq. 2.49 are determined in two different models : a factorization model and a pole model. The results from the two models differ by a factor of about 20 and have opposite signs. McKellar-Gibson conclude that maybe experimental observations can help decide which model is the more correct. For the final results they use the factorization model; the pole model gives a negligible ρ-contribution.

Effects included	$\frac{\Gamma^{nm}_{TOT}}{\Gamma_\Lambda}$
π only	0.97
ρ only	0.52
π + ρ	2.33
π - ρ	0.71

Table 2.2 : The results of the McKellar-Gibson calculation for Λ decay in nuclear matter. The factorization model has been used to determine the ρ-component, and the parameters in the form factors are $\Lambda_\pi^2 = 20\ \mu^2$ *and* $\Lambda_\rho^2 = 2.27\ m_\rho^2$.

In obtaining their final results, collected in Table 2.2, the authors restrict their analysis to initial s-states, but take into account all the possible final state angular momenta, i.e., ΔL = 0, 1 and 2. They use nuclear matter correlations and a tensor force in the final state. McKellar-Gibson point out that for the π-contribution alone, 97% of the process proceeds through the

s → d transition, induced by the tensor component in the interaction Hamiltonian.

To be able to include the ρ-contribution, one has to know the relative sign of the π- and ρ-amplitudes. Since no reliable information about this can be gained from their calculation, the authors give results both for constructive and destructive interference and they quote as their final result:

$$\log_{10}\left[\frac{\Gamma_{TOT}^{nm}}{\Gamma_{\Lambda}}\right] = 0 \pm 0.3 \qquad (2.52).$$

2.2.5.4 *The Oset - Salcedo calculation.*

In their calculation Oset and Salcedo use a many body method to study the Λ decay in nuclei (Ose 85, Ose 86). Only pion interactions are considered but on the other hand all pions, virtual as well as real, are allowed to interact with the surrounding nuclear medium. This results in a renormalization of the pion propagator, which in some cases has large effects on the decay rates.

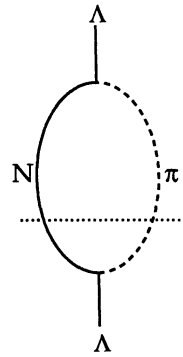

Fig. 2.13 : Diagram showing a contribution to the Λ self-energy. The free decay rate can be calculated by putting the particles crossed by the dotted line on-shell.

The decay rates are calculated from an evaluation of the Λ self-energy, depicted for free Λ decay in Fig 2.13. By requiring that the particles cut by the dotted line are on-shell, i.e., fulfilling the free-particle energy-momentum relation

$$p^0 = \sqrt{\bar{p}^2 + m^2} \qquad (2.53),$$

the Λ decay width is given by the imaginary part of the self-energy

$$\Gamma = -2\,\mathrm{Im}\,\Sigma_{\Lambda} \qquad (2.54)$$

where

$$\Sigma_\Lambda \propto \int \frac{d^4 q}{(2\pi)^4} \left(S^2 + \frac{P^2}{\mu^2} \bar{q}^2 \right) \tilde{D}_N \, \tilde{D}_\pi \tag{2.55}$$

and the nucleon and pion propagators are given by

$$\tilde{D}_N = \frac{1}{k^0 - q^0 - \varepsilon(\bar{k} - \bar{q}) + i\varepsilon} \tag{2.56}$$

$$\tilde{D}_\pi = \frac{1}{q^{0^2} - \bar{q}^2 - \mu^2 + i\varepsilon} \tag{2.57}.$$

Here, $\varepsilon(\bar{k} - \bar{q})$ is the nucleon kinetic energy.

In nuclear matter both the nucleon and the pion propagators are changed by interactions with the medium, as is schematically shown for the Λ self-energy in Fig. 2.14. The modifications to the nucleon propagator are due to the effects of the Fermi sea of nucleons and the nucleon potential. This latter quantity is here given by a local density approximation :

$$V_N(r) = -\frac{1}{2m} \left(\frac{3}{2} \pi^2 \rho(r) \right)^{3/2} \tag{2.58}$$

where the nuclear density $\rho(r)$ is taken from experiment.

The pion can interact with the nuclear medium through particle-hole and Δ-hole-excitations, as well as via s-wave πN-interactions. The net result of this is that an extra term from the pion self-energy, $-\Pi(q^0, q)$, is added to the denominator of the pion propagator, eq. 2.57.

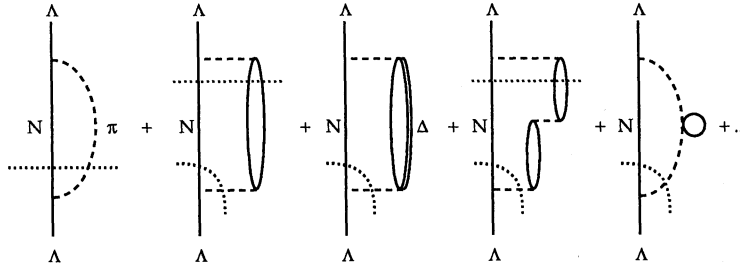

Fig. 2.14 : Diagrams contributing to the calculation of the Λ self-energy in the nuclear medium. By putting the particles cut by the dotted lines on-shell, contributions to both the mesonic and the non-mesonic decay rate can be evaluated.

When performing the integration over the complex plane, one can pick out the components corresponding to the non-mesonic and the mesonic channels. The results for the Λ non-mesonic decay rate show a smooth rise from the lighter to the heavier systems :

$$\frac{\Gamma^{nm}}{\Gamma_\Lambda} \approx 1 \qquad \text{for } {}^{5}_{\Lambda}\text{He} \qquad (2.59),$$

$$\frac{\Gamma^{nm}}{\Gamma_\Lambda} \approx 1.5 \qquad \text{for } {}^{12}_{\Lambda}\text{C} \qquad (2.60),$$

$$\frac{\Gamma^{nm}}{\Gamma_\Lambda} \approx 2 \qquad \text{for A} \approx 100 \text{ hypernuclear systems} \qquad (2.61).$$

Note, however, that these numbers include only the contribution from pions in the meson-exchange. As the authors point out, if heavier mesons are included the total non-mesonic rate decreases by about 25%, as shown by Dubach (see the next paragraph). Taking this into account gives a calculated $\Gamma^{nm}/\Gamma_\Lambda$-value for ${}^{12}_{\Lambda}$C which is very close to what is found experimentally (Gra 85). For the heavy hypernuclear systems the corrected non-mesonic decay rate is :

$$\frac{\Gamma^{nm}}{\Gamma_\Lambda} \approx 1.5 \qquad \text{for A} \approx 100 \text{ hypernuclear systems} \qquad (2.62).$$

An interesting result of the Oset-Salcedo calculation is the large enhancement seen for the mesonic decay of heavy hypernuclei. However, although the enhancement can be as large as a factor 30 for medium heavy hypernuclear systems, the mesonic decay is still predicted to be at the 1 - 2% level for hypernuclei of mass A ≈ 200.

2.2.5.5 *The Dubach calculation.*

In his calculation, Dubach (Dub 86) treats the Λ non-mesonic decay as a one-meson exchange process, including both weak and strong interactions, as depicted in Fig. 2.15. Both the pseudoscalar mesons, π, η and K, and the vector mesons, ρ, ω and K*, are taken into account.

By using $SU(6)_W$ symmetry and enforcing the "ΔI=1/2-rule" the author obtains the relation

$$\langle M' \mid H_W \mid M \rangle \propto \langle \pi \mid H_W \mid K \rangle \qquad (2.63)$$

i.e., all weak meson-meson amplitudes in the diagram of Fig. 2.15c are related to the $K \to \pi$ - amplitude, given by the $K \to \pi\pi$ decay rate.

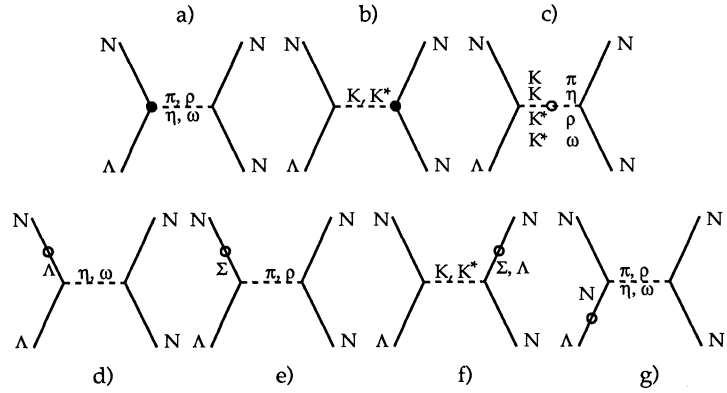

Fig 2.15 : Meson exchange diagrams used in the Dubach calculation. A black dot indicates the full strangeness changing weak interaction. An open circle indicates a weak meson-meson or baryon-baryon transition.

The weak baryon-baryon amplitudes in diagrams 2.15d-g are related to the physical Λ and Σ decays by

$$\langle N \mid H_w \mid \Lambda \rangle \propto \langle \pi^0 n \mid H_w \mid \Lambda \rangle \tag{2.64}$$

$$\langle N \mid H_w \mid \Sigma \rangle \propto \langle \pi^0 p \mid H_w \mid \Sigma^+ \rangle \tag{2.65}.$$

In Fig. 2.15, a weak strangeness changing interaction is marked by a black dot and an open circle indicates a weak baryon-baryon or meson-meson transition.

With these ingredients the author is able to calculate the $\Lambda N\pi$-amplitude

$$A^{\Lambda N\pi} = 1.35 \cdot 10^{-6} \qquad \text{(calculation)} \tag{2.66}$$

in good agreement with the experimental value

$$A^{\Lambda N\pi} = 1.61 \cdot 10^{-6} \qquad \text{(experiment)} \tag{2.67}.$$

For the final calculation the Λ is taken to be at rest inside a Fermi sea of nucleons with a Fermi momentum of $k_F = 268$ MeV/c. Only initial s-states

are included but all possible s, p and d final states are taken into account. A few different forms for the initial and final state wave functions are considered to take into account nuclear correlations in the best possible way.

Effects included	$\frac{\Gamma^{nm}}{\Gamma_\Lambda}$
π (no correlations)	3.89
π (with correlations)	1.82
$\pi + \rho$	1.55
$\pi, \rho, \eta, \omega, K, K^*$	1.23

Table 2.3 : The results of the Dubach calculation for Λ decay in nuclear matter.

Dubach gives the values in Table 2.3 as his final results. It is worth noting the ≈30% decrease in the decay rate when going from the pure π-exchange to including the full set of mesons. It is also pointed out that in the full calculation the s → d rate is substantially reduced compared to the pure π-exchange ; s → p and s → d transitions contribute with about equal strengths to the final result.

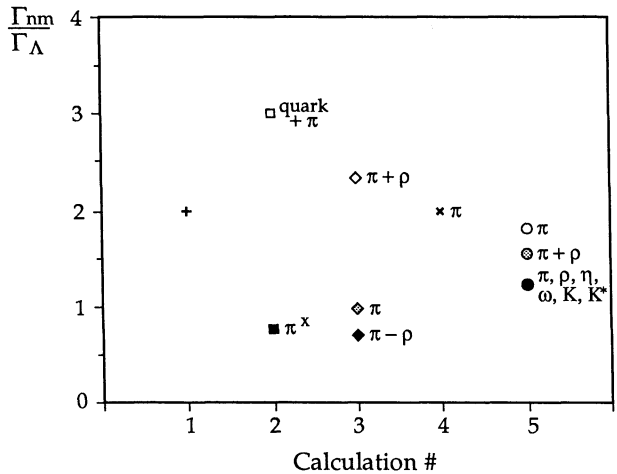

Fig. 2.16 : Results from the theoretical calculations on the Λ decay in nuclear matter. The calculations are 1) Dal 64, 2) Hed 86, 3) McK 84, 4) Ose 85 and 5) Dub 86. Each point, except for calculation 1, is marked with the mesons included. Note that the π-exchange in calculation 2, marked by an x, is only evaluated for R > 1 fm.

2.3 The fission process.

One of the most spectacular phenomena in nuclear physics is the splitting of a heavy nucleus into two, approximately equal fragments. This process is called binary fission and some of its fundamental properties are described in this section. However, since the fission process is mainly used as a tool in this thesis, the treatment will be very brief. Most of the general material is collected from the book by Vandenbosch and Huizenga (Van 73). Several reviews on fission isomers exist; particularly those by Metag et al (Met 80) and Poenaru (Poe 77) have been used as references here.

2.3.1 The physics of fission.

Simply from studying a chart of nuclear masses, it is clear that for heavy nuclei, the splitting into two equal-weight fragments is energetically favourable. The quantity ΔM, defined as

$$\Delta M = M(A, Z) - 2 \cdot M(A/2, Z/2) \tag{2.68}$$

is positive for nuclei with a mass larger than about A = 90. However, it is well known that even for the heaviest naturally occurring nuclides, such as ^{238}U, only a very small decay rate through spontaneous fission has been observed. The reason is that heavy nuclei are stable against small deformations in their shape; there is a certain energy barrier, the fission barrier, which has to be surmounted before fission can take place. This situation is schematically shown in Fig. 2.17.

The fission barrier height is very sensitive to the nuclear mass, typically dropping from about 20 MeV for $A \approx 200$ to only a few MeV for mass $A \approx 250$. Spontaneous fission, found for some nuclides with mass $A \geq 230$, is a quantum mechanical tunneling phenomenon, the rate for which is very sensitive to the height and width of the fission barrier. As typical examples, spontaneous fission half-lives range from 10^{19} years for ^{230}Th to about 400 μs for ^{258}Fm. The nuclide ^{252}Cf, used as a calibration source in this work, has a half-life of about 80 years for fission decay. Only 3% of the decays of this nuclide go through fission, the main rate being due to α-emission.

The changes in the shape of the fissioning nucleus as it moves from the ground state to a situation with two separated fragments are depicted in the upper part of Fig. 2.17. The critical point at the top of the fission barrier, from which the nucleus inevitably moves towards fission, is called the saddle

point. The final division into two separate fragments takes place at the so called scission point.

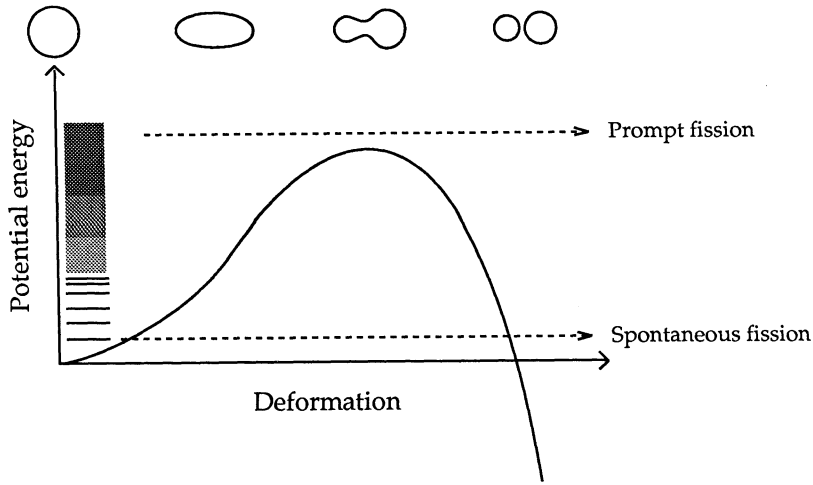

Fig. 2.17 : Schematic illustration of a single-humped fission barrier. The shapes of the nucleus at different stages of the fission process are indicated on the top.

Through bombardment with different types of projectiles one can extend the mass range of fissioning nuclides, and systematically study the energy dependence of the fissility, i.e., the ratio of the fission cross-section to the total reaction cross-section. Common probes are neutrons, γ-rays and charged particles like protons, deuterons or α-particles. Even pions and muons have been used to induce fission. In general, the fission cross-section depends on the shape of the fission barrier, on the excitation energy and also on the possibility of decay through competing channels, like neutron emission. For highly excited, heavy nuclei the different stages in the deexcitation process follows about the same scheme as for antiproton annihilation, shown in Fig. 2.3. A higher excitation energy imparted to a heavy nucleus gives a higher probability for fission, since the competition between neutron emission and fission decay is repeated through many steps before the excitation energy is reduced below the fission barrier. This situation is clearly illustrated in Fig. 2.18, where the fission probability for different nuclei bombarded with high energy protons is shown. As the proton energy is increased from 150 MeV to 1 GeV the fissility steadily goes up.

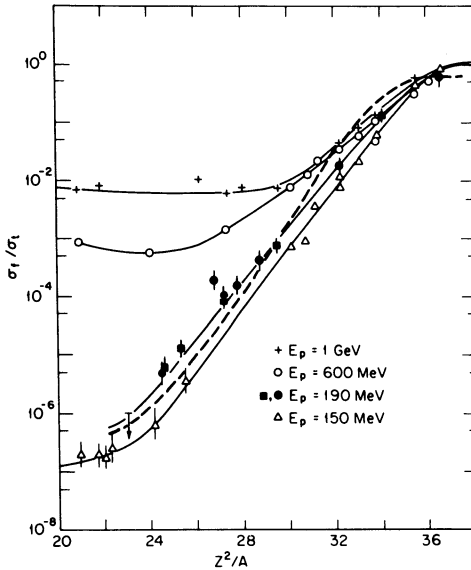

Fig. 2.18 : Fission probability, given as the ratio of fission to geometrical cross-sections, in proton induced reactions as a function of Z^2/A. The figure is taken from Bec 83, where the references to the different original works can be found.

Once fission has taken place, most of the released energy is carried away by the fission fragments, primarily as kinetic energy but also as excitation energy. Typical fragment velocities are of the order 1 cm/ns. Since the neutron excess increases with mass, the two daughter fragments will be highly neutron-rich and they normally emit 2-4 neutrons in a short time after fission. For excitation energies below the neutron emission threshold the deexcitation process proceeds through γ-emission. The fragments finally reach a stable state by slow β-decay.

The kinetic energy released in fission is mainly determined by the Coulomb repulsion of the two fragments at the instant of scission and it is relatively insensitive to the excitation energy. An approximate correlation between the mass and charge of the mother nucleus and the average kinetic energy release is given by

$$\langle E_{kin} \rangle = 0.1071 \; Z^2 / A^{1/3} + 22.2 \qquad [\text{MeV}] \qquad (2.69).$$

Thus, for bismuth one obtains $\langle E_{kin} \rangle \approx 145$ MeV, while uranium gives $\langle E_{kin} \rangle \approx 175$ MeV. The total kinetic energy for a certain fissioning nucleus will, however, depend on the mass ratio of the two fragments. A slightly asymmetric mass split gives a higher total kinetic energy, a fact which is illustrated in the upper part of Fig. 2.19.

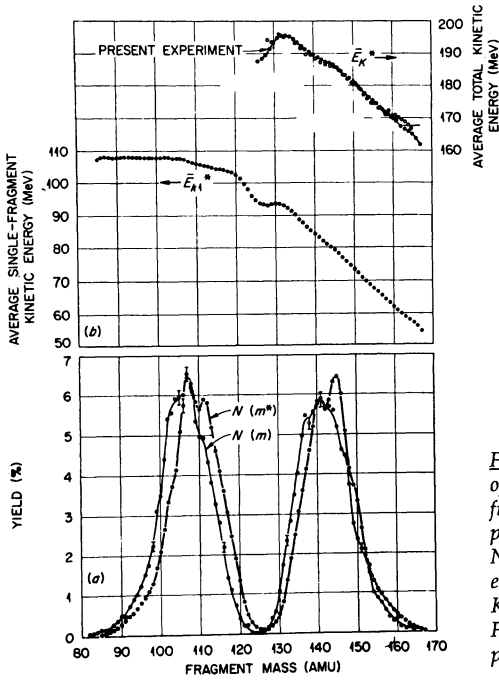

Fig. 2.19 : a) Mass distribution of fragments from spontaneous fission of ^{252}Cf. $N(m^*)$ is the preneutron-emission and $N(m)$ the postneutron-emission mass distributions. b) Kinetic energy distributions. From Sch 66. See the original paper for further details.

The mass distribution of fission fragments depends strongly on the excitation energy of the fissioning nucleus. As an example of low-energy fission, the lower part of Fig. 2.19 shows the mass distribution of fragments from spontaneous fission of ^{252}Cf. For this nuclide, practically no fission events give rise to a symmetric split of the nucleus. The mean mass for the heavy fragment is about A = 139 while for the light fragment it is A = 106. As the excitation energy of the fissioning nucleus is increased, the symmetric mass splitting is more and more pronounced. For nuclides with $Z \leq 83$, where the fission barrier is high, the symmetric mode predominates, resulting in an approximately Gaussian distribution of fragment masses. However, for fission induced by high-energy protons an almost uniform mass distribution has been observed for intermediate-mass nuclei, like Sb, Ag and Ni (And 87).

2.3.2 Fission isomers.

In 1962 S.M.Polikanov and co-workers (Pol 62) discovered a fission activity with a half-life of about 14 ms in the reaction products after bombarding a ^{238}U target with energetic ^{16}O and ^{22}Ne ions. The produced nuclide was later identified as ^{242}Am, the normal spontaneous fission half-life of which is close to 10^{12} years. Considering that induced fission normally takes place in about 10^{-17} s after the impact of the energetic projectile, it was clear that a new phenomenon had been discovered.

To explain the short spontaneous-fission lifetime, a model with a more complicated, two-humped fission barrier had to be invoked, schematically shown in Fig. 2.20. In this picture, there exists an isomeric state for a larger deformation than that of the ground state.

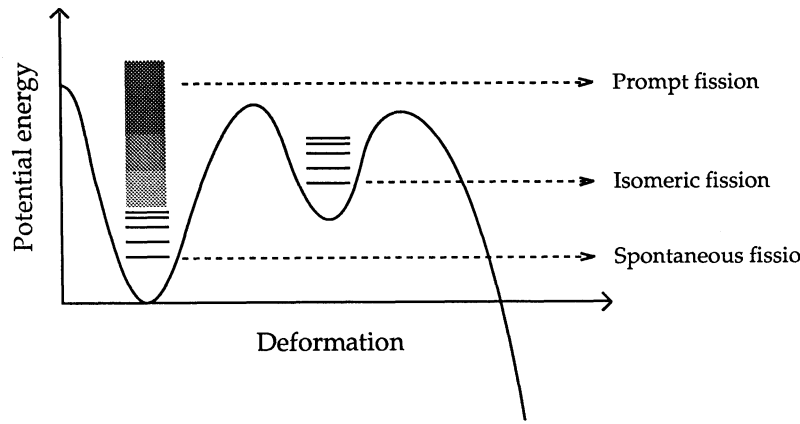

Fig. 2.20 : Schematic illustration of the double-humped fission barrier.

Normal spontaneous fission involves the tunneling from the ground state to a complete separation into two fragments. If, however, enough excitation energy is supplied to the nucleus, it may reach the isomeric state in the second minimum. From there it can either continue to fission by tunneling through the second barrier or revert to the ground state by γ-emission. The γ-decay back to the ground state is for most fission isomers hindered by the different shapes of the ground state and the isomer, with the possible exceptions of the U and Np isomers. The short lifetime of the isomeric state is due to the fact that the second barrier is both narrower and lower than the full barrier seen from the ground state. Clear evidence for the

existence of the second potential minimum, with a larger deformation, has been seen in the rotational band structure of a few nuclides (see, e.g., Spe 72).

Until now, fission isomers have been observed in more than 30 nuclides from ^{236}U to ^{246}Am (Fig. 2.21). Their half-lives range from 14 ms for the most long-lived to just a few ps for the most short-lived state. The lightest known fission isomer, that of ^{236}U, has a half-life of about one hundred ns.

The most convenient way to produce fission isomers is by simple pick-up reactions, using protons, neutrons, deuterons or α-particles. Under such conditions, it is relatively easy to control the identity of the isomeric nuclide and the amount of energy transferred. The production cross-sections are normally very low. Thus, in the most favourable reactions the ratio of isomeric production to the total geometrical cross-section is of the order 10^{-4}.

The existence of the "isomeric island" for masses around A ≈ 236 - 246 is theoretically explained as an interplay between macroscopic (liquid drop) and microscopic (shell structure) nuclear effects. It is not believed that fission isomerism will be found for nuclei with masses outside this region.

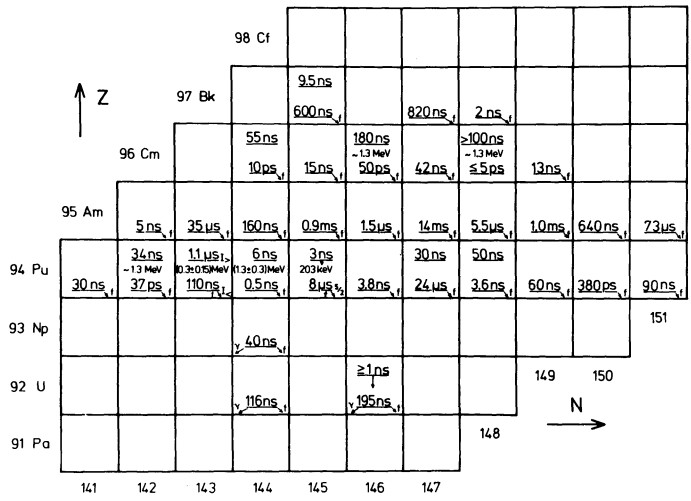

Fig. 2.21 : The nuclide chart of fission isomers. Two values for the same nucleus indicate spin isomeric states in the second minimum. From Met 80.

Chapter 3 : THE PS177 EXPERIMENT.

3.1 The CERN low-energy antiproton facility.

The PS177 experiment was performed at the Low Energy Antiproton Ring, LEAR, one of the experimental facilities of the European Organization for Nuclear Research, CERN, situated in Geneva, Switzerland. The data presented here were collected during two separate periods: in September 1985 and in July 1986.

An overview of the CERN antiproton complex is shown in Fig. 3.1. The antiprotons are produced by a beam of 26 GeV/c protons from the CERN proton synchrotron, PS, striking a Cu target. The produced antiprotons have a broad distribution of momenta, with a flat maximum at 3-4 GeV/c (Jon 84). A system for collecting and transporting the antiprotons, designed for particles of 3.57 GeV/c ±0.75%, injects them into the Antiproton Accumulator, AA. New bunches of particles are added to the stack in AA every 2.4 seconds. In the AA the antiprotons are subjected to stochastic cooling to reduce the phase-space spread of the stack. The cooled antiprotons are then transferred back to the PS for deceleration to 600 MeV/c before being injected into the LEAR machine.

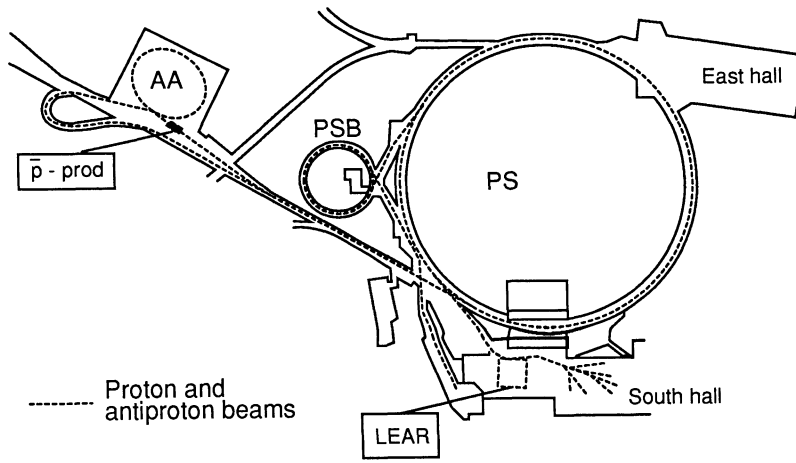

Fig. 3.1 : Schematic drawing of the CERN low-energy antiproton complex. PS is the proton synchrotron, PSB the proton synchrotron booster, AA the antiproton accumulator and LEAR the low energy antiproton ring. The antiproton production target is indicated by " $\bar{p}$ - prod ".

LEAR, situated in the CERN South hall, is a storage-cooler ring with a circumference of 78 m (Lef 84, Lef 85). It is designed to provide the experiments with high quality antiproton beams in the momentum range of 0.1 - 2.0 GeV/c. Using stochastic cooling, the momentum spread of the extracted beams is reduced to $\Delta p/p = 0.5 - 1 \cdot 10^{-3}$. By means of an ultra-slow extraction system, LEAR delivered a continuous beam, with an antiproton intensity of typically 10^5 per second over a period of about 50 minutes.

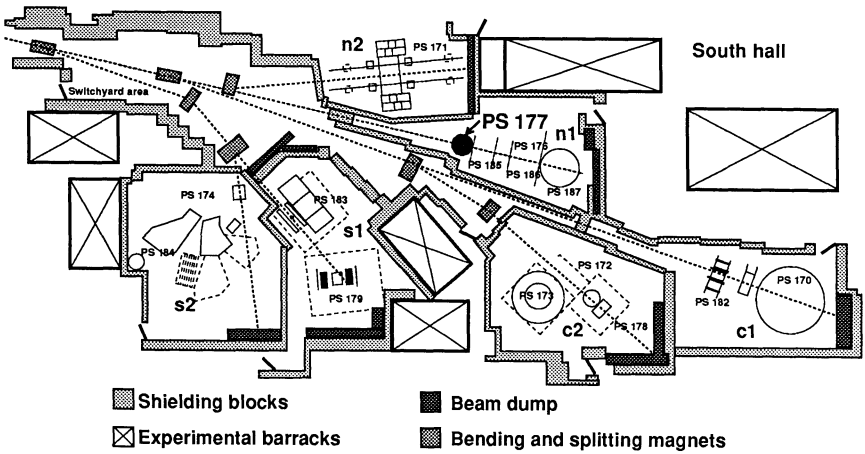

Fig. 3.2 : Lay-out of the LEAR experimental area, in the CERN South hall. The position of the PS177 experiment is indicated by the black dot in the n1 area. June 1983.

The PS177 experiment was located in the n1 experimental area as the most up-stream experiment on this beam-line. A plan of the South hall floor space is shown in Fig. 3.2.

The n1 was one of two beam-lines specially designed for providing antiprotons at the low-momentum end of the LEAR momentum range. To accomplish this the most stable power supplies for the beam-line elements and special beryllium windows at the down-stream end of the beam-pipes were installed. These special precautions were aimed at keeping stable beam conditions and reducing the multiple Coulomb scattering as much as possible.

The antiproton beam delivered at the PS177 target position, marked by a black dot in Fig. 3.2, had a nominal momentum of 105.5 MeV/c and a beam-spot width of about 2 mm (FWHM) both horizontally and vertically (Fig. 3.3). Note that the measurement in Fig. 3.3 includes multiple scattering in the beam-line exit window.

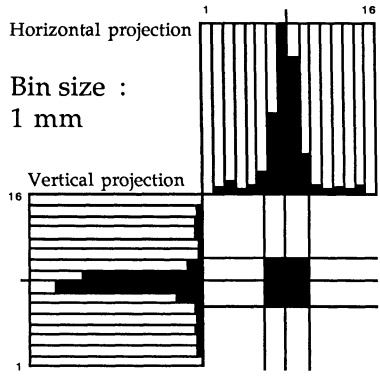

Fig. 3.3 : A cross-section of the LEAR beam at the PS177 target position, measured by the LEAR beam diagnosticcs group. The histogram bin size is 1 mm both horizontally and vertically.

3.2 The recoil-distance method.

The experimental technique used in the work presented here is the so called recoil-distance method, first described by Metag et al. in 1974 (Met 74). This technique has been widely used to study fission isomers, determining their lifetimes, in the ps to ns region, and the reaction cross-section (see, e.g., Sle 76).

The special geometrical arrangement of this method is recalled in Fig. 3.4. A thin target, having a well-defined width ρ, is deposited on one side of a thick target backing, having a width r. The backing width r is slightly larger than the target width ρ. At some distance R, where $R >> r$, from the centre of the target the detectors are placed, parallel to the beam axis, x. The target arrangement defines two regions in the detectors, separated by the projection of the target plane : an open region with an unobstructed view of the target, and a shadowed region where the view to the target is blocked by the target backing.

The recoil-distance technique is a fission-in-flight method that depends on the fact that prompt fission, occurring about 10^{-18} s after the antiproton annihilation, takes place inside the thin target while nuclei decaying by

delayed fission, in the case of hypernuclei occurring after about 10^{-10} s, have a chance to escape out of the target. Fission fragments emitted from the target plane can only be recorded in the open area of the detectors, any fragment directed towards the shadowed area will be stopped in the target or the target backing. On the other hand, fission events that take place in the fission chamber at some distance away from the target plane have a possibility to emit fragments that are registered in the shadowed area of the detectors.

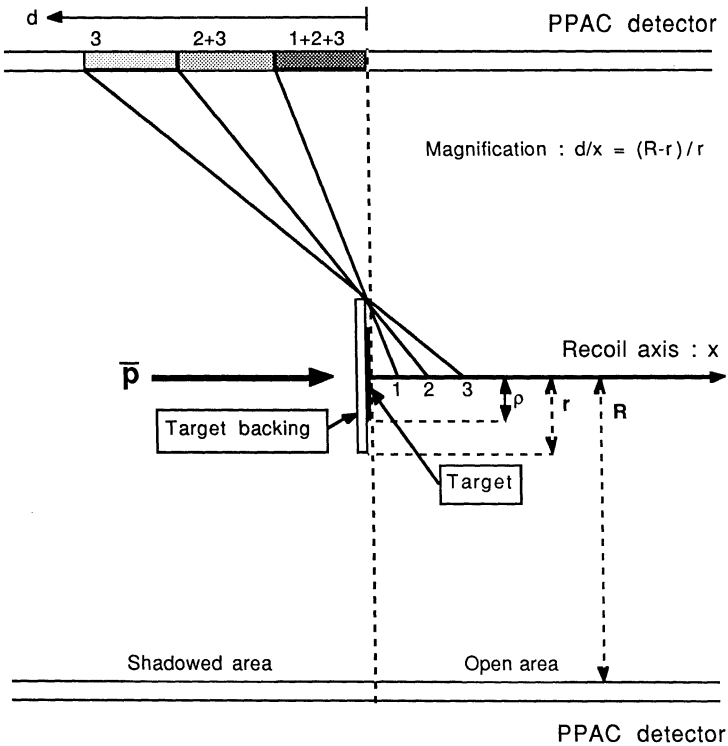

Fig. 3.4 : The principle of the recoil-distance method. The distance recorded in the detector, d, is magnified a factor (R-r)/r compared to the distance travelled by the recoil, x_i, along the recoil axis. The drawing is not to scale.

Furthermore, as can be seen from Fig. 3.4, the short distances travelled by the recoils before they decay are magnified in the detectors. This is exemplified by the three perpendicular recoils coming from the centre of the

target in the figure. Fragments emitted from the position 1 along the x-axis can strike the shadowed area of the detectors only in the dark shaded region marked 1+2+3. Fragments coming from positions further away from the target plane can reach successively deeper into the shadowed area, as shown by the lighter shaded regions 2+3 and 3. The maximum magnification for any recoil distance x, along the beam axis, is simply

$$\frac{d}{x} = \frac{(R-r)}{r} \approx \frac{R}{r} \quad \text{, since } R >> r \qquad (3.1).$$

The position distribution of fission fragments recorded in the shadowed part of the detectors is thus determined by the recoil distances of the decaying nuclei. This distance, in turn, depends on the lifetime and the velocity of the recoil. Only under simplifying assumptions is it possible to calculate this position distribution analytically. In general it is necessary to use specially developed simulation programs to take into account the actual experimental conditions. The simulation program used in the present experiment is described in section 5.1.

3.3 The experimental set-up.

3.3.1 The fission chamber.

The whole PS177 experiment was housed in a 55 x 55 x 55 cm^3 aluminium box, the fission chamber. The design of this box is schematically shown in Fig. 3.5 and the main components are described below.

The large energy losses suffered by fission fragments when passing through matter makes it necessary to keep the interior of the fission chamber under vacuum. The box was pumped by means of a turbo-molecular pump with a capacity of 500 l/s, typically keeping a few times 10^{-5} torr vacuum.

The antiproton beam entered the box about 15 mm from its centre by a special construction of the wall facing the LEAR beam pipe. It is preferable to have the foils separating the LEAR high vacuum from the lower vacuum of the fission chamber as close to the target as possible. This minimizes the effect of multiple scattering of the beam, thus keeping a good focus on the target spot. The passage from one vacuum to the other consisted of two thin foils, the LEAR beam line exit foil of 100 μm Be and the box entrance foil of 25 μm Kapton, separated by a 5 mm air gap. The diameters of the foils were

35 mm for the exit foil and 16 mm for the entrance foil. See Fig. 3.7 for details.

On each vertical wall, parallel to the beam, was placed a parallel plate avalanche counter (PPAC), each with a dimension of 190 mm horizontally and 290 mm vertically. These were the main detectors of the experiment and they are described in detail in sub-section 3.3.4. Their distance to the beam line axis, and consequently to the centre of the target, was 270 mm.

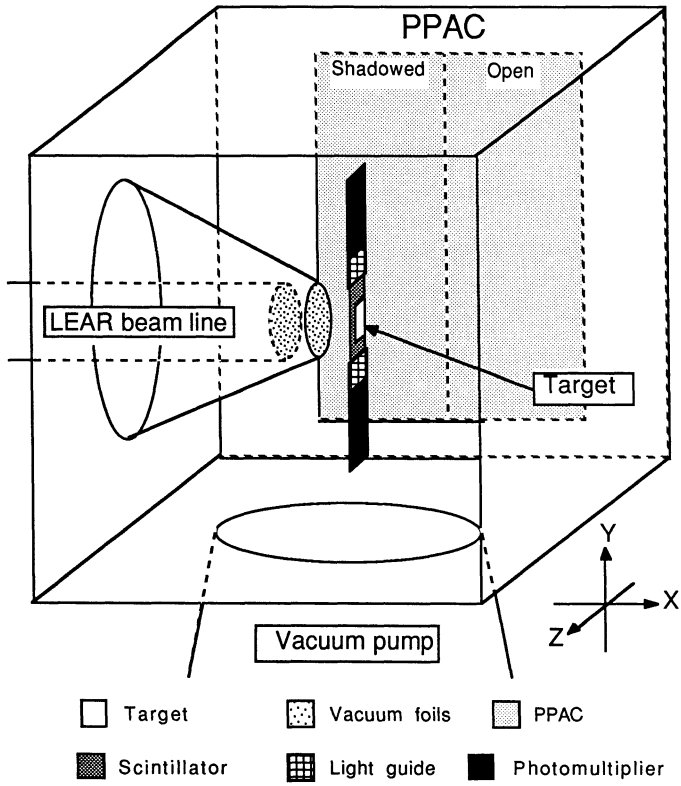

Fig. 3.5 : Schematic side view of the fission chamber with the closest wall removed. The experimental coordinate system is also indicated. Note, however, that the origin is at the centre of the target. See Fig. 3.7 for a closer view of the target region.

The target arrangement, which is described in detail in the next sub-section, was placed in the centre of the fission chamber. The volume between the target and the parallel plate chambers was kept clean of all

material, such as cables, light guides, PM tubes etc. All these parts were placed in the space above and below the target, making a clear path for fragments emitted from the target surface towards the detectors.

3.3.2 The target arrangement.

The experimental environment and the detection technique adopted put special demands on the construction of the targets, degraders and the beam diagnostics equipment.

The recoil distance technique, see Fig. 3.4, requires a small target backing width, r, and consequently an even smaller target width, ρ, to give a large magnification, d/x, on the detectors. Furthermore, the target has to be very flat to define the separation between open and shadowed regions accurately, and it must have perfectly defined edges to keep a constant magnification over the whole surface.

The target should be thin to permit the slow, recoiling nuclei to escape, but at the same time it should be thick enough to give a sufficiently high antiproton stopping rate. The choice of target material has to be a compromise between the requirements of a low fission yield in the primary antiproton annihilation, and a high fission yield in the hypernuclear decay. Additionally, it is an advantage to stay away from mass regions where short-lived fission isomers can be produced.

Prior to the LEAR era little was known about antiproton interactions with heavy nuclei, and more specifically, antiproton induced fission. In the original proposal (Joh 80) the use of Th-, U- and Pu-targets was foreseen. Tests of several different targets : Pb, Au, Bi and U, were performed in order to measure fission probabilities. These tests involved nuclei in a wider mass range than originally proposed, motivated by the desire to study possible target nuclei in a broader region of the parameter Z^2/A.

A simple test set-up was arranged, with the antiprotons stopped in thin, self-supporting targets inclined 45° to the beam and placed in the centre of the fission chamber, facing the PPACs. Coincident fission fragments were recorded in the two PPAC detectors, giving the relative fission probabilities. The measured fission probabilities, normalized to an assumed 100% fission in U, are plotted in Fig. 3.6 (Ber 85). On the basis of this test, the Bi target could be expected to be a good candidate for the hypernuclear production.

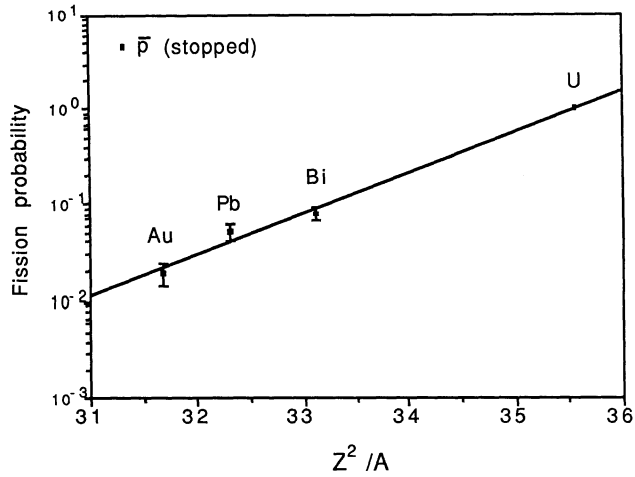

Fig. 3.6 : Fission probabilities for antiprotons stopped in targets of Au, Pb, Bi and U as a function of Z^2/A. The straight line is a fit to an exponential. The values are normalized to 100% fission in U. Data from Ber 85.

However, using the normal hypernuclear production set-up (Fig. 3.5), no trace of delayed fission was found in the first short test runs with a Bi target. Quite unexpectedly, tests with a U target, on the other hand, showed clear evidence of delayed fission events.

These findings for the different nuclei led to the choice of two different heavy targets, ^{209}Bi and ^{238}U, in the final heavy hypernucleus production runs presented here.

The final design adopted for the target region is shown in Fig. 3.7. The dimensions of the target were 2 mm horizontally and 5 mm vertically for both target types. In the ^{209}Bi case it was put on the backing by evaporation. The thickness of the ^{209}Bi layer was given by a simultaneous resistance measurement on an glass plate adjacent to the actual target. The ^{238}U material was put on the backing by ion implantation, performed at the PARIS isotope separator in Orsay, France (Meu 81). In this latter case a thin aluminium coating was put on one side of the backing, making it possible to gauge the amount of material deposited by measuring the current. An independent measurement of the α-activity of the U-target confirmed the mean thickness. Both targets had a thickness of 100 $\mu g/cm^2$.

A thin slab of plastic scintillator, type NE110, was used as target backing. At the same time, this scintillator acted as a degrader of the beam and an

antiproton counter. The thickness of the scintillator was 220 μm and the width in the z-direction, corresponding to 2r in Fig. 3.4, was 2.5 mm for the hypernuclear production runs. In a separate test run a 10 mm wide scintillator backing for a uranium target was used (see sub-section 5.2.5). The vertical length of the scintillator was 50 mm and at each end it was connected to a cylindrical plexiglass light guide. These light guides were in turn connected to photomultiplier tubes, Philips XP1911.

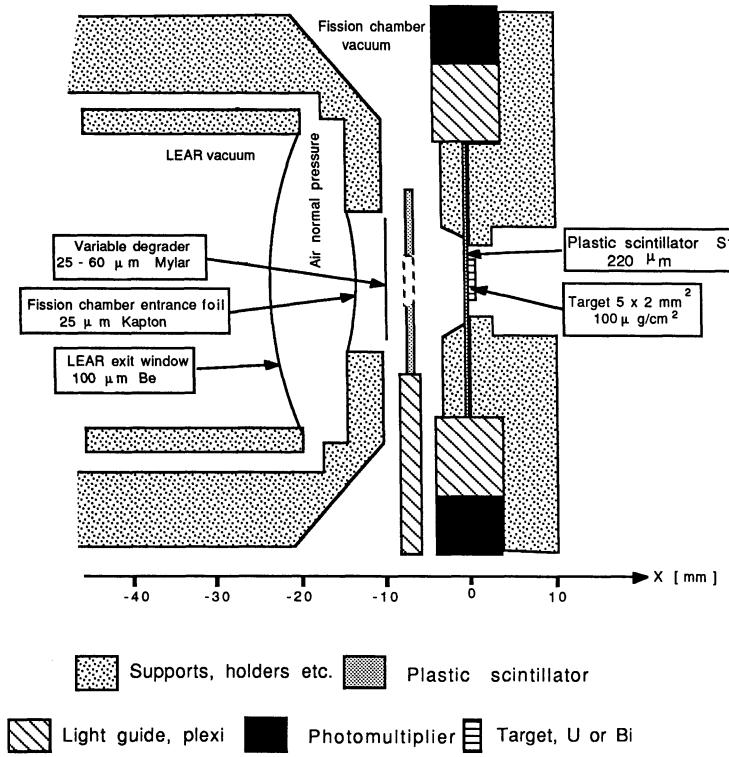

Fig. 3.7 : Design of the target region. The scale in mm is only approximate.

To align the targets in a position perpendicular to the antiproton beam axis, a laser beam test was performed. The laser was put a few meters downstream of the target and aimed at the target along the beam axis, passing through a hole in the downstream wall of the fission chamber. The target was adjusted in such a way that the laser light was reflected straight back along the beam axis again.

The flatness of the target surfaces was tested by interferometry with a Na-lamp. They were found to be flat to within 1 μm.

3.3.3 Detecting and stopping antiprotons.

The low kinetic energy of the antiproton beam, 5.3 MeV, made it necessary to construct a compact, low-mass system for degrading the antiprotons and performing the necessary beam diagnostics.

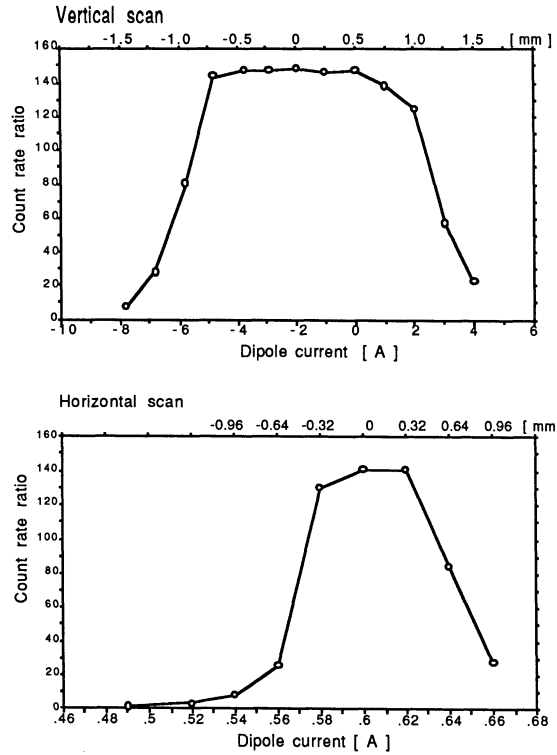

Fig. 3.8 : Vertical and horizontal scan with beam line dipoles. The count rate S1·$\overline{S2}$/S2 is plotted as a function of dipole current. The correspondence current to distance is indicated at the top of each plot.

As indicated in the previous sub-section, the target backing was in itself a part of the beam diagnostics system, acting both as a fixed degrader and an antiproton counter. This is the 220 μm plastic scintillator, S1, in Fig. 3.7.

Another scintillator, 1 mm thick, with a 3 x 6 mm^2 hole cut out, was placed 7 mm upstream of the target. The centre of this hole was positioned on the beam axis. Hence, this scintillator, S2, acted as a beam anti-counter, the count rate of which had to be minimized at the same time as the S1 rate had to be at its maximum.

A preliminary focussing and centring of the beam on the expected target position was made with a beam diagnostics wire-chamber by the LEAR staff before the experimental equipment was put in the beam line (see Fig. 3.3). To fine-tune the beam onto the actual target spot, two beam line dipoles, a few meters up-stream of the experimental position, were adjusted once the fission chamber was put in place. Fig. 3.8 shows an example of such a dipole scan. The count rate of scintillator S1, vetoed by S2, was compared to the rate of S2 itself to monitor the number of antiprotons striking the target. The optimum dipole settings were chosen at the centre of the broad distributions, I_{vert} = -2.0 A and I_{hor} = 0.6 A in Fig. 3.8, giving a maximum rate $S1 \cdot \overline{S2}/S2$, both horizontally and vertically.

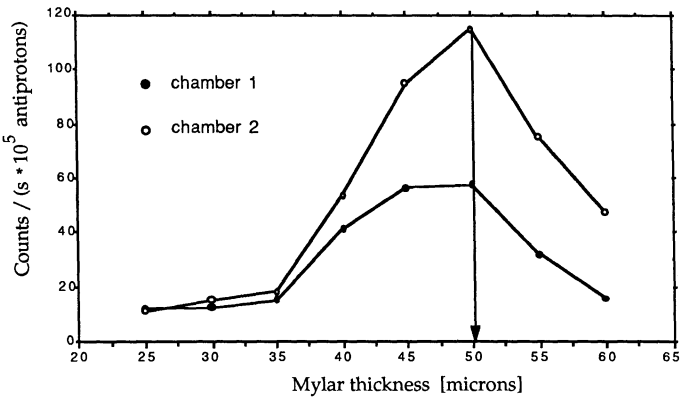

Fig. 3.9 : The number of counts per second in the two PPAC detectors as a function of the thickness of the variable Mylar degrader. Fragments from antiproton annihilations in uranium. The thickness chosen, 50 μm, is indicated by the vertical arrow.

The thin targets used in this experiment made the antiproton stopping rate sensitive to even very small variations in the beam momentum. Therefore, a variable degrader was placed in the antiproton beam line just downstream of the box entrance foil. This degrader was composed of Mylar strips glued together and was adjustable in 5 μm steps from 25 μm to 60 μm

by a remote control step motor. Having a production target in place, the fission yield recorded in the PPAC detectors was used to monitor the antiproton stopping efficiency. The chamber count rate as a function of degrader thickness, i.e., the antiproton range curve, is shown in Fig. 3.9. The width is in this case about 16 μm (FWHM), in agreement with tabulated values (Jan 82). For this particular test, the optimum degrader thickness was set to 50 μm.

Assuming that the 50 μm Mylar degrader made the antiprotons come to rest in the centre of the target, one can estimate the beam momentum by the following procedure, where all the material between the target and the LEAR vacuum is taken into account :

Energy to penetrate the 220 μm CH_2 scintillator	3.83 MeV
+ -"- -"- -"- the 50 μm Mylar foil	4.43 MeV
+ -"- -"- -"- the 25 μm Kapton foil	4.70 MeV
+ -"- -"- -"- the 5 mm air gap	4.75 MeV
+ -"- -"- -"- the 100 μm Be window	5.86 MeV.

A kinetic energy of 5.86 MeV corresponds to an antiproton momentum of 105 MeV/c, in good agreement with the nominal beam momentum of 105.5 MeV/c. Similar calculations show that the momentum range covered by the 25 - 60 μm Mylar degrader is about 103 - 106 MeV/c.

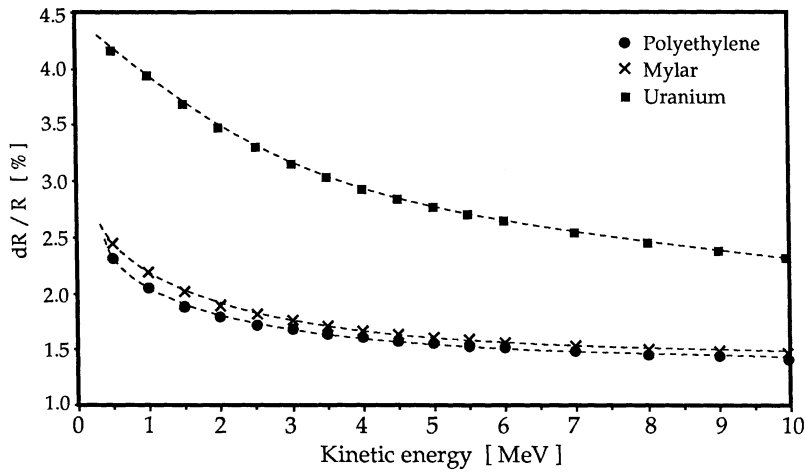

Fig. 3.10 : The relative range straggling in percent for protons as a function of kinetic energy. R is the mean range and dR is the range straggling. Values for polyethylene (CH_2), Mylar and uranium are plotted. Note that the vertical scale starts at 1 %. From Jan 82.

Using the methods described here, both the beam focussing and centring, as well as the degrader thickness, were continuously monitored during the running periods, with an interval of a few hours.

The fraction of antiprotons stopped in the target can be estimated under a few general assumptions. Firstly, the stopping power and range tables for protons are assumed to be valid also for antiprotons and secondly, the variable degrader adjustment is assumed to stop an antiproton of average energy in the centre of the target. The fluctuations in range, the straggling, of the antiprotons can be approximated by a normal distribution around the mean range, where the variance is given by (Seg 77)

$$V_{range} = \sigma^2_{range} = 4\pi \cdot z_p^2 \cdot N_a \cdot Z_a \cdot e^4 \cdot \int_0^{E_p} \left(\frac{dE}{dx}\right)^{-3} dE \qquad (3.2).$$

where N_a is the number of atoms per cm^3 in the absorber,
Z_a is the charge number of the absorber,
z_p is the charge number of the projectile,
E_p is the kinetic energy of the projectile.

Performing this integration for protons in a few different materials gives the range straggling as a function of kinetic energy as shown in Fig. 3.10 (Jan 82).

One can further assume that the normal shape of the straggling curve is kept when the antiprotons enter the actual target, but that the variance is modified according to the target medium. Thus, the standard deviation of the range distribution in the targets is given by $\sigma_U = R_U(E_0)$ and $\sigma_{Bi} = R_{Bi}(E_0)$ for uranium and bismuth, respectively. Here, R is the range and E_0 is given by $R_{CH_2}(E_0) = \sigma_{CH_2}$. Finally, performing the integration over the normal distribution gives the stopping efficiency (in percent) as

$$\varepsilon_{stop} = 100 \cdot \left(2 \cdot \int_0^{t(1/2)} N(0, \sigma_{target})\, dx \right) \; [\%] \qquad (3.3),$$

where $N(0, \sigma_{target})$ is the normal density function with zero mean and standard deviation σ_{target},
σ_{target} is σ_U or σ_{Bi},
$t(1/2)$ is half the target thickness.

Table 3.1 summarizes antiproton stopping rate calculations, performed in the manner described above, for four momenta close to the expected 105 MeV/c. Note, however, that in this table no loss of antiprotons due to multiple scattering is taken into account. The low beam momentum,

allowing for thin degraders, in combination with the compact geometry of the degrader and beam diagnostics system should make such losses almost negligible.

Momentum [MeV/c]	Energy [MeV]	ε_{stop} U [%]	ε_{stop} Bi [%]
95.0	4.80	1.41	1.55
100.0	5.31	1.23	1.34
105.0	5.86	1.07	1.16
110.0	6.43	0.91	0.98
200.0	21.1	0.14	0.15

Table 3.1 : Stopping efficiency in the target for five different beam momenta.

Table 3.1 also emphasizes the importance, in this experiment, of a low beam momentum to make efficient use of the antiprotons.

3.3.4 Parallel plate avalanche chambers.

3.3.4.1 Principle of operation.

The main detectors in the PS177 experiment are two position sensitive parallel plate avalanche chambers (PPAC), the detailed design of which will be covered in the next sub-section. This section gives a brief description of the operating principle of such chambers.

Basically, each parallel plate chamber consists of two planes of equally spaced wires placed halfway between a cathode and an anode plane, as shown schematically in Fig. 3.11. The gap between the electrodes is filled with a suitable gas, isobutane in this case.

Position sensitive PPACs and low-pressure multi-wire proportional chambers (MWPCs) have played an important role in heavy ion research in the last decade or so. They have proved to possess excellent timing and localization properties when exposed to heavily ionizing particles (See, e.g., Bre 82 , Sch 83 and Pei 83). Their low mass, making them more or less

transparent, together with the good timing has made them well suited as start and stop counters in time-of-flight measurements.

The fundamental processes governing the interactions of charged particles in gas-filled detectors have been treated extensively in the literature. For some reviews see, e.g., Sau 77 and Ric 74. Here follows only a short summary.

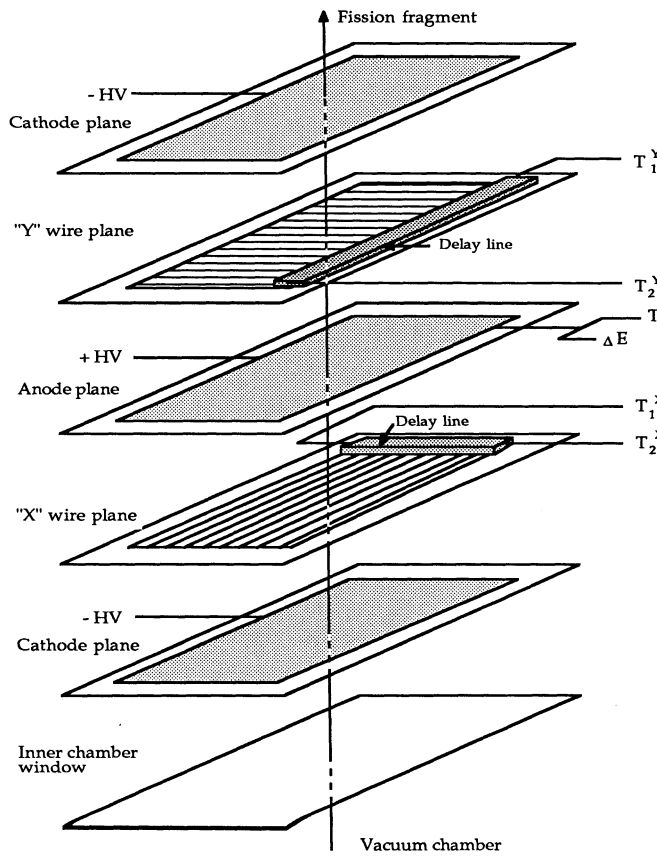

Fig. 3.11 : Exploded view of the PPAC detector used in experiment PS177.

When a charged particle traverses the gas volume of the chamber it will lose some of its energy through Coulomb interactions with the molecules of the gas. This energy is transferred to the molecules in the form of excitations and ionizations, the latter producing electron-ion pairs. The energy is shared

about equally between excitations and ionizations. The mean energy needed to produce an electron-ion pair differs from gas to gas ; for isobutane it is of the order 23 eV.

The produced pairs are separated by the applied electrical field and start to drift towards the electrodes. In general, the electrons move much faster than the positive ions, due to their small mass and large mean free path. The average velocity of the slowly moving ions is linearly proportional to the reduced field :

$$w^+ = \mu^+ \left(\frac{E}{p}\right) \tag{3.4}$$

where p is the pressure, and
μ^+ is the mobility (0.55 [$cm^2/(V\ s)$] for isobutane).

For the drift velocity of the electrons the following relation is valid :

$$w^- = \frac{e}{2\,m} \cdot E \cdot \tau \tag{3.5}$$

where τ is the mean time between collisions.

In turn, τ is a function of the pressure, p, and the electrical field, E. At high fields values of w^- around 5 cm/μs are typical for normal pressure.

In a PPAC, operated under low gas pressure, the reduced field between the electrodes, E/p, reaches a few hundred V/(cm Torr). In such a high reduced electrical field the electrons are accelerated to energies large enough to induce secondary ionization of the molecules of the gas. An amplification takes place, creating a swarm of electrons moving towards the anode. The number of electrons in the swarm grows exponentially with the distance, and the gain can therefore be given as :

$$G = \exp\left[\alpha\, d\right] \tag{3.6}$$

where d is the distance from the primary electron to the anode,
α is the first Townsend coefficient.

The coefficient α, being the average number of secondary electrons produced by a free electron per unit length, can be approximated by :

$$\frac{\alpha}{p} = A \cdot \exp\left[-B\left(\frac{E}{p}\right)^{-1}\right] \tag{3.7}$$

where A and B are gas specific constants. Typical gas gains of up to 10^4 can be achieved in low-pressure PPACs with an E/p of a few hundred V/(cm torr) (Ste 76). Due to the exponential character of the gain, the charges released closest to the cathode contribute the most to the final avalanche.

Hence, the time spread of the fast electron signal depends on the position of this first primary charge which gives an intrinsic time resolution of at best a few hundred pico-seconds (FWHM) (Bre 79). Due to the low pressure the positive ions can be collected relatively fast and consequently the problem of remaining space-charge, which reduces the count rate in a normal-pressure chamber, is much smaller in the low-pressure type.

The amplification process in a PPAC is totally different from that which takes place in MWPCs where the secondary amplification step takes place in the close vicinity of the chamber wires, as shown in Fig. 3.12.

The energy loss resolution of the PPAC is quite poor, typically a few tens of percent (Bre 79). This is mainly due to the statistical fluctuations in the amplification process. As stated earlier, the avalanche size is strongly influenced by the distance of the first primary charge to the cathode.

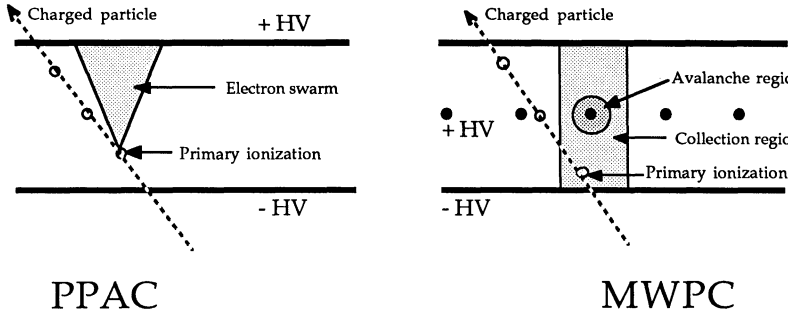

Fig. 3.12 : Working principle of PPAC and MWPC detectors.

It can be shown (Har 79) that when such an avalanche is collected on the anode it gives rise to an induced charge in the wires approximated by the expression

$$q_j \approx \cosh^{-1}\left[\pi \frac{(x' - x_j)}{D}\right] \qquad (3.8)$$

where q_j is the charge induced on wire j,
D is the gap between the electrodes,

x' is the true position of the avalanche close to the anode,

x_j is the position of wire j.

An example of the distribution of charges over a set of neighbouring wires is shown in Fig. 3.13.

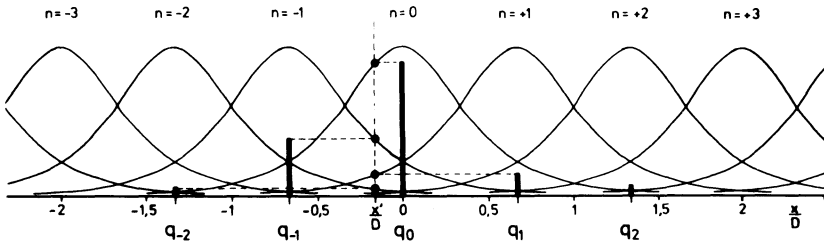

Fig. 3.13 : Distribution of induced charges on neighbouring wires by a charge moving at x'/D near the anode. The geometry is D = 3 mm and a = 2 mm. The black bars denote the position of the wires and the magnitude of the induced charge. From Har 79.

The position resolution one might obtain depends on the actual geometry of the construction. It is typically several hundred μm up to about one mm (Pei 83, Har 79).

The total charge induced in the wires will vary depending on the position of the avalanche, with a smaller charge induced for an avalanche occurring in the middle between two wires, as shown in Fig. 3.14a.

With a charge distribution described by eq. 3.8, the centre-of-gravity of an induced signal will give an estimated position of the avalanche, $\bar{x}$, which differs from the true position, x'. This results in an intensity modulation with the same period as the wire distance. As is shown in Fig. 3.14b, this variation in the intensity can be as large as ±18 % for a ratio wire distance, a, to electrode gap, D, of 2/3. The PS177 PPACs have an a/D ratio of 2.54/3.2.

When using large surface PPACs one has to be aware of the problems introduced by deformations of the electrode windows, caused by the electrostatic forces. Even small variations in the gap distance D can give large variations in the gain and can also affect the timing (Pei 83). However, in the PS177 application the differences in the gain are not considered serious since no very exact information is needed on this part. The differences in timing for different parts of the detector will cause variations of around or less than one ns (Eya 78, Har 79).

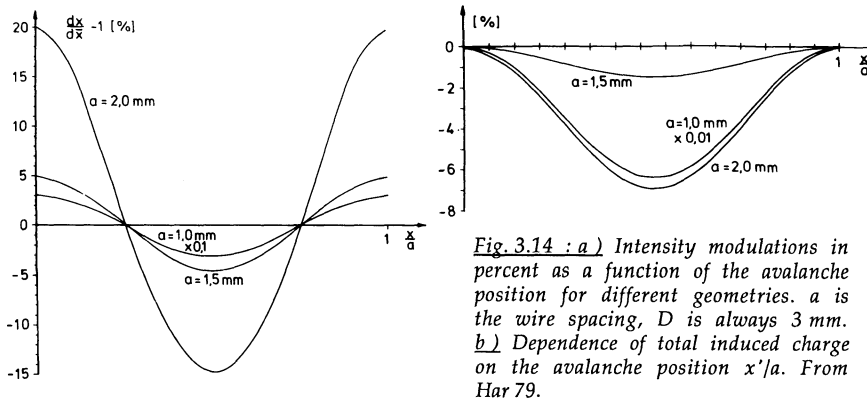

Fig. 3.14 : a) Intensity modulations in percent as a function of the avalanche position for different geometries. a is the wire spacing, D is always 3 mm. b) Dependence of total induced charge on the avalanche position x'/a. From Har 79.

3.3.4.2 *The PPAC detectors in the PS177 experiment.*

Two identical position sensitive parallel plate avalanche chambers have been used in the PS177 experiment. The geometry of the whole experimental set-up is described in section 3.3. Basically, each chamber provided information on the position and energy loss, ΔE, of the heavily ionizing particles passing through and also acted as one of the counters in the time-of-flight measurement.

Each chamber has a sensitive area of 190 x 290 mm^2 and the main features of their design are shown in Fig. 3.11. The anode and the cathodes are made of 2 μm thick aluminized Mylar foils. For the anode plane the aluminium layer covers both sides of the foil. The gap between the electrodes is 3.2 mm and halfway in between them a plane of 50 μm CuBe wires is placed, having a wire spacing of one tenth of an inch, 2.54 mm. This gives in total 74 long wires and 115 short wires per chamber. The two planes of each chamber measure two orthogonal directions, the wires of the inner plane placed vertically (x-direction) while the outer plane is placed horizontally (y-direction). A foil of 2 μm polypropylene acts as an inner detector window towards the vacuum of the fission chamber.

The chambers were operated with isobutane gas at a pressure of 7 mbar and with a high voltage of ±280 V on the electrodes. The wires were connected to ground. Each wire was connected to a tap of a delay-line of the type Pulse Engineering PE 20610, giving a delay of 2 ns per tap.

The fast electronic signal from the anode plane was sent via a pre-amplifier to a timing filter amplifier (ORTEC 454). This signal was then split into one part used in the energy loss measurement and a second part used as a start signal for the TDCs in the position determination and in the the time-of-flight measurement. In the latter case, the stop pulse was provided by the antiproton signal from the S1 scintillator. Signals from both ends of a delay-line were fed via pre-amplifiers to timing filter amplifiers (ORTEC 474) followed by constant fraction discriminators (CFD, Schlumberger 1326D). This eliminated the dependence on the amplitude of the delay-line pulse in the time definition . The logic CFD-pulse defined the stop signal for the TDCs which measure the position. See the next section for further details on the electronics.

The impact position in the chamber was given by measuring the difference between the two propagation times at each end of the delay-line. The sum of the two propagation times shows if the whole length of the delay-line has been traversed, thus providing a test for multi-fragment or other background events.

The performance of the chambers under experimental conditions is covered in chapter 4.

3.4 Data acquisition and electronics.

3.4.1 Data acquisition.

The most important task for the data acquisition system was to store the experimental information on magnetic tape for later use in the off-line analysis. It should also monitor the performance of the different parts of the experiment during data taking periods.

The block diagram in Fig. 3.15 presents the main components of the data acquisition system.

The electrical signals from the various detectors at the experimental site were transferred to the counting room by 45 m long standard BNC coaxial cables. Some of the signals from the detectors were split in two. After pre-amplification, one part of the signals from the PPAC anodes and from the S1-scintillator photomultiplier was, via a suitable delay, fed to an analogue-to-digital converter unit (ADC, LeCroy 2249) for pulse height analysis to give information on energy deposition. The second part was used for the fast trigger logic electronics (see next sub-section).

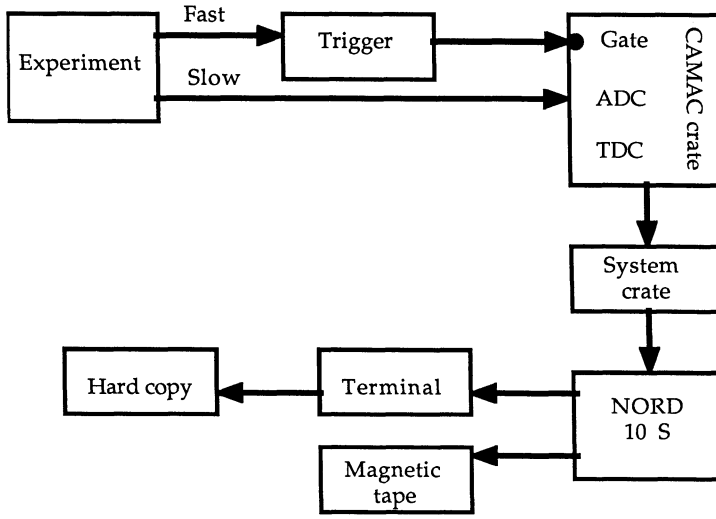

Fig. 3.15 : Block diagram of the components of the data acquisition system. The arrows indicate the data flow.

When the pre-defined trigger conditions were met, read-out was initiated by a LAM grader unit and the information from the experiment was transferred via DMA - direct memory access - directly to the host computer, a Norsk Data NORD 10 S. The most important task for the host computer was to copy the experimental information to magnetic tape. Some of the information was also directly processed and displayed to monitor the performance of the apparatus. A CERN standard program for NORD computers, the data acquisition system DAS (Bog 84a, Bog 84b), was used in this experiment. The sequence of read-out of the electronics in the CAMAC crate defined the order of the different data-words in an experimental event, as is shown by Fig. 3.16. The three-word event-head was added by the computer before writing on tape.

A hard-copy unit connected to the computer terminal allowed for the documentation of histograms and scatter-plots on paper.

The CERN standard input-output package EPIO was used to read the experimental tapes off-line.

Word #		
1	Event length : 40	Event header
2	Event identifier (1)	
3	Event number	
4	Pattern word	
5	PPAC X-11	TDC 1
6	PPAC X-12	
7	PPAC Y-11	
8	PPAC Y-12	
9	TOF 1 (PM 1)	
10		
11		
12		
13	PPAC X-21	TDC 2
14	PPAC X-22	
15	PPAC Y-21	
16	PPAC Y-22	
17	TOF 2 (PM 1)	
18		
19		
20		
21	PM 3 (Beam diagn.)	TDC 3
22	PM 2 (Beam diagn.)	
23		
24		
25		
26		
27		
28		
29	T0 1	ADC
30	T0 2	
31	PM 1	
32		
33		
34		
35		
36		
37		
38		
39		
40		

Fig. 3.16 : Event structure.

3.4.2 Electronics and trigger system.

The electronics used in the PS177 experiment consisted of standard NIM and CAMAC modules. A schematic drawing of the circuitry is shown in Figs 3.18a and b.

For each chamber, the signals from the PPAC delay-lines were connected as stop signals to a time-to-digital converter (TDC, LeCroy 2228) which was started by the fast T_0 signal from the chamber anodes (see Fig. 3.11).

The same TDC unit was also used for the time-of-flight measurement, in which case the stop signal was provided by a delayed signal from the antiproton counter, S1. In this arrangement the largest TDC channel numbers were attributed to the fastest projectiles and, conversely, that the slower projectiles were given lower TDC channel numbers. This situation is pictured in Fig. 3.17. Hence, to deduce an absolute time-of-flight it was necessary to know both the channel-to-ns calibration of the TDC and the position of the prompt peak in the TDC spectrum. This question is further discussed in section 4.2.

The role of the fast trigger is to initiate the read-out of the electronics when the information from the detectors indicate that an interesting event has occurred. Fig. 3.18 shows the circuitry of the fast trigger electronics. Only the main components are shown in this figure which means that, e.g., all delay units have been omitted.

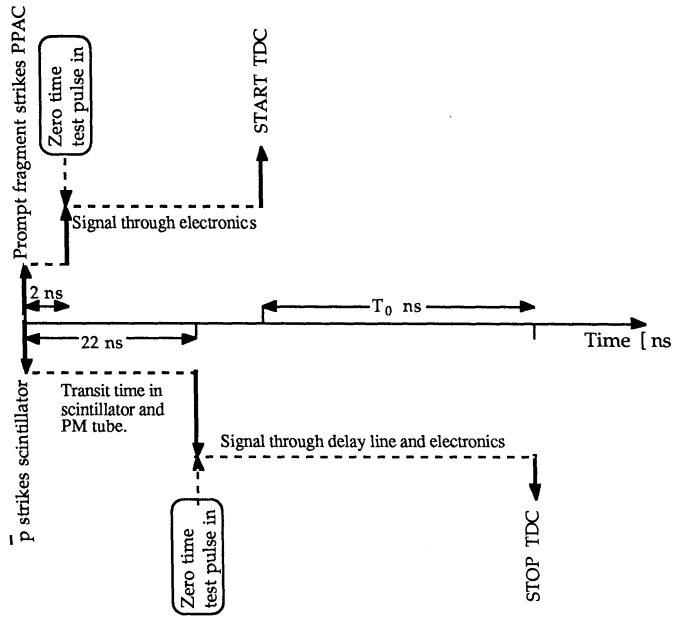

Fig. 3.17 : The time-of-flight measurement. The TDC is started by the PPAC signal and stopped by the antiproton scintillator signal. This gives an "inverted" time which is translated to an absolute time by the known position of the prompt peak, T_0, and the channel-number-to-ns calibration. Note that there is a 20 ns off-set in the prompt peak determination due to the different transit times in the detectors.

Two types of triggers were used for data-taking : the singles and the coincidence trigger. The singles trigger was defined as :

$$S1 \cdot (T01 \vee T02) \cdot \overline{Busy} \qquad (3.9),$$

where $\overline{Busy}$ denotes a computer generated signal, telling the system that the computer is not yet ready to accept another event. The T0-signals are the PPAC anode pulses, defined in Fig. 3.11.

The coincidences trigger was defined as :

$$S1 \cdot (T01 \wedge T02) \cdot \overline{Busy} \qquad (3.10).$$

This latter type of trigger was only used in connection with the two runs of July 1986. See Table 5.1 for a run period summary.

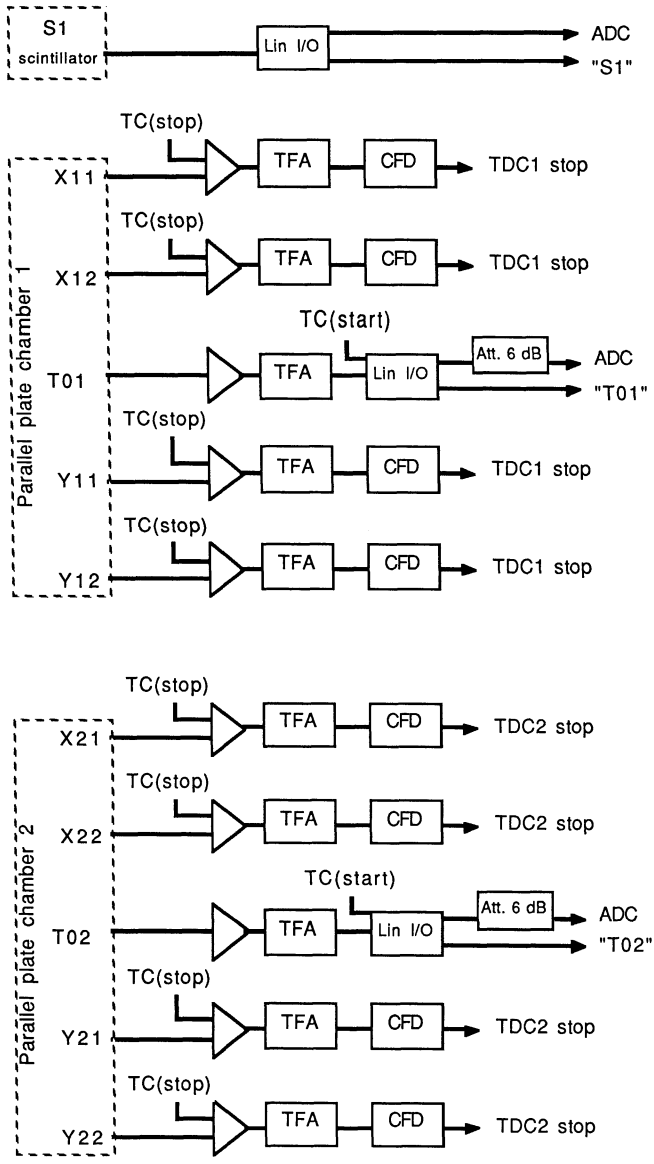

Fig. 3.18 : a) Electronics circuitry. Distribution of analogue (ADC) and TDC stop pulses. TC(stop) and TC(start) indicate where the time calibration pulses were connected. The electronics for the three trigger pulses "S1", "T01" and "T02" are continued in Fig. 3.18b).

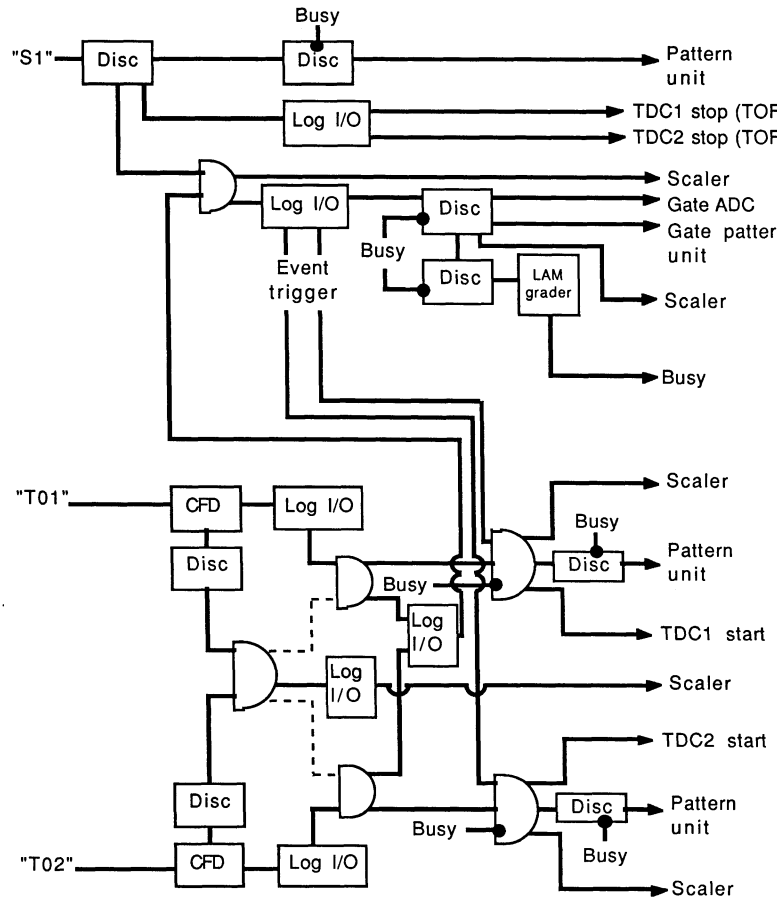

Fig. 3.18 : b) Electronics circuitry. The fast trigger logic. See Fig. 3.18a) for the origin of the pulses "S1", "T01" and "T02". The dashed connection lines were only activated for the coincidence trigger.

Chapter 4 : PERFORMANCE OF THE DETECTOR SYSTEM.

This chapter describes the performance and calibrations of the various detector components. The interpretation of the signals from the detector system depends to a large extent on a correct understanding of the energy deposited by different types of particles in different parts of the apparatus. Therefore, the first section of this chapter gives a short description of the energy losses inflicted on the particles participating in the reactions of this experiment.

In conclusion, it is shown that by imposing certain cuts, the PS177 detector system can be used to make an unambiguous selection of fission fragments.

4.1 Energy loss considerations.

4.1.1 Energy loss in the target.

The kinetic energies of fission fragments are typically in the range of 0.1 to 1.0 MeV/amu, where the light fragments have a somewhat higher energy than the heavy ones due to momentum conservation in binary fission (Fig. 2.19b). The range of various heavy ions in a number of different materials can be extracted from the tables of Northcliffe and Schilling (Nor 70) and from the handbooks edited by Ziegler (Zie 80, Lit 80).

The effects of energy loss on typical fission fragments can be evaluated by studying the nuclides ^{107}Ag and ^{142}Nd. These correspond to the two peaks in the asymmetric mass distribution of fission fragments from ^{252}Cf (Fig. 2.19a), later used as a calibration source (see sub-section 4.4.1).

Fission fragments are in general only marginally affected by the passage through the target material. For light fission fragments the range is about 10 mg/cm^2 in uranium whereas for the heavy ones it is about 8 mg/cm^2 (Lit 80). This should be compared to the target thickness of 0.1 mg/cm^2. Only for fragments with trajectories making an angle of less than one degree to the target surface does the energy loss become significant. This corresponds to fragments striking the parallel plate detectors within 5 mm of the target projection line.

For the heavy recoils, about to undergo delayed fission, the situation is less clear. Experimental data on the energy loss of heavy ions with mass

around 200 amu and higher in heavy targets are extremely scarce. The total recoil energy is in this case presumably only a few hundred keV (see section 5.1 for a further discussion on this point). Using the computer program suggested by Ziegler (Zie 85) gives an estimate of the ranges of these heavy ions, as plotted in Fig. 4.1. In this case the projectile is a ^{200}Hg ion, moving in bismuth, but a plot for the energy loss in uranium looks very similar. Clearly, a large fraction of the recoils with kinetic energies below about 1 MeV, coming from within the target, will not have sufficient range to penetrate the 100 μg/cm^2 target.

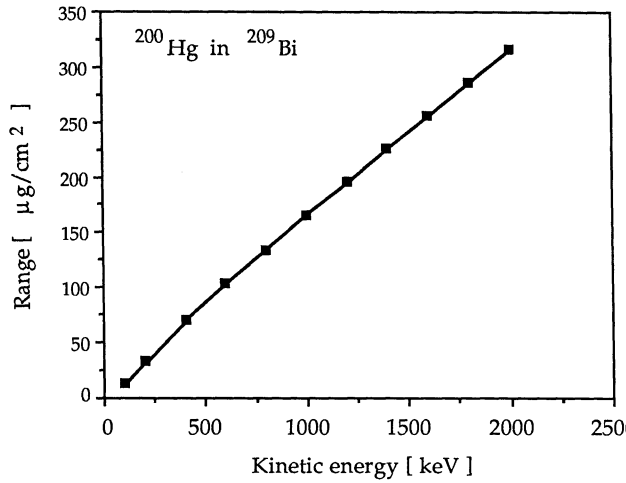

Fig. 4.1 : The approximate range of low-energy ^{200}Hg ions in ^{209}Bi.

The implications of energy loss and range for the detection efficiency determination are further discussed in sub-section 5.2.1.

4.1.2 Energy loss in the PPAC detectors.

The construction of the parallel plate counters as well as the interpretation of the data requires an understanding of the energy loss experienced by fission fragments traversing the foils and gas-volumes of the chambers.

A 105 MeV ^{107}Ag ion has a range of about 18 μm (2.5 mg/cm^2) in Mylar, for an 80 MeV ^{142}Nd ion the range is about 15 μm (2.1 mg/cm^2). Moving perpendicular to the detector planes, a fragment has to penetrate a total foil

thickness of 6 μm to be detected in both the x- and y-measuring volumes of the PPAC chamber (see Fig. 3.11). As will be shown later, the energy loss in the gas volume itself is negligible in this context. Hence, the chambers are well designed for registering fission fragments. Since α-particles from competing decay processes invariably accompany fission fragments when using a ^{252}Cf source, the range of 6 MeV α-particles is interesting for comparison. In Mylar it is about 39 μm.

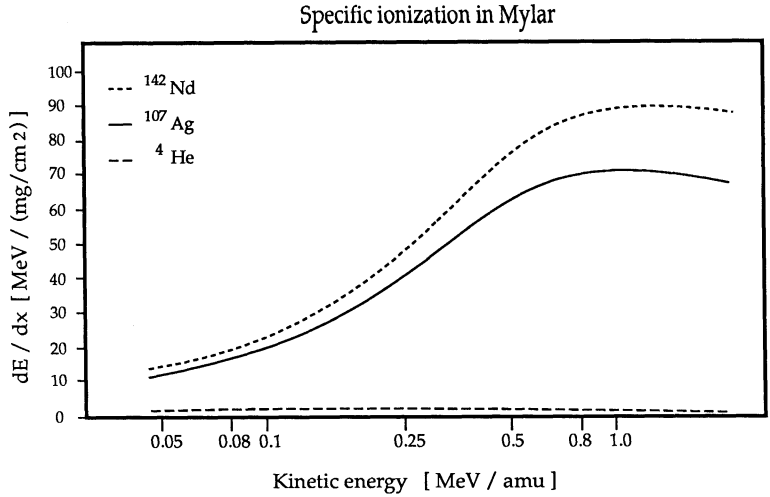

Fig. 4.2 : Specific ionization for different heavy ions in Mylar. Data from ref. Nor 70.

In Fig. 4.2 a plot of specific energy loss in Mylar is shown for the two nuclides discussed above. The data are taken from the tables of Northcliffe and Schilling (Nor 70). The energy loss of α-particles has also been included in this figure.

Fig. 4.2 clearly shows that in the energy range considered there is a positive correlation between kinetic energy and energy loss : the higher the energy the higher the energy loss. This correlation is even more pronounced for the fragments actually detected in the gas volumes of the PPAC, since part of their energy is lost when passing the detector foils.

Table 4.1 summarizes a calculation of the successive energy losses of the two fission fragments as they pass through the chamber. For comparison, an energy loss estimate for a 6 MeV α-particle has also been included. In Table 4.2 is shown the expected energy loss of the same fragments when

passing through the gas-volumes of the chambers. It should be noted that the lighter, faster fission fragments deposit more energy in the gas of the chamber than the heavy, slow fragments. Note also that the energy deposited by the α-particles is only about 2 % of that lost by the fission fragments.

	Inner chamber window *		1st Mylar foil		2nd Mylar foil		
	E_{kin} [MeV]	ΔE	E_{kin} [MeV]	ΔE	E_{kin} [MeV]	ΔE	E_{kin} [MeV]
$^{142}_{60}Nd$	80	19	61	20	41	15	26
$^{107}_{47}Ag$	105	17	88	20	68	19	49
$^{4}_{2}He$	6.0	0.17	5.8	0.22	5.6	0.23	5.4

Table 4.1 : Successive energy losses, ΔE, experienced by typical fission fragments and α-particles when passing through the PPAC foils. The tables of Northcliffe and Schilling (Nor 70) have been used.

**) Tabulated values for $(CH_2)_n$ used.*

The numbers presented in the two tables, 4.1 and 4.2, are only approximate. The reasons for this are, firstly, that the exact composition of the individual materials has not always been used and, secondly, that the tabulated dE/dx-values differ by about 10 % between different compilations. The latter fact can be seen by comparing the tables of Ziegler (Zie 80) and the ones of Northcliffe and Schilling, used in this calculation. The lack of precision is, however, of no great importance in this application, due to the poor energy resolution of the PPACs.

The results of the study presented here clearly shows that

1) the chambers are transparent to typical fission fragments,

2) the energy deposited in the chamber gas-volumes by typical fission fragments is about 50-100 times higher than for 6 MeV α-particles,

3) a larger ΔE signal can be expected for the light, fast fission fragments than for the heavy, slow ones. This is particularly true when the energy losses in the chamber foils are taken into account.

	Inner volume "x"		Outer volume "y"	
	E_{kin} [MeV]	ΔE	E_{kin} [MeV]	ΔE
$^{142}_{60}Nd$	41	0.39	26	0.28
$^{107}_{47}Ag$	68	0.52	49	0.49
$^{4}_{2}He$	5.6	0.0062	5.4	0.0064

Table 4.2 : Energy loss of typical fission fragments and α-particles in the gas-volumes of the PPAC detectors. The density of isobutane is 2.67 [mg/cm^3] at 1 atm, 0° C. Tabulated values for $(CH_2)_n$ are used. Data from Nor 70.

4.2 Time calibration.

4.2.1 TDC-calibration.

In this experiment both the position and the velocity measurements depend on timing information. The correlation between TDC channel number and time is directly used in the time-of-flight assignments. It is also important that the calibrations of the two TDCs, timing the signals from each end of a chamber delay-line, are well known. Possible differences in these calibrations have to be taken into account to get reliable position and resolution information.

The calibration was made by feeding a signal from an ORTEC 462 time calibrator unit through parts of the electronics. The calibrator start pulse simulated the fast timing signal from the chambers and was connected at position "TC(start)" in the electronics scheme (see Fig. 3.18a). The calibrator stop pulse was distributed to simulate all the pulses from the various delay lines, indicated by the "TC(stop)" in Fig. 3.18a. The period of the pulser was set to 10 ns and its range to 0.64 μs. This procedure gives a TDC spectrum with sharp peaks separated by 10 ns in time. Fig. 4.3 shows the TDC channel numbers of the peak positions versus time for a typical calibration run.

A line fitted to the data of Fig. 4.3 reveals that the deviations from a straight line for the individual peak positions are very small indeed, and the slope gives the required channel to time calibration. These calibrations were performed in each run and were subsequently used in the event evaluation.

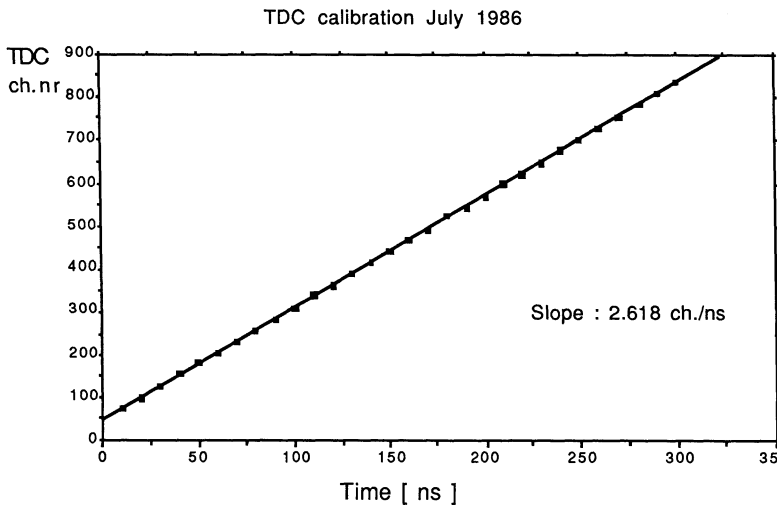

Fig. 4.3 : TDC calibration. Channel number of calibration peak versus time.

4.2.2 Zero-time (prompt) peak position.

To convert the registered TDC information to a real time-of-flight it is necessary both to know the channel to time calibration and to define the position of the zero-time (prompt) peak in the spectra. The latter task was performed by feeding a pulse from the time calibrator simultaneously to the two fast timing (anode) outputs of the chambers and to the output of the photomultiplier (PM) base connected to the antiproton beam scintillator, S1 in Fig. 3.7. In this way all the cable and electronics delays affecting the timing signals were taken into account, except for the transit time in the chamber anodes (approximately 2 ns) and in the photomultiplier (about 22 ns according to the photomultiplier specifications). Thus, an extra 22 - 2 = 20 ns had to be added to the measured position of this peak (see Fig. 3.17).

Fig. 4.4 shows the raw TDC spectra for the two chambers with the prompt (zero-time) position indicated by the dashed, vertical line. These data were

recorded while stopping antiprotons in a ^{238}U target. Due to the arrangement with the start/stop signal, time is running from right to left in this figure. The lower scale in Fig. 4.4 gives the time-of-flight in ns for this particular run. The independently measured zero-time position coincides exactly with the sharp cut-off in the TOF distributions.

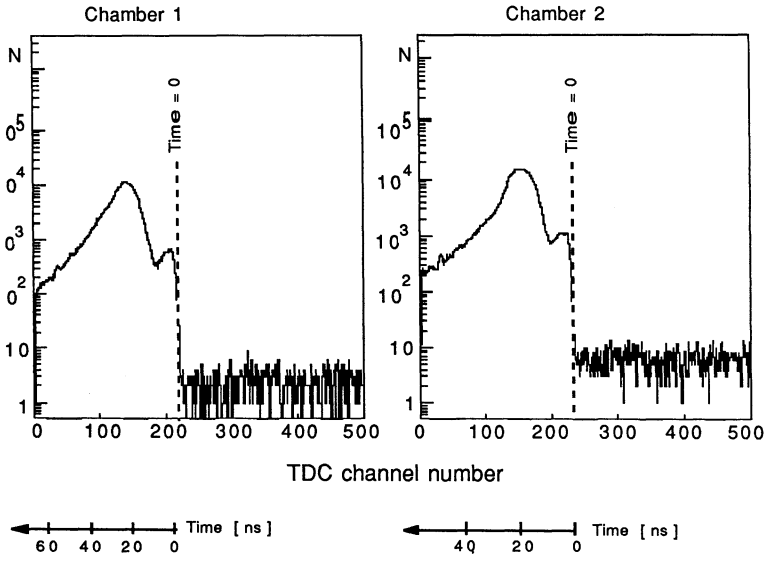

Fig. 4.4 : TDC spectra with zero-time position indicated by the dashed line. Lower scales show time in nano-seconds, as given by the TDC calibration. Note that time is running from right to left in the figure. Spectra of single fragments from antiproton annihilations in uranium.

4.3 Position calibration and resolution.

4.3.1 Position coordinate calibration.

Having checked that no correction is needed due to differences in the calibration of any pair of TDCs on the same delay-line, one can use the TDC information directly to give the fragment position and position resolution. Subtracting the two TDC numbers from each end of a delay-line gives the fragment position, adding them together gives a possibility to discard background events.

Assume that the times registered at the two ends of a delay line are $T_1 = t_1 + \Delta t$ and $T_2 = t_2 + \Delta t$, respectively, where t_1 and t_2 are the transit times in the delay line and Δt is a common time off-set. Then

$$T- = T_1 - T_2 = t_1 + \Delta t - (t_2 + \Delta t) = t_1 - t_2 \quad \text{and}$$
$$T+ = T_1 + T_2 = t_1 + \Delta t + (t_2 + \Delta t) = t_1 + t_2 + 2\,\Delta t \qquad (4.1)$$

Hence, the TDC difference, $T_1 - T_2$, directly corresponds to a position coordinate. It can also be seen from eq. 4.1 that a small time off-set, which might be introduced for various reasons (see sub-section 4.3.2), does not influence the position coordinate determination. It tends, however, to broaden the distribution of summed times, thereby introducing a small uncertainty in the background rejection.

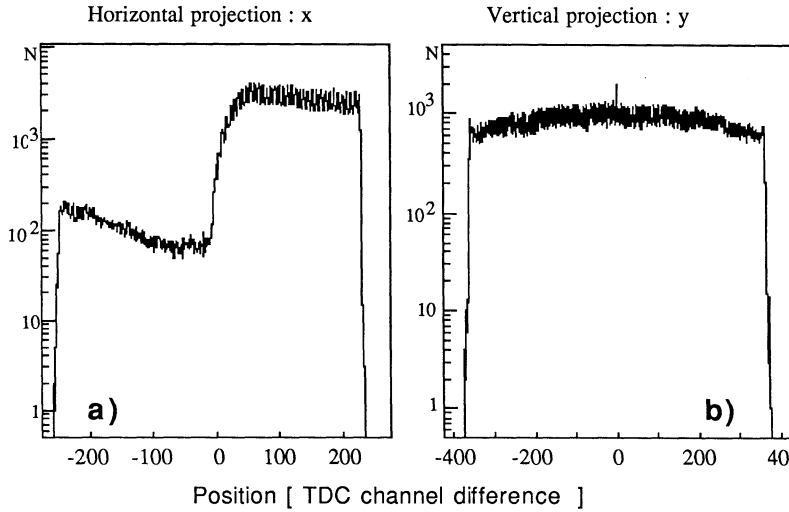

Fig. 4.5 : Singles distributions in one of the PPACs. a) is the horizontal projection (along the beam axis), x. b) is the vertical projection, y. Data from antiproton annihilations in uranium.

A typical example of a singles raw distribution projected along the beam-axis (the horizontal projection) is shown in Fig. 4.5a, and the corresponding position distribution in the vertical projection is shown in Fig. 4.5b. The edges of the chambers are clearly defined in these distributions, and in

Fig. 4.6 they are shown in a magnified scale for the horizontal case. The extremes of the chambers are taken as the positions where the number of counts has dropped to half of that at the plateau inside the chamber to take into account the finite position resolution. These positions are marked as full-drawn, vertical lines in Fig. 4.6.

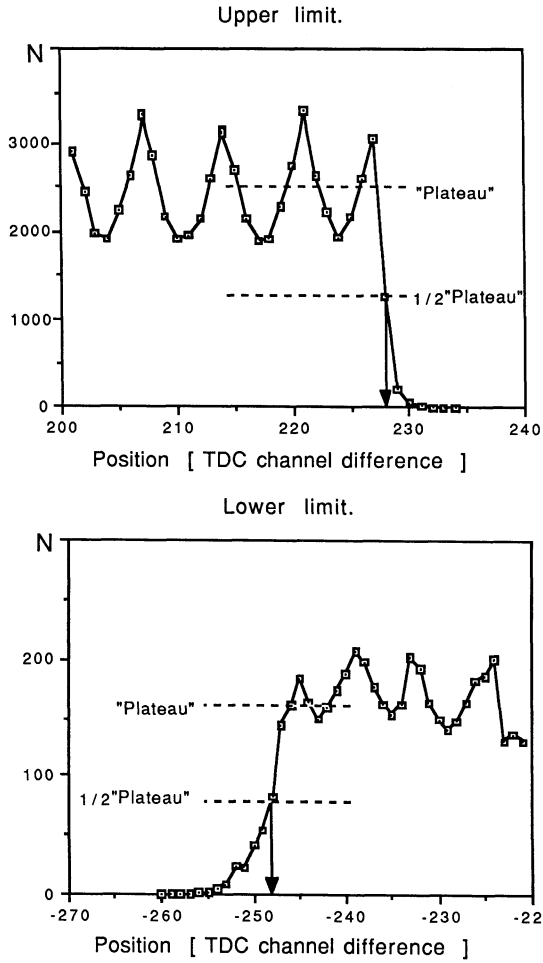

Fig. 4.6 : Magnified view of the position distribution at the chamber edges in the horizontal projection. See Fig. 4.5 for full view. The limits of each chamber are defined as shown by the full drawn arrows. The oscillating structure of the "plateau" is discussed in sub-section 4.3.2.

The limits of the chambers in each coordinate direction immediately gives the correspondence between TDC channel number and position. These position calibrations were performed in every run period and inserted into the event evaluation program.

To check that the channel to distance calibration was linear over the whole chamber a grid of known dimensions was placed in front of the inner chamber window. When exposed to fission fragments, a pattern of alternate bands with and without detected fragments was produced in the chambers. The positions and widths of these bands were consistent, within errors (see next sub-section), with the position calibration over the whole chamber width.

4.3.2 Position coordinate resolution.

The position resolution of a chamber of this type can, as explained earlier, be expected to be considerably better than the 2.54 mm wire spacing. This was checked by studying the chamber edges, Fig. 4.6. Ideally, these should be sharp, but due to the finite resolution of the chambers they are seen to be somewhat rounded off. The widths of these smeared edges give an indication of the position resolution. It was found that the resolution in the x-direction, ≈ 1.0 mm, was better than the resolution in the y-direction, ≈ 1.8 mm. This difference can partly be explained in terms of the energy loss experienced by fragments passing through the detector. Fragments in the outer, y-measuring, part of the PPAC have, on average, a lower energy than those traversing the inner, x-measuring, part. The larger inclination of the tracks at the y-measuring edge could also contribute to this effect.

These findings agree well with the 1 mm resolution found in previous experiments using the same chambers (Ris 88).

For a single fragment, the sum of the propagation times of the two pulses travelling to each side of the delay line should, ideally, be a constant. The reason is that the total delay experienced by a signal in the delay-line is independent of where the fragment enters the chamber. This fact can be used to discard multi-particle or uncorrelated fragment events.

In practice, several effects contribute to give the spectrum of summed propagation times a finite width. Firstly, the fragments have different impact positions along the wire. With a signal propagation speed of $2/3\ c$, this gives a timing spread of about 3 ns for the long wires and about 2 ns for the short ones. Other contributions come from the small difference in TDC

calibrations and non-linearity in the delay-line as well as different charge collection times on the electrodes. There is also a finite transit time for the start pulse through the anode and this will be different in different parts of the chambers. Finally, small deformations of the chamber windows and foils can lead to variations of around or less than 1 ns (Eya 78, Har 79) in the pulse propagation time.

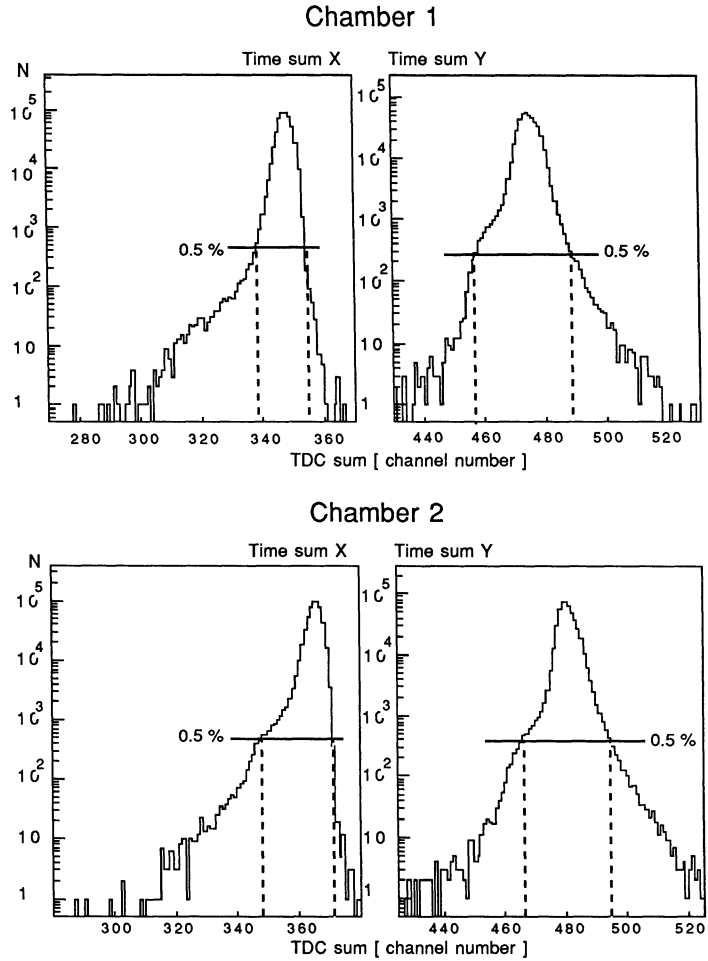

Fig. 4.7 : Time sum spectra for a ^{252}Cf test. The dashed lines indicate the window inside of which events are accepted. Note the logarithmic scale.

Consequently, one would expect the spectrum of summed propagation times to be composed mainly of one sharp peak, corresponding to the propagation time in the full delay line plus some mean propagation time in the wire itself. There should be no events with propagation time sums much greater than this. Background events of the multi-particle type as well as uncorrelated fragments should give rise to sums that are shorter than the full delay-line peak, except for very special cases.

The experimental distributions of summed times are plotted in Fig. 4.7 The vast majority of fragments fall inside a well defined peak (note the logarithmic scale). The widths of the peaks are about 3 ns (FWHM) for the sum in the x-direction and about 4 ns in the y-direction. Most of this spread can be understood in terms of variations along a wire. The fact that the larger width is observed for the shorter, outer wires can possibly be explained by the difference in specific ionization of the fragments in the x- and y-measuring parts of the detectors, as mentioned earlier. To exclude any dubious events, but still allow for the intrinsic time spread, a rather broad window was set around the peaks, corresponding to the position where the channel contents had fallen to 0.5% of the peak value, as shown by the dashed lines in Fig. 4.7. All events outside these windows were rejected from further analysis.

A periodic, oscillating structure can be observed superimposed in the position distribution (Fig. 4.6). A closer study shows that the period of this oscillation is equal to the distance between two wires. The experimentally found period is 2.55 ± 0.23 mm, in excellent agreement with the 2.54 mm wire distance given by the mechanical construction. As already mentioned in the previous chapter, sub-section 3.3.4, these modulations are due to the difference between the estimated centroid of the pulse from the wires and the true position of the avalanche on the anode (Har 79). In general, this structure can be reduced by reducing the ratio a/D, where a is the wire spacing and D is the gap between the electrodes. The clear resolution of this oscillation again shows that the error in the position determination is indeed smaller than the 2.54 mm wire distance.

Due to the rather limited statistics available, it was not considered meaningful to use the 1-2 mm position resolution for binning. To exclude the possibility of introducing any artificial structure into the position distributions, the experimentally found wire distance of 2.55 mm was used as the basic unit when finally binning the data for evaluation purposes. As will be seen in the next chapter, 4 x 2.55 mm bins were used for the analysis

of the delayed fission events, and 2 x 2.55 mm bins for the more numerous prompt fission events.

4.4 Response to fission fragments.

Fission fragments have characteristic properties that make them easy to distinguish from other types of ions. They are

1) heavy and have a high charge, making them highly ionizing when passing through matter,
2) fairly slow, with typical velocities around 1 cm/ns,
3) normally emitted in pairs, back to back in binary fission.

These properties are used in this work to separate fission fragments from other particles emitted in the antiproton annihilation process.

4.4.1 Fragments from ^{252}Cf.

To set the various parameters governing the response of the chambers to values optimized for the detection of fission fragments, several tests with a ^{252}Cf source were performed.

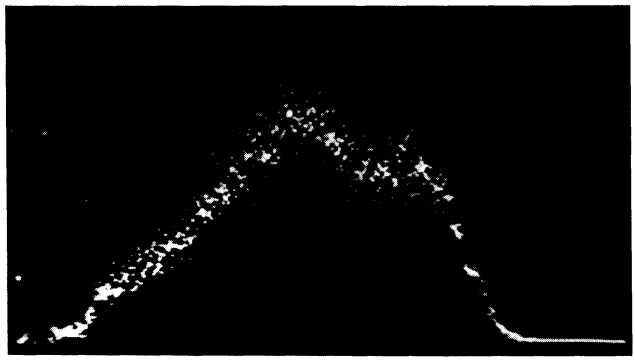

Fig. 4.8 : Energy spectrum of ions from the ^{252}Cf source used in the calibration, as measured by a solid-state counter. The vertical scale is logarithmic. The sharp peak at low ΔE contains the α-particles, the broader structure at high ΔE corresponds to fission fragments.

This radio-nuclide has two main decay channels of interest here. It is a strong α emitter, giving α-particles of an energy of about 6 MeV.

Additionally, in about 3 % of the cases, the decay will go through spontaneous fission. The mass and kinetic energy distributions of the fission fragments are shown in chapter 2, Fig. 2.19. Thus, this source is well suited to test the response of the chambers to typical fission fragments.

An energy spectrum of fragments from the ^{252}Cf-source used in the calibration, detected in a solid-state counter, is shown in Fig. 4.8. The sharp peak at small energies corresponds to the 6 MeV α-particles while the broader structure at higher energy is caused by the heavily ionizing fission fragments. Note that the ordinate scale in Fig. 4.8 is logarithmic.

A 6 MeV α-particle loses only a few keV in the isobutane gaps of the chambers. Typical fission fragments lose several hundred keV in the same volume. The discriminator levels were adjusted in such a way that no PPAC ΔE-signals were seen from the α-particles in the ^{252}Cf test runs. The chamber voltage, and thereby the gain, was set to a level where the full fission fragment energy loss distribution is included in the ADC range.

Fig. 4.9 showns a ^{252}Cf fission fragments ΔE spectrum, together with ΔE-spectra from reactions induced by antiprotons stopped in stainless steel and in ^{238}U. The poor energy resolution of the PPAC does not make it possible to separate the light and heavy fission fragments, corresponding to the asymmetric mass distribution of the ^{252}Cf fission fragments. The difference in ΔE-signal between fission fragments and other, lighter ions is nevertheless clearly visible.

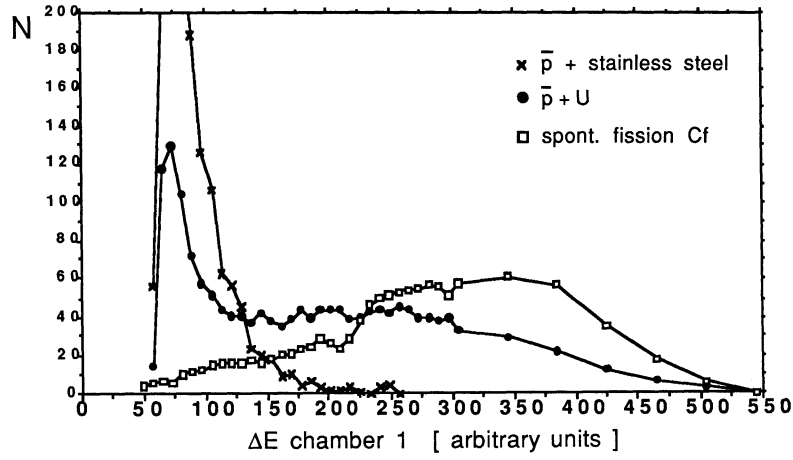

Fig. 4.9 : Energy loss of fragments of various origin registered in the PPAC detector.

Figs 4.10 and 4.11 show results from a test where the ^{252}Cf source was placed in the same position in the fission chamber as the targets in the antiproton runs. The californium material was deposited on a scintillator backing of the same dimensions as for the ordinary targets. This scintillator was then covered with a steel mask to ensure that particles from the ^{252}Cf decays were emitted only through a surface of the same size as that of the actual targets. The normal trigger conditions were imposed, requiring a signal from the scintillator, S1, and from at least one of the chambers. This trigger requirement, together with the thick steel mask, prevented the detection of almost all coincident fission fragments in this test.

Fig. 4.10 shows the velocity distribution of the fission fragments measured in the two chambers, as given by the time-of-flight and position for each fragment. The measured mean velocity is 12.7 and 12.2 mm/ns for chamber 1 and 2, respectively. This compares well with what is expected. Simple non-relativistic kinematics gives the velocity of the fragments as

$$\frac{v}{c} = \sqrt{\frac{2 \cdot E_{kin}\ [MeV]}{M\ [MeV/c^2]}} \qquad (4.2).$$

Thus, a 100 amu fission fragment with a kinetic energy of 100 MeV moves with a velocity of about 13.8 mm/ns.

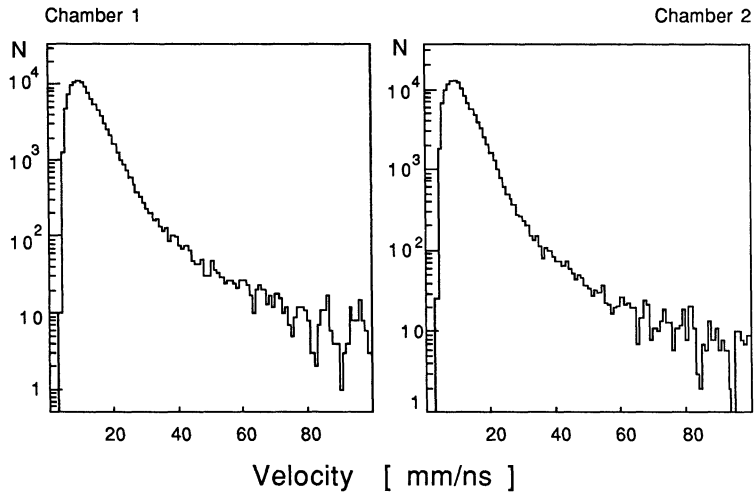

Fig. 4.10 : Velocity distributions of fragments from a ^{252}Cf source recorded in the two chambers.

A scatter plot of energy loss versus velocity for fragments from the ^{252}Cf source is shown in Fig. 4.11. In this and all the subsequent plots, the individual ΔE values have been normalized to correct for the path length traversed in the chamber. This should give a more correct $\Delta E/\Delta x$ assignment to the individual fragments. There is a clear positive correlation between the velocity and $\Delta E/\Delta x$: the higher the velocity the higher the energy loss registered. This behaviour can be understood qualitatively by studying the specific ionization curves for fission fragments in the appropriate energy range, taking into account the energy loss of the fragments in the chamber windows. Going back to section 4.1, Fig. 4.2 shows the energy loss as a function of kinetic energy for two different heavy ions, corresponding to fission fragments emitted in the decay of ^{252}Cf .

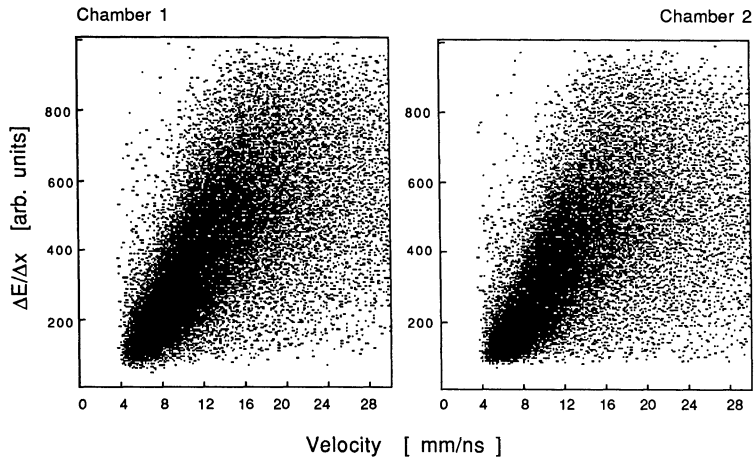

Fig. 4.11 : Scatter plot of $\Delta E/\Delta x$ versus velocity for ^{252}Cf fission fragments registered in the two chambers (singles).

The calculations in sub-section 4.1.2 show that the chambers are indeed transparent to fission fragments, even though the energy loss in the chambers can be considerable. The kinetic energy of fragments from ^{252}Cf, detected in the gas volumes of the chambers, range from about 0.1 MeV/amu up to about 1 MeV/amu, with the heavier fragments at the lower energy limit and the lighter ones at the higher. It is clear from Fig. 4.2 that one expects fission of ^{252}Cf to produce fragments which, after passage through the foils of the chambers, give an increasing energy loss with

increasing fragment energy, i.e., with increasing velocity. This is also what is observed experimentally.

4.4.2 Antiproton induced fragments - selection of fission fragments.

When targets intended for hypernuclear production are exposed to the antiproton beam one can expect the parallel plate chambers to be irradiated both by fission fragments and by other, lighter ions. These light ions originate from antiproton annihilation in material surrounding the actual targets, such as target backing, moderators and foils in the beam line as well as from other processes than fission in the target nuclei. Those parts of the apparatus which can be expected to be struck by antiprotons have been constructed from low Z material to reduce this type of background.

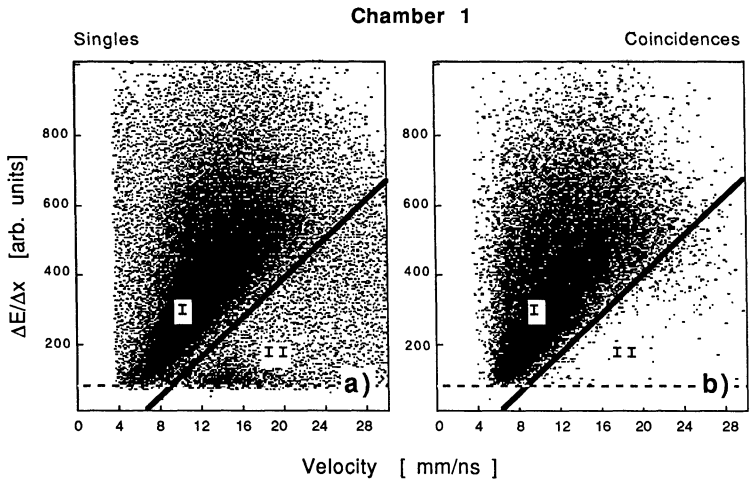

Fig. 4.12 : Scatter plot of $\Delta E/\Delta x$ versus velocity for fragments produced in antiproton annihilations in a uranium target, a) for singles and b) for coincident fragments.

Fig. 4.9 shows the ΔE-signals from one of the chambers when exposed to fragments of various origin. The separation between low mass, low Z - fragments and high mass, high Z - fragments is quite good. This figure also gives a clear indication that fission fragments are produced in antiproton annihilation in a uranium target. The spectrum obtained in this latter case consists of a mixture of the two others, exhibiting both the peak at low ΔE

and a broader structure towards high ΔE. The overlap in ΔE, in Fig. 4.9 in the region up to about 200 (arbitrary units), between different types of fragments is partly resolved when taking into account the velocity of each fragment. Looking at the scatter plot of $\Delta E/\Delta x$ versus velocity for fragments from antiprotons stopped in the uranium target, Fig 4.12a, one observes two well separated regions. The distribution of fragments in region I obviously corresponds to the fission fragments earlier identified in the ^{252}Cf tests. The fragments in region II, on the other hand, originate from antiproton annihilation in lighter nuclei, or fragmentation of the target nuclei, and thus constitute a background. By imposing a linear cut, indicated by the thick diagonal line in Fig. 4.12, fragments from region II can be rejected.

However, some background fragments remain, uniformly distributed over the region I in Fig. 4.12a. These events are rejected by imposing a coincidence requirement : only those events are accepted which are found in region I in both chambers. The effect of this requirement is shown in Fig. 4.12b. Note that in this figure, the linear cut has not yet been applied. In this case there still remain a few events in region II, which are subsequently removed by the linear cut.

Furthermore, a few fragments exhibit anomalously low $\Delta E/\Delta x$-signals. To rule out any contamination by random coincidences of light ions a threshold was imposed, indicated by the horizontal, dashed line in Fig. 4.12.

The probability of random coincidences of fragments in region I is very small. With a measured singles count rate of typically 60-70 per second and chamber, the random coincidence rate is

$$N_{chance} = 2 \cdot 60 \cdot 70 \cdot \Delta t \qquad (4.3),$$

where Δt is the coincidence gate width of 240 ns. Hence, this rate is about one coincidence every 8 min. This should be compared to a rate of about 90 registered coincidences per min. Moreover, this background of chance coincidences is almost entirely concentrated to the open area of the detectors. There also exists a possibility to further reduce the very small contribution of chance coincidences with one fragment in the shadowed region, as is explained in section 5.2.

The velocity spectra of true fission fragments from antiproton annihilation in uranium, selected according to the above presented procedure, are shown in Fig. 4.13. The mean velocity, 12 [mm/ns] for both

chambers, agrees well with what is expected for fission fragments from this reaction.

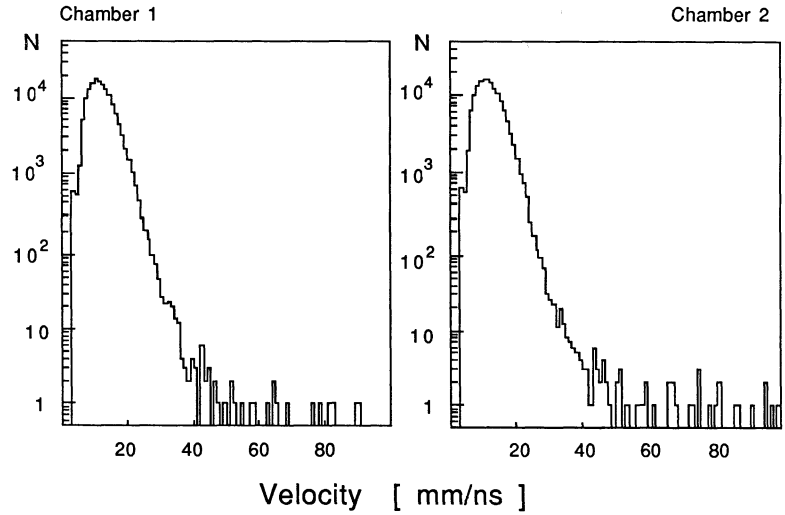

Fig. 4.13 : Velocity of selected fission fragments in the two parallel plate counters. Data taken while stopping antiprotons in a uranium target.

In conclusion, the methods described in this chapter make it possible to perform an unambiguous selection of fission events.

Chapter 5 : PHYSICS ANALYSIS.

The data presented in this thesis were collected during four different runs, involving two different target nuclei, as shown in the run summary of Table 5.1 below. The nominal beam momentum was 105.5 MeV/c for all the runs.

Date	Target (backing)	# p [$*10^9$]	# fission	time [h]
Sept.-85	^{238}U (10 mm)	0.96	14 100	--
Sept.-85	^{238}U (2.5 mm)	2.10	34 900	--
July-86	^{238}U (2.5 mm)	5.62	138 500	26.50
July-86	^{209}Bi (2.5 mm)	11.75	39 400	19.65

Table 5.1 : Run summary. The dimension indicated under "Target" is the backing width. The number of fission events are those remaining after all the cuts described in chapter 4 have been applied.

For the July -86 runs, most of the data were taken with a coincidence requirement in the electronics trigger. Only a small part of the uranium target run from this period used the singles trigger. All the runs using a 2.5 mm wide target backing were used in the delayed fission, i.e., hypernuclear, analysis. The run using the 10 mm wide target backing was used to check the recoil-distance method, as will be explained in sub-section 5.2.5.

The lower relative fission yield in September 1985 was due to a larger beam-spot size in these runs compared to the July 1986 runs.

The data analysis was performed on a μVAX computer at the Department of Radiation Sciences, Uppsala University, Sweden. The rather slow speed of this computer had some implications for the work as will be discussed later.

5.1 Analysis programs.

5.1.1 Event selection program.

The purpose of the event selection program is to separate true fission events from other types of fragmentation events, induced by antiproton annihilations in and around the target. In addition, the program should present the selected events in distributions that can be directly compared with the results of the simulation program, described in the next subsection.

The event evaluation program summarizes the properties of the chambers as determined by the calibration and the various detector tests. It also includes cuts which take into account the underlying physics processes. More specifically, the calibrations made independently of the data collection, such as the TDC calibration and zero-time measurements, are directly inserted into the program. Other parts of the calibration, e.g., the position calibration translating the delay-line TDC difference to a coordinate, makes use of the program in a first round after which also these numbers are fixed and taken as input for the subsequent physics analysis.

Various quantities which are calculated in the program, such as the velocity and the $\Delta E/\Delta x$ of the fission fragments, depend strongly on the calibrations performed.

In order to make a correct selection of true fission events, the data are fed through three types of cuts of increasing complexity:

1) First order, electronics cuts. These exclude any event from further evaluation which has an overflow or underflow
   - either in the delay-line TDCs
   - or in the ΔE-measuring ADCs.

2) Second order, instrumental cuts. Events are cut for which
   - the time-of-flight TDC has a value outside the physical range or
   - the sum of delay-line TDCs is outside the defined window.

3) Third order, physics cuts. These vary somewhat depending on what is presently studied, but in general, events that are kept must
   - pass a linear cut in the $\Delta E/\Delta x$ - velocity scatter-plot,
   - be subject to a threshold cut in the $\Delta E/\Delta x$ - distribution and
   - involve both chambers, i.e., be coincidence events.

This procedure provides samples consisting of only fission events. Further geometrical or other requirements finally define the conditions for each separate event sample.

5.1.2 Monte Carlo simulation.

It was shown already in the early work on the recoil-distance method (Met 74) that only under ideal conditions is it possible to calculate analytically the position distribution of the fragments originating from delayed fission events. If one wants to take into account the physical processes under study, as well as the experimental geometry and the detector performance, special programs which simulate the experiment have to be developed. One quite recent example of such a program, also using the so called Monte Carlo method, is described in Dor 86.

The details of the physical processes leading to fission and the precise geometry of the experimental set-up have been described elsewhere in this thesis. Here only the general outlines of the Monte Carlo program are given, with emphasis on the physics assumptions made. The case of delayed fission, i.e., decaying heavy hypernuclei, is treated first before describing the small and straightforward changes needed to adjust the program for prompt fission simulation. It should be stressed that no estimates on the relative yields of delayed and prompt fission are made in the Monte Carlo program; the two processes are treated separately.

Fig. 5.1 shows the main components in the simulation of a delayed fission event. Note that, for clarity, the dimensions of the target and the vector $\vec{H}$ are exaggerated in the figure.

The production point of the heavy hypernucleus is indicated by a P in the figure. Due to the fact that the LEAR beam had a width of about 2 mm both horizontally and vertically (FWHM) at the target position a square surface of dimension 2×2 mm^2 was chosen as the effective production area. A uniform distribution of production points over this area was assumed (dark shaded area in Fig. 5.1).

The direction of the outgoing hypernucleus, along the vector $\vec{H}$, was chosen at random from a uniform spherical distribution (CERN program library routine RAN3D). All hypernuclei recoiling in the negative x-direction, i.e., into the target, were considered lost. To gain efficiency, all events could therefore be given a positive x-component, resulting in

outgoing directions uniformly distributed over a half-sphere. This has no effect on the distributions as long as one is only interested in coincidences.

The length of the vector $\vec{H}$ is determined by the lifetime, τ, and the velocity of the hypernucleus. It is the aim of this work to estimate the values of these two quantities. However, in the case of the velocity two assumptions go into the simulation program.

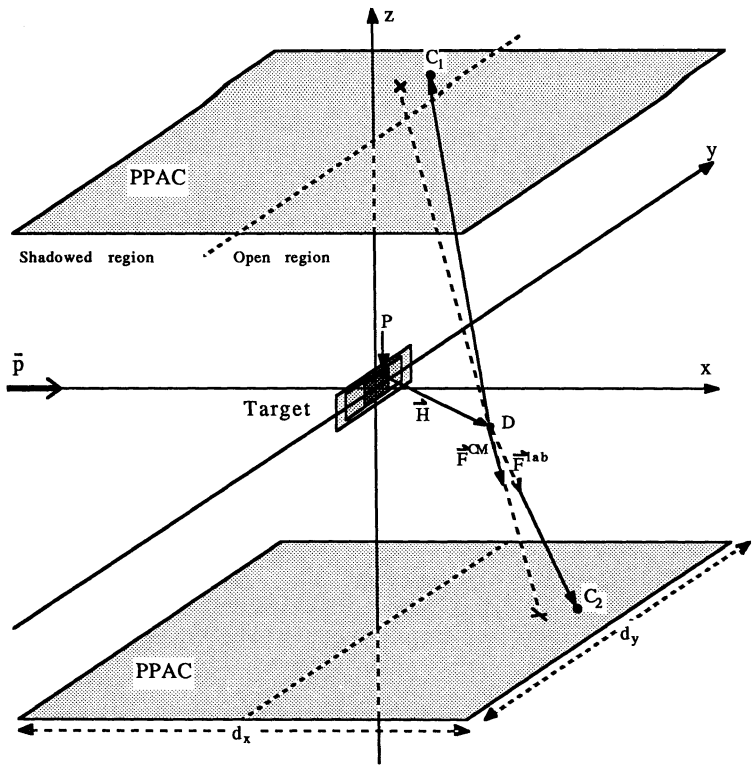

Fig. 5.1 : Schematic view of the experimental set-up. The main components of a simulated delayed fission event are shown. The figure is not to scale.

Firstly, an assumption about the mass of the formed hypernucleus has to be made. Some results on mass distributions after antiproton annihilation in heavy targets have been quoted in section 2.1. Especially the work by Angelopoulos et al. (Ang 88) seems applicable in this case. Here it is shown that each heavy nucleus loses on average about six neutrons, in a very short time after the annihilation. Applied to the targets used in this experiment

their result gives a mass of the heavy hypernucleus of 202 amu in the bismuth case and 231 amu for uranium, since one nucleon is lost in the initial annihilation. Furthermore, one can expect a few protons to be directly knocked out from the heavy nucleus. These are only rough estimates but, as is shown later in this chapter, sub-section 5.2.5, the final results are not sensitive to this particular input parameter.

Secondly, some assumption has to be made about the momentum distribution of the recoiling hypernuclei. A reasonable guess, considering the statistical behaviour of the annihilation, could be to use an exponential function, corrected to take care of the low-momentum part of the spectrum properly. This is the form favoured by intra-nuclear cascade calculations and it is also supported by some recent measurements on the recoil momenta of ^{3}He - and ^{4}He - particles emitted after antiproton annihilations in a wide range of target materials (Egi 88). The form finally introduced was

$$N(p) = p^{i/2} \cdot \exp(-p / p_0) \qquad (5.1)$$

where **i** is an integer,

p_0 is a constant, describing the width of the distribution.

This approach should be considered as purely phenomenological. A few different choices of i were tested as explained in sections 5.2 and 5.3. The constant p_0, as well as the lifetime τ, were treated as free parameters in the least-squares minimization. By using a slightly modified version of the CERN program library routine FUNRAN, each event was given a random momentum generated from an overall distribution of the functional form given in eq. 5.1.

The hypernuclear decay, leading to fission, takes place at position D in Fig. 5.1. In the simulation program, fission was considered to be binary and perfectly back-to-back in the mother nucleus' reference system. Apart from that, two main quantities are of interest here: the kinetic energy and the mass of the fission fragments. As was shown in section 2.3, the kinetic energy release in fission is almost linear in the Coulomb energy parameter, $Z^2 / A^{1/3}$. For a compound nucleus with A around 200, e.g., ^{200}Tl, formed in α-bombardment, the kinetic energy given to the two fragments is about 140 MeV, quite independent of the α-particle energy (Van 73). Similarly, for a compound system of $A \approx 230$ the kinetic energy release is 160 - 165 MeV, where the higher values correspond to higher excitation energies. The

values used here for this quantity were 140 MeV for bismuth and 160 MeV for uranium.

The masses of fragments from fission induced by energetic projectiles, corresponding to a high excitation energy of the fissioning nucleus, show a symmetric distribution (Fig. 2.19). Since the energy released in the decay $\Lambda + N \rightarrow N + N$ is of the order of 160 MeV it seems reasonable to assume that this type of mass distribution also applies to fission induced by the decay of heavy hypernuclei. To simplify things further, a constant mass of half the mother nucleus mass was assigned to each daughter fragment. As will be shown later, in Fig. 5.22 in sub-section 5.3.2, there is experimental evidence to support such an assumption.

Table 5.2 summarizes all the inputs to the Monte Carlo program concerning the fission process.

The directions of the emitted fission fragments, $\pm \vec{F}^{CM}$, are generated randomly from a uniform spherical distribution. Due to the recoil of the fissioning system, the opening angle between the laboratory directions of the fragments, $\vec{F}_1^{lab}$ and $\vec{F}_2^{lab}$, will deviate from 180°. Furthermore, the true decay point D is not known experimentally and the opening-angle distribution is therefore calculated using the vectors from the origin, i.e., the centre of the target, to the two impact points on the detectors, C_1 and C_2. For consistency, this is also the opening angle calculated in the Monte Carlo program. The difference to the true opening angle between the two fragment trajectories is very small, since the recoiling heavy nucleus only traverses a few tenths of a mm outside the target before decaying.

Target	Mass [amu] mother	daughters	Kinetic energy [MeV]
^{209}Bi	200	100	140
^{238}U	230	115	160

Table 5.2 : Fission process inputs to the Monte Carlo calculations.

The full geometry of the experimental set-up is implemented in the Monte Carlo program. Thus, any fragments striking the target arrangement,

as well as those intersecting the chamber planes outside their physical limits, are considered lost.

Applied to the prompt fission case, the main modification to the program is that the vector $\vec{H}$ is given a zero length. This takes into account the fact that prompt fission occurs in a very short time, about 10^{-18} s after the annihilation. Hence, all the prompt fission takes place inside the target itself. This further implies that, as already mentioned for the heavy recoils, any fragment with a velocity component in the negative x-direction, i.e., going deeper into the target, is considered lost. Since the kinetic energy release is only weakly dependent on the excitation energy, the values from the delayed fission analysis, Table 5.2, were also used for prompt fission simulation.

5.2 Delayed fission analysis.

This section describes the evaluation of the delayed fission events. Extracting the lifetime of the delayed fission process was the main goal of the analysis, and it is treated here in some detail.

The unambiguous selection of true fission events, delayed and prompt, was described in the previous chapter and the procedure was summarized in section 5.1. In all what follows the cuts described there have already been applied.

5.2.1 Detection efficiency.

With the geometry of the experiment given by the mechanical construction of targets, target backings, chambers etc., there are still a few factors left that determine the number of delayed fission events registered in the detectors :

i) The probability for the recoiling, heavy nucleus to escape from the target. This escape efficiency will depend on the momentum, mass, charge, production point, direction of motion etc of the heavy recoil. Some aspects of this were already discussed in sub-section 4.1.1.

ii) The PPAC detection efficiency.

iii) The spatial distribution of decay points, as given by the velocity and the lifetime of the fissioning nucleus.

Point i) above is only important if one wants to calculate the absolute yield of delayed fission events. As the emphasis here is on the

determination of the lifetime of the delayed fission process this problem has mainly been considered in the context of restricting the recoil angles of the escaping heavy nuclei, as will be discussed in sub-section 5.2.5. Moreover, this effect is to some extent taken care of by the phenomenological form of the momentum transfer distribution. Nevertheless, a rather simple calculation of the escape efficiency was made, based on the stopping power program suggested by Ziegler (Zie 85). This showed that about 30 % of all recoils - or about 60 % of those moving in the forward direction - escaped from the target into the fission chamber.

Point ii) is discussed at some length when the analysis of the prompt fission events is presented in section 5.3. For simplicity, in the analysis of the delayed fission events the chambers were always considered to be 100 % efficient.

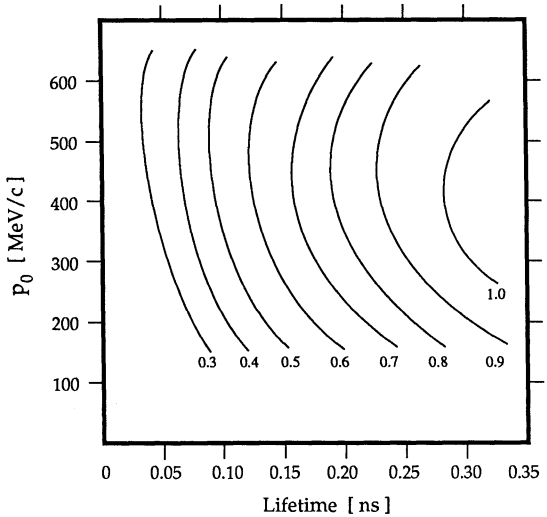

Fig. 5.2 : Delayed fission detection efficiency for uranium (2.5 mm backing) as a function of the lifetime and the p_0-parameter. The level of each curve is marked in percent. Straggling and multiple scattering in the target are ignored and the parallel plate chambers are assumed to be 100% efficient, the recoils are assumed to be isotropic over 4π solid angle and the escape efficiency is 100%.

The dependence of the detection efficiency on the velocity and the lifetime of the recoiling heavy nucleus can be studied with the Monte Carlo simulation program. The result of such a study is presented in Fig. 5.2, showing a contour plot of the efficiency when varying the lifetime and the width, p_0, of the momentum transfer function, eq. 5.1. Here the integer i was

set to 2 and the fission parameters were chosen according to the uranium case in Table 5.2. As expected, the detection efficiency increases with increasing lifetime. The efficiency for bismuth looks quite similar, although the curves are shifted somewhat towards lower p_0-values in that case.

The Monte Carlo study also shows that there are at least as many delayed fission events, where both fragments are registered in the open area as there are events with one fragment being recorded in the shadowed area and the other in the open area. Since there is no way, with the present detection system, to separate delayed and prompt fission events other than by purely geometrical methods, it is impossible to include the former type of delayed fission events in the analysis.

The probability of forming a hypernucleus is not taken into account in the calculation at this stage.

5.2.2 The target plane projection.

The only type of delayed fission event treated here is that for which one of the fission fragments has an impact position in the shadowed area of the detector. The separation line between the shadowed and the open area is given by the intercept of the extended target plane with the detectors, as is shown in Fig. 3.4. The accurate determination of the geometrical limits of these areas is therefore a crucial ingredient of the recoil-distance technique.

The method applied to fix the exact geometry of the experiment will now be illustrated for one special case, using the 1986 uranium target data. The same procedure was repeated for all the hypernuclear production runs.

The gross features of the position distribution in each chamber give a rough idea of the position of the target plane projection. Fig. 5.3 shows the interesting part in more detail for both chambers. Note the logarithmic scale. The centre of each chamber is indicated by a dashed line and the positions of the minima of the intensity oscillations, discussed in section 4.3, are shown by short, solid lines. The oscillating structure can be followed well into the low-populated area of the chamber, thus interfering with the structure caused by the shadow of the target backing. Nevertheless, a first guess where to find the target plane projection can be made by connecting the structure minima, as indicated by the solid lines in Fig. 5.3. This points to a position around channel -14 in chamber 1 and channel -8 in chamber 2.

To fix the separation line position, a preliminary least-squares test was performed. Each choice of the target plane projection line defines a different

experimental geometry and thereby a different delayed fission event sample. The least-squares method was applied to the position distribution in the shadowed area for each sample. The values of the global least-squares minima in the τ / p_0 - parameter space for the different projection line choices are plotted in Fig. 5.4.

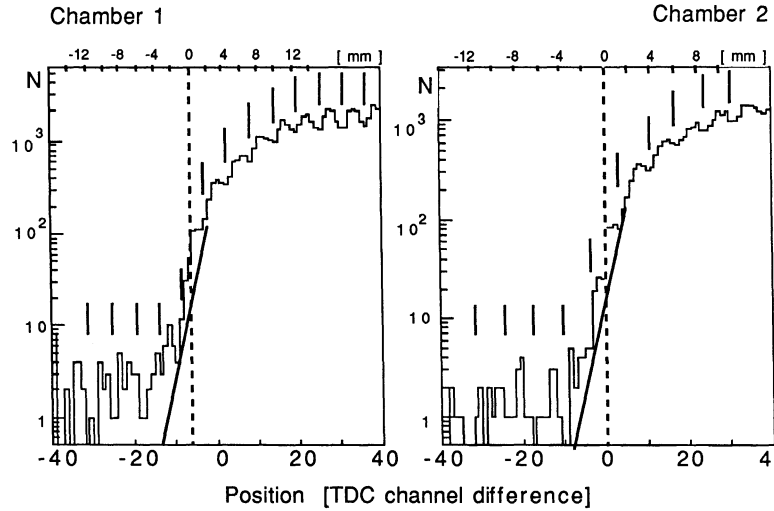

Fig. 5.3 : Position distribution of fission fragments projected along the experimental x-axis. The middle of each chamber is marked with a dashed line. Each minimum of the intensity modulation is indicated by a short, solid line. The long, solid line connects the two minima in the open region close to the open/shadowed area separation line, for each chamber. On top of each plot is indicated the scale in mm. Data from the uranium run in July 1986.

Clearly, channel -15 in chamber 1 and channel -9 in chamber 2 give the lowest minimum and can therefore be selected as the target plane projection for this run. Trying some of the "cross-combinations", such as -15, -10 or -14, -9, gives no lower minima. Of course, one still has to be aware of the fact that the finite position resolution might mix events of the delayed and the prompt type in the region closest to the separation line between the shadowed and the open area. This problem will be studied further in subsection 5.2.5.

In this way the dimensions of the open and shadowed areas for each chamber and run could be included into the simulation program. It was found that the target position was in general 2 - 3 mm upstream of the

middle of the chambers, making the open area slightly larger than the shadowed.

Comparing the position distributions for horizontal slices at the top and the bottom of the chambers, shows that the targets were in all runs placed in a perfectly vertical position. In the bismuth run of July 1986, however, the target was observed to be slightly rotated around the vertical axis, by about 0.3°. Included in the simulation program, this rotation produced no effect on the final results.

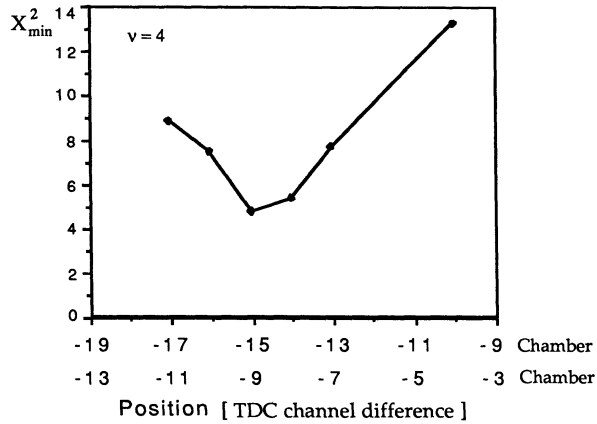

Fig. 5.4 : Least-square minimum for the shadowed region as a function of the position, in TDC channel number difference, of the separation line between open and shadowed regions. The number of degrees of freedom in the least-square calculation is 5. Data from the uranium target run in July 1986.

5.2.3 Event selection and cuts - experimental distributions.

Having fixed the geometry and, specifically, determined the separation line between the open and the shadowed areas, it is then a straightforward task to identify the delayed fission events. This is made simply by selecting those events with one, and only one, fragment in the shadowed area. Figs 5.5 and 5.6 show the position and opening-angle distributions of the selected delayed fission events from the three 2.5 mm backing runs (see Table 5.1), respectively. The separation line between open and shadowed regions, indicated by the dashed line in Fig. 5.5, defines the origin in the position distributions.

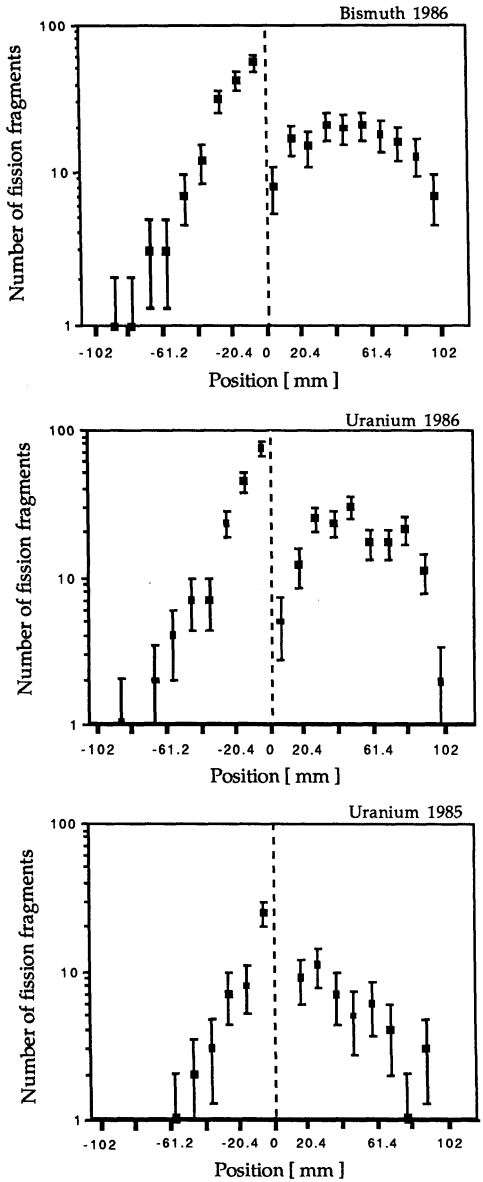

Fig. 5.5 : Position distribution for selected delayed fission events from all 2.5 mm target backing runs. The bin size is 10.2 mm. See Table 5.3 for more details.

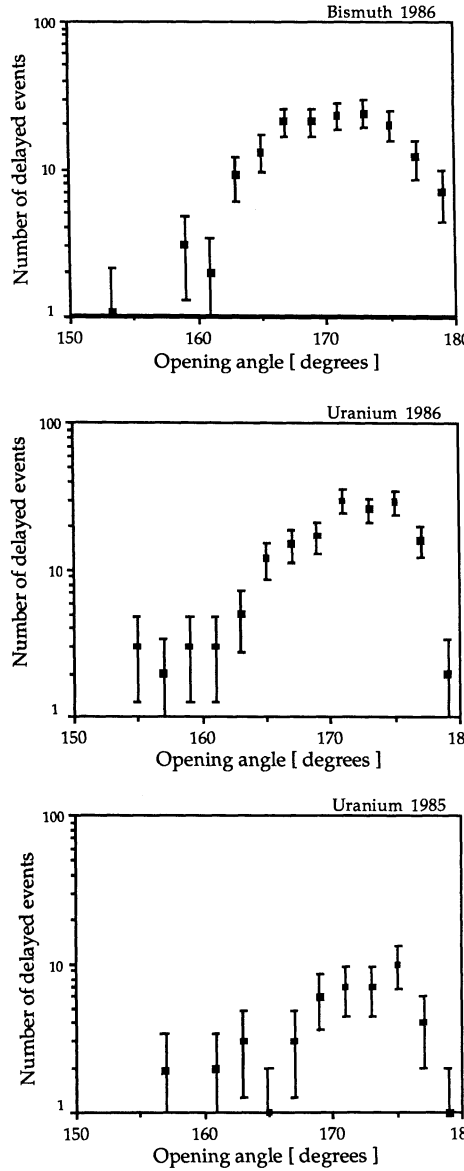

Fig 5.6 : Opening-angle distribution of selected delayed fission events for all 2.5 mm target backing runs. The data are binned by 2°. Table 5.3 gives the values for mean angle, rms width and number of entries.

The position distribution histograms are binned by 10.2 mm, corresponding to 4 x 2.55 mm, to avoid the introduction of any artificial structure due to the intensity oscillations. At the same time this binning gives a reasonable number of entries per bin.

The position distribution in the open area is given by the fragments accompanying those striking the shadowed area in a coincident event. The opening angle is defined as the angle, smaller than 180°, between the two vectors connecting the centre of the target with the two impact points in the detectors. The opening angle is calculated in the same manner in both the event selection program and in the Monte Carlo program.

One consequence of the recoil-distance technique is that every recoiling heavy nucleus, giving rise to a detected delayed fission event, has a momentum component in the positive x-direction (see Fig. 5.1 for the definition of the experimental coordinate system). If this is the only momentum imparted on the recoiling nucleus, and the subsequent fission is perfectly back-to-back, the impact position in the open area will be found further away from the open/shadowed area separation line than the correlated impact position in the shadowed area. However, examining the experimental distribution of the quantity

$$\Delta x = |x_{open}| - |x_{shadowed}| \qquad (5.2),$$

shown in Fig. 5.7, one notices that the distributions extend to negative Δx-values that are by far larger than what one would expect from, for example, the finite position resolution.

The shape of the Δx-distributions can be understood if one takes into account the weak decay process. In the underlying $\Lambda + N \rightarrow n + N$ reaction, responsible for the subsequent fission decay of the heavy nucleus, about 400 MeV/c momentum is given to each final state nucleon. In leaving, these nucleons interact with the residual nucleus, transferring excitation energy but also linear momentum. Monte Carlo studies show that an extra, isotropically distributed, momentum transfer of about 300 MeV/c, given at the instant of fission decay, can explain the shapes of the Δx-distributions.

At the same time, this effect had almost no influence on the final result of the parameters pertaining to the delayed fission process. Therefore, it was not included when performing the least-squares search for the lifetime parameter. The same Monte Carlo study, however, also shows that even in

the most extreme cases, with a recoil kick of several hundred MeV/c, it is very unlikely to get events with $\Delta x < -30$ mm.

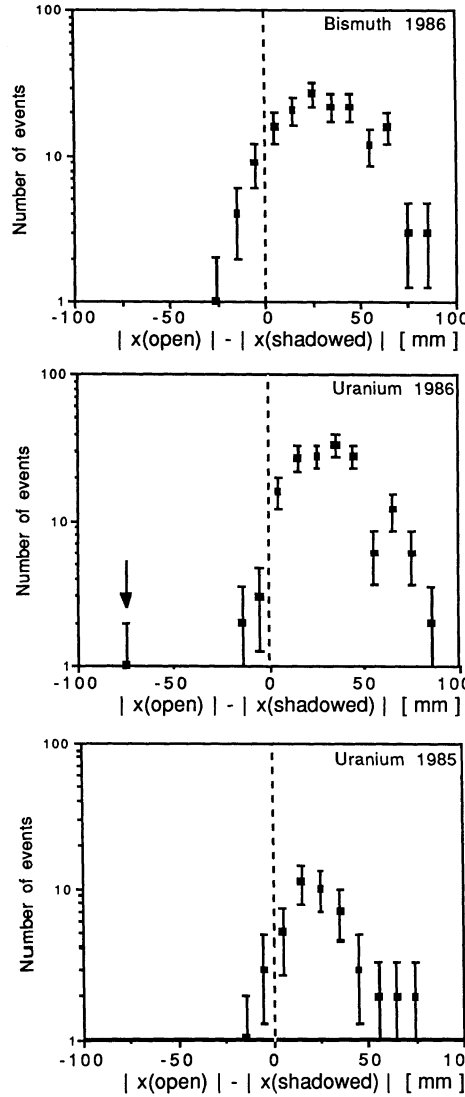

Fig. 5.7 : Δx-distributions for all 2.5 mm target backing runs. One event, indicated by the arrow, from the July 1986 uranium run, is rejected.

This then gives a possibility to introduce an extra cut for delayed fission events, rejecting any event with $\Delta x < -30$ mm. Only one experimental event, from the July 1986 uranium run, was rejected on these grounds. This event is indicated by an arrow in Fig. 5.7. The properties of the remaining events are summarized in Table 5.3.

Date	Target/ backing	# delayed fission	$\langle \Theta \rangle$ [degr.]	Θ_{rms} [degr.]
Sept.-85	100 $\mu g/cm^2$ U 10 mm	7	170.1	4.3
Sept.-85	100 $\mu g/cm^2$ U 2.5 mm	46	170.7	5.3
July-86	100 $\mu g/cm^2$ U 2.5 mm	163	170.6	5.1
July-86	100 $\mu g/cm^2$ Bi 2.5 mm	156	170.5	4.7
Sept.-85 + July-86	100 $\mu g/cm^2$ U 2.5 mm	209	170.6	5.1

Table 5.3 : Delayed-fission event selections for the four runs discussed in this thesis. The number of events, mean opening angle and rms width of the opening-angle distribution are given for each event sample. The properties of the combined sample of uranium data taken with the 2.5 mm target backing are shown below the wavy line.

5.2.4 Parameter search.

The least-squares method was adopted to extract physics information from the experimental distributions. The main principles of this method are explained in Appendix A. This sub-section describes how the least-squares principle was applied to the PS177 data.

The residual sum of squares, X^2, is given by eq. A1 in Appendix A as:

$$X^2 = \sum_{i=1}^{N} \left[\frac{y_i - f_i(\underline{\theta}; x_i)}{\sigma_i} \right]^2 \qquad \text{(A.1).}$$

This quantity has been calculated individually for three different distributions : i) X^2_{shad} for the position distribution in the shadowed area of the detectors, ii) X^2_{angle} for the opening-angle distribution and iii) X^2_{open} for the position distribution in the open area. The theoretical prediction, $f_i(\underline{\theta}\,; x_i)$, as well as the estimated error, σ_i, in each data point were given by the Monte Carlo simulation program (see section 5.1 for details). The Monte Carlo histograms were produced with 20 - 30 times more events than the experimental ones. Two parameters, τ and p_0, pertaining to the lifetime and the recoil velocity of the nuclei about to undergo delayed fission, respectively, were varied freely ; the principal aim of this part of the analysis was to get accurate estimates of these two quantities.

In general, one can expect the X^2 calculated from the position distribution in the shadowed area to be the one most sensitive to the lifetime parameter. In most experiments using the recoil-distance method no coincidences are recorded and, consequently, the position distribution in the shadowed area becomes the only source of information on the fissioning system. In our case, however, the opening-angle distribution gives additional information. This latter distribution can be expected to be especially sensitive to the velocity of the recoiling heavy nucleus at the instant of fission decay. In the analysis presented here the X^2_{open} is also studied, as an extra check on consistency.

The next four paragraphs present the details of the parameter search for the three 2.5 mm target backing runs.

5.2.4.1 September 1985 uranium data.

When applying the least-squares test to the uranium data of September 1985 it was found that, for the opening-angle distribution, a disproportionally large contribution to X^2 was given by the two events in the 157° bin. Removing these two events, by imposing a $\theta > 160°$ cut, both on the experimental and the Monte Carlo events, reduced the number of experimental events to 44 but at the same time made the variations in all three X^2 - surfaces much smoother. For consistency, the corresponding entries in the position distributions were also removed.

Fig. 5.8 shows contour plots of the three X^2/ν - surfaces in the τ/p_0 - parameter space. Every contour is marked by its X^2/ν - value and the global minima are indicated by black dots.

The shapes of the three X^2 - surfaces shown in Fig. 5.8 are somewhat contradictory when it comes to selecting the best combination of the τ - and p_0 - parameters. Clearly, the X^2_{angle} is practically insensitive to the variations in the lifetime parameter, τ. The minimum on this surface is found for a rather high value of the recoil momentum parameter, $p_0 \approx 450$ MeV/c, as compared to the $p_0 \approx 300$ MeV/c given by the other two X^2 - surfaces. As expected, the X^2_{shad} - values exhibit a strong dependence on the τ - parameter but are only weakly dependent on the choice of p_0, at least for $p_0 > 200$ MeV/c. The global minimum on the X^2_{shad} - surface is found for τ = 0.12 ns and p_0 = 300 MeV/c. As can be seen in Fig. 5.8, this is also the p_0 - value for which the quite irregularly shaped X^2_{shad} - contours have their largest width in the τ -direction.

Therefore, plotting the X^2_{shad} - values as a function of the τ - parameter only, with a fixed recoil momentum function of $N(p) = p \cdot \exp(-p / 300\ [\text{MeV/c}])$, should give quite a conservative estimate of the statistical errors involved. Such a plot is shown in Fig. 5.9 and the dashed lines in this figure indicate how the intersection method is applied to give approximate confidence limits. For the 1σ - error the X^2_{shad} – curve is intersected at a level of $X^2 = X^2_{shad}(\text{min}) + (1^2)$ and for the 95 % confidence level the corresponding level is at $X^2 = X^2_{shad}(\text{min}) + (1.96^2)$. The numerical results are :

$$\tau\,(^{238}\text{U})\ (\text{Sept.-85}) = \left(0.12\ ^{+0.05}_{-0.04} \right) \text{ns} \qquad : 1\sigma \text{ error interval}$$

$$\tau\,(^{238}\text{U})\ (\text{Sept.-85}) = \left(0.12\ ^{+0.13}_{-0.06} \right) \text{ns} \qquad : 95\ \%\ \text{CL interval}$$

In addition to giving parameter estimates, the least-squares method also provides a goodness-of-fit test. The basis for this test is described in Appendix A, section A.3. Making use of eq. A.22 one gets

$$\alpha = 1 - F\left(X^2_{shad}(\text{min}) = 2.4,\ \nu = 3 \right) \approx 48\ \%$$

The probability to get a higher $X^2_{shad}(\text{min})$ in 48 % of the cases, when a new data-set drawn from the same parent population is used, strengthens the confidence in the obtained results.

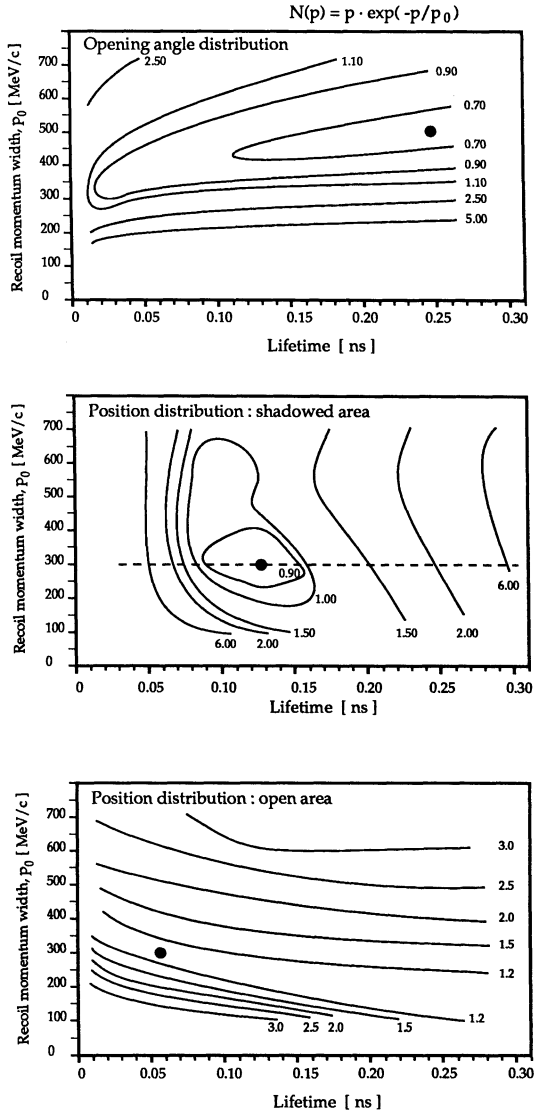

Fig. 5.8 : Contours of reduced residual sum of squares, X^2/ν, in the τ/p_0-parameter space for the September 1985 uranium data. The number of degrees of freedom, ν, is 7 for the opening-angle, 3 for the shadowed-area and 6 for the open-area calculation. Each contour is marked by its X^2/ν – value. The minimum on each surface is indicated by a black dot. The dashed line for p_0 = 300 MeV/c in the shadowed area X^2/ν - surface indicates the cut displayed in Fig. 5.9.

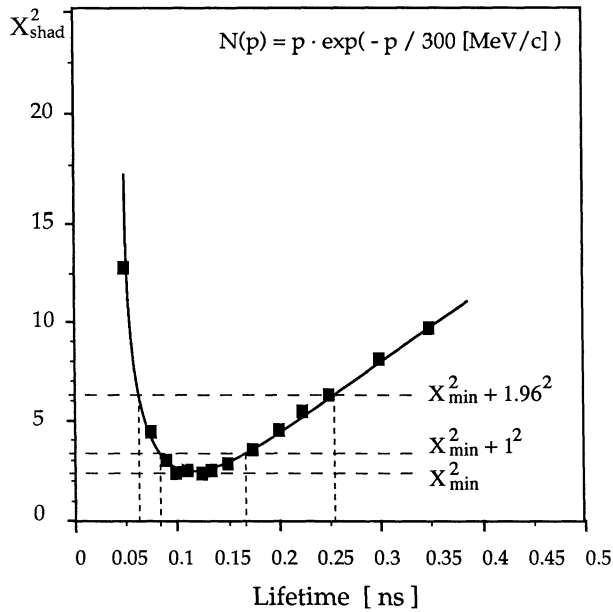

Fig. 5.9 : The residual sum of squares for the shadowed region, X^2_{shad}, as a function of the Monte Carlo lifetime parameter, τ, for September 1985 uranium data. The dashed lines indicate how the intersection method is applied to give the approximate 1σ - and 95 % confidence intervals.

5.2.4.2 *July 1986 uranium data.*

Contour-plots of the three X^2 - surfaces in the τ/p_0 - parameter space are shown in Fig. 5.10 for the July 1986 uranium data. Before applying the least-squares test one experimental event, at position x = -86.7 mm, was excluded from the analysis. This was made on purely computational grounds, to avoid the complication of having bins with no entries in the least-squares expression. The corresponding fragment in the open area position distribution was also removed, as well as the entry in the opening-angle distribution.

In order to reproduce the experimental situation correctly, the Monte Carlo events were required to have a position in the shadowed area of $x_{shad} \geq -71.4$ mm and an opening angle of $\theta \geq 154°$.

As indicated by the black dot in Fig. 5.10, for this data set the global minimum on the X^2_{shad} - surface is found for the combination $\tau = 0.14$ ns, $p_0 = 350$ MeV/c. Both the X^2_{angle} - and the X^2_{shad} - surface exhibit much the same properties as were already found in the analysis of the September 1985 uranium data. However, the larger number of events in the July 1986 run makes the variations over the X^2 - surfaces much smoother in this case.

Following the recipe from the previous analysis one can fix the p_0 - parameter at 350 MeV/c, as given by the X^2_{shad} minimum. This p_0 also more or less corresponds to the largest width of the ellipse-like X^2_{shad} - contours, thus giving a good estimate of the statistical error. The error estimates for the τ - parameter, as given by the intersection method, are shown in Fig. 5.11.

From Fig. 5.11 the following result for delayed fission in the uranium data-set of July 1986 can be extracted:

$$\tau\,(^{238}U)\ (\text{July -86}) = (\,0.140 \pm 0.025\,)\ \text{ns} \qquad : 1\sigma \text{ error interval}$$

$$\tau\,(^{238}U)\ (\text{July-86}) = \left(\,0.140\ ^{+\,0.06}_{-\,0.04}\,\right)\ \text{ns} \qquad : 95\ \%\ \text{CL interval}$$

To obtain these values a recoil momentum function of the form $N(p) = p \cdot \exp(\,-p\ /\ 350\ [\text{MeV/c}]\,)$ was used, as indicated in the figure. Changing to a higher value of the width parameter, setting for example $p_0 = 450$ MeV/c as suggested by the X^2_{angle} - surface, shifts the minimum to 0.15 ns with the same error intervals.

The goodness-of-fit test gives for this data-set

$$\alpha = 1 - F\,(\,X^2_{shad}(\text{min}) = 4.8,\ \nu = 4\,) \approx 31\ \%$$

Even though this value is somewhat lower than what was obtained for the analysis of the September 1985 uranium data it is still comfortably high .

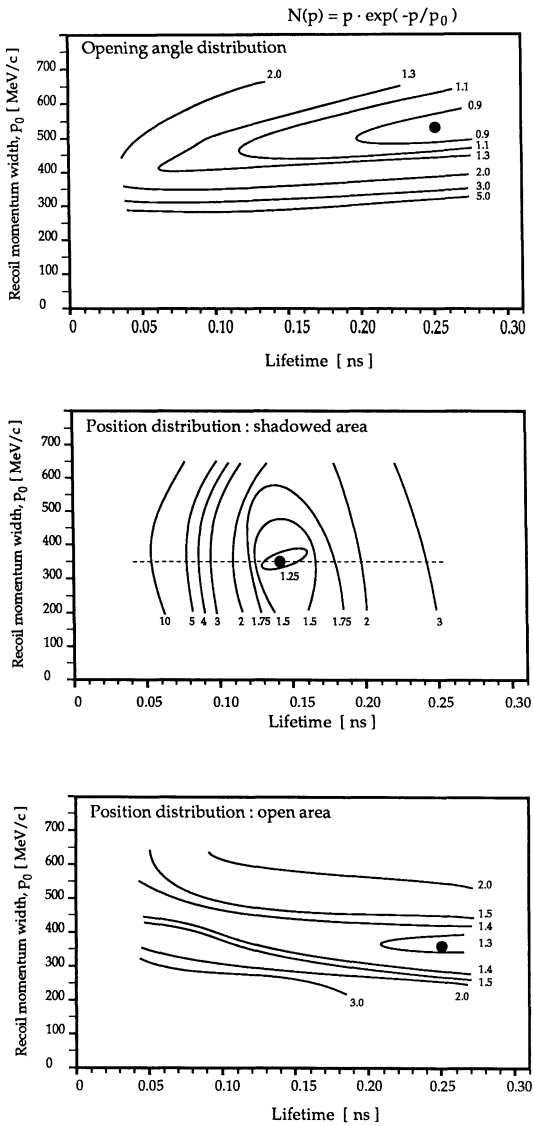

Fig. 5.10 : Contours of reduced residual sum of squares, X^2/ν, in the τ/p_0-parameter space for the July 1986 uranium data. The number of degrees of freedom, ν, is 10 for the opening-angle, 4 for the shadowed-area and 7 for the open-area calculation. Each contour is marked by its X^2/ν – value. The minimum on each surface is indicated by a black dot. The dashed line for p_0 = 350 MeV/c in the shadowed area X^2/ν - surface indicates the cut displayed in Fig. 5.11.

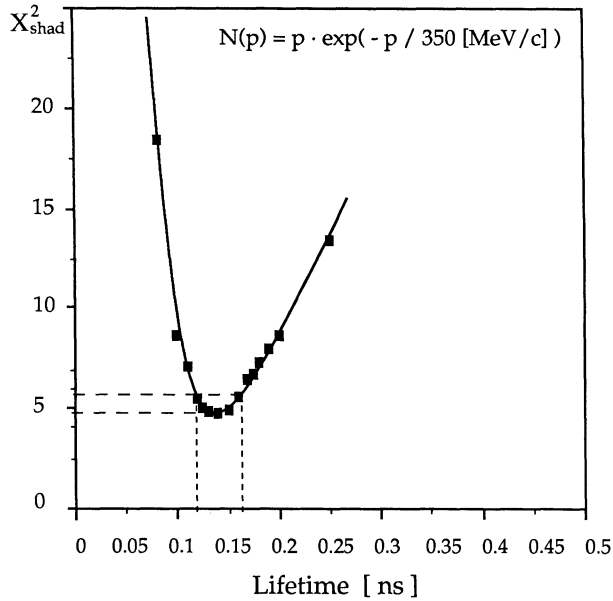

Fig. 5.11 : The residual sum of squares for the shadowed region, X^2_{shad}, as a function of the Monte Carlo lifetime parameter, τ, for the July 1986 uranium data. The solid line only connects the points to guide the eye. The dashed lines indicate how the intersection method is applied to give the 1σ error interval.

5.2.4.3 *All 2.5 mm target backing uranium data.*

As has been seen in the previous two paragraphs, the data from the two uranium target runs, in September 1985 and July 1986, give very consistent results. This consistency, together with the fact that all experimental conditions were the same for the two runs, made it possible to combine them into one data-set. The results from a least-squares parameter search using this combined uranium data sample is presented in Fig. 5.12.

Of the total 209 selected delayed-fission events constituting this combined data-set only one was rejected before the least-squares calculation was performed, namely the one with x_{shad} = -86.7 mm from the July 1986 data.

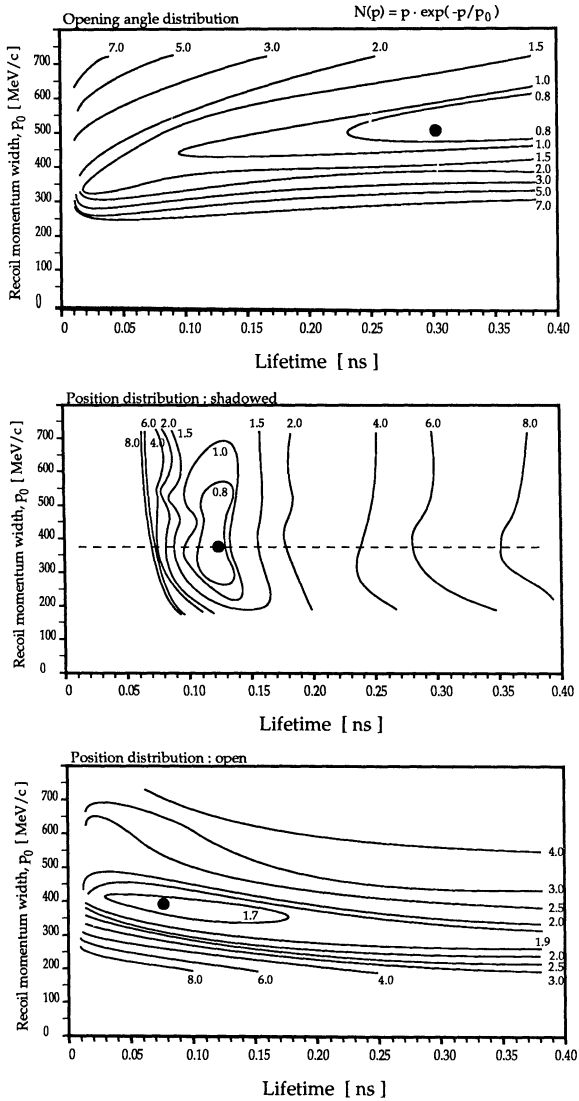

Fig. 5.12 : Contours of reduced residual sum of squares, X^2/ν, in the τ/p_0-parameter space for the combined uranium data. The number of degrees of freedom, ν, is 10 for the opening-angle, 4 for the shadowed-area and 7 for the open-area calculation. Each contour is marked by its X^2/ν – value. The minimum on each surface is indicated by a black dot. The dashed line for p_0 = 375 MeV/c in the shadowed area X^2/ν - surface indicates the cut displayed in Fig. 5.13.

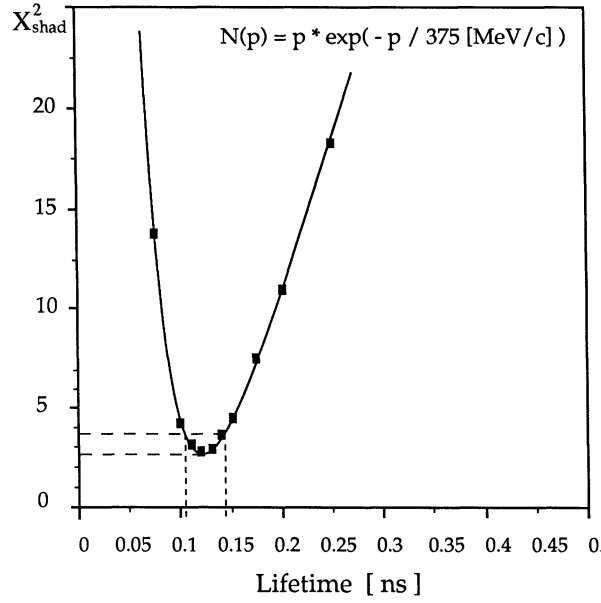

Fig. 5.13 : The residual sum of squares for the shadowed region, X^2_{shad}, as a function of the Monte Carlo lifetime parameter, τ, for the combined 1985 and 1986 uranium data. The solid line only connects the points to guide the eye. The dashed lines indicate how the intersection method is applied to give the 1σ error interval.

Inspecting Fig. 5.12, one observes that the shape of the X^2_{angle} - surface changes very little when combining the two uranium runs. The contours on the X^2_{shad} - surface are narrower and more ellipse-like for the combined data-set. The global minimum on this surface is found for $\tau = 0.12$ ns and $p_0 = 375$ MeV/c; there is also a local minimum for the same lifetime but a p_0 of about 1000 MeV/c. For the X^2_{open} - surface a global minimum has developed for $\tau = 0.07$ ns and $p_0 = 400$ MeV/c. The minimum in this case is very shallow in the τ - direction and there is no real contradiction to the higher and better defined τ - value given by the X^2_{shad} - minimum.

In conclusion, there is a fair overall consistency in the features of the three individual X^2 -surfaces, indicating that the model and the parameter estimates give a good description of the physical processes at hand.

Fig. 5.13 gives the following result for the lifetime parameter, based on delayed fission data from the uranium target runs in September 1985 and July 1986 :

$$\tau\,(^{238}U)\ (\text{All uranium}) = \left(0.120\ ^{+\,0.025}_{-\,0.020} \right) \text{ns} \qquad : 1\sigma \text{ error interval}$$

$$\tau\,(^{238}U)\ (\text{All uranium}) = \left(0.12\ ^{+\,0.05}_{-\,0.03} \right) \text{ns} \qquad : 95\ \%\ \text{CL interval}$$

The recoil momentum function $N(p) = p \cdot \exp(- p/ 375\ [\text{MeV/c}])$ was used to extract these error intervals.

The goodness-of-fit test gives

$$\alpha = 1 - F(X^2_{shad}(\text{min}) = 2.9, \nu = 4) \approx 56\ \%,$$

again indicating that both the model and the parameter estimates describe the experimental situation in a statistically satisfactory manner.

5.2.4.4 July 1986 bismuth data.

Out of the 156 selected delayed fission events from the bismuth run two were discarded before the least-squares parameter search was performed. As in the uranium analysis, this was made to get a smoother behaviour of the X^2 -surfaces. One rejected event had an opening angle of $\theta = 152.1°$ and was excluded by a $\theta > 158°$ cut. The other event had a position in the shadowed region of $x_{shad} = -87$ mm and was excluded by an $x_{shad} > -81.6$ mm cut. The two cuts were imposed both on the experimental and the Monte Carlo data.

The least-squares test of the remaining 154 events is presented in Fig. 5.14. Both the X^2_{angle} - and the X^2_{open} - surface show great similarities with what was found in the uranium analysis : they only exhibit a weak dependence on the lifetime parameter, τ, and the values for the recoil momentum parameter, p_0, at the X^2 -minima are very close to the uranium values.

The shape of the X^2_{shad} - surface, on the other hand, exhibits a few differences compared to that of the corresponding surface found in the uranium analysis, Fig. 5.12. Firstly, the position of the <u>global</u> X^2_{shad} - minimum is in this case found for a high value of the p_0 - parameter, $p_0 \approx 1500$ MeV/c. In the uranium case a <u>local</u> minimum was found for about the same p_0 - value. However, such high p_0 - values are totally excluded by the least-squares fits to the other two distributions. Secondly, the value of the lifetime parameter that gives the X^2_{shad} - minima, both the global one and the local minimum marked by the black dot in Fig. 5.14, is about a factor of two larger than that given by the uranium analysis.

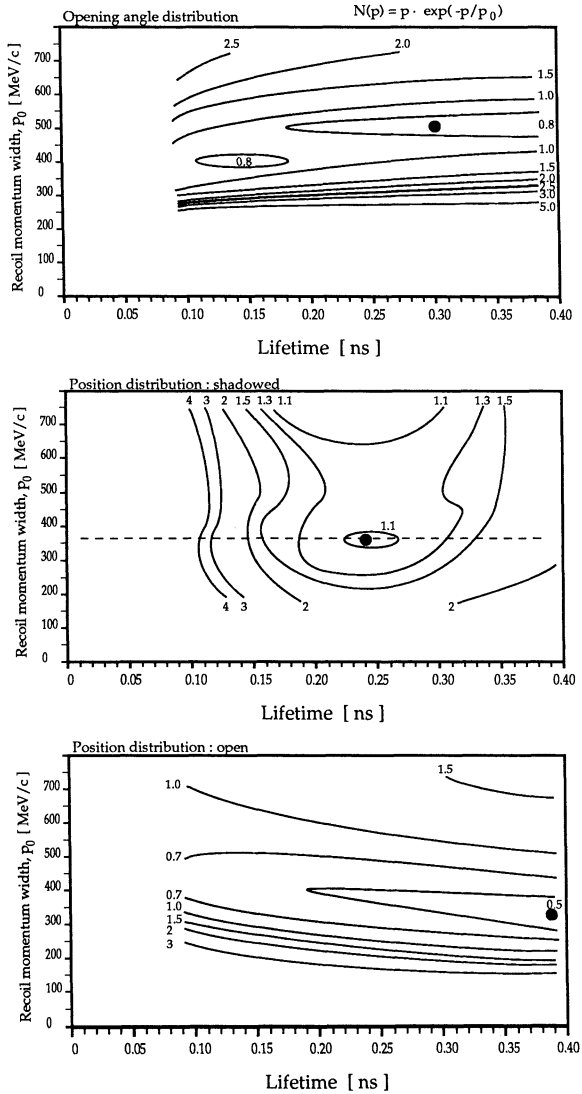

Fig. 5.14 : Contours of reduced residual sum of squares, X^2/ν, in the τ/p_0-parameter space for the bismuth data. The number of degrees of freedom, ν, is 8 for the opening-angle, 5 for the shadowed-area and 7 for the open-area calculation. Each contour is marked by its X^2/ν – value. The minimum on each surface is indicated by a black dot. For the X^2_{shad} the black dot indicates the position of a local minimum. The dashed line for p_0 = 350 MeV/c in the shadowed area X^2/ν - surface indicates the cut displayed in Fig. 5.15.

Fixing the p_0 - value at that given by the local minimum, $p_0 = 350$ MeV/c, indicated by the dashed line in Fig. 5.14, gives the X^2_{shad} as a function of lifetime plotted in Fig. 5.15. The minimum is here found for $\tau = 0.24$ ns, and the statistical errors given by the intersection method, indicated by the dashed lines in Fig. 5.15, are :

$$\tau\,(^{209}\mathrm{Bi}) = \left(0.24 \,^{+0.06}_{-0.05} \right) \text{ns} \quad : 1\sigma \text{ error interval}$$

$$\tau\,(^{209}\mathrm{Bi}) = \left(0.24 \,^{+0.13}_{-0.08} \right) \text{ns} \quad : 95\ \%\ \text{CL interval}$$

The shape of the recoil momentum function was in this case N(p) = p * exp(- p/ 350 [MeV/c]).

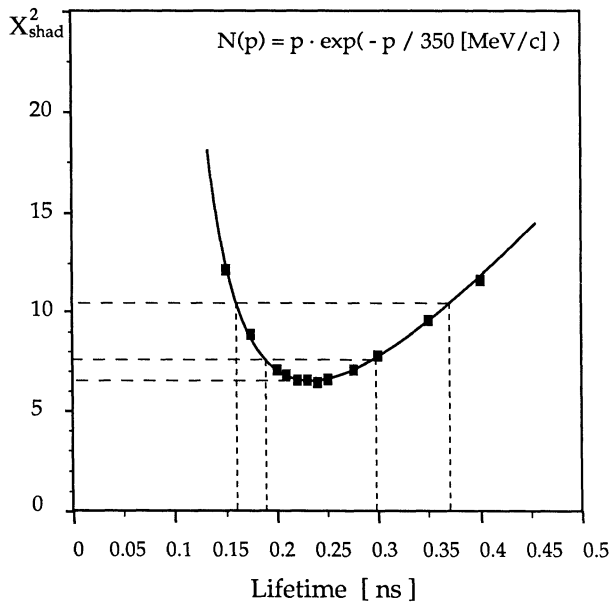

Fig. 5.15 : The residual sum of squares for the shadowed region, X^2_{shad}, as a function of the Monte Carlo lifetime parameter, τ, for the bismuth data. The solid line only connects the points to guide the eye. The dashed lines indicate how the intersection method is applied to give the 1σ and 95 % CL error intervals.

The goodness-of-fit test gives

$$\alpha = 1 - F(X^2_{shad}(\min) = 6.5, \nu = 5) \approx 27\ \%.$$

A probability of 27 % for getting a higher $X^2_{shad}(\min)$ when using a new set of data drawn from the same parent distribution should normally be quite acceptable. In this case, however, the fact that only a local minimum of the X^2_{shad} - surface has been used adds some extra uncertainty to the results.

In view of the different results obtained in the uranium and the bismuth analysis, the shape of the X^2_{shad} - surface and the rather low goodness-of-fit value in the bismuth case might indicate that some of the assumptions made in the simulation program are not quite applicable to the bismuth analysis.

5.2.5 The stability of the results.

Several tests were performed to study the stability of the results presented earlier in this chapter. At the same time, these tests also give an indication of the systematical errors involved in the analysis. The results of some of these tests are collected in this sub-section; they are grouped rather loosely in four categories:

- 10 mm target backing test,
- software geometrical tests,
- tests of the analysis method,
- variation of some Monte Carlo input parameters.

5.2.5.1 10 mm target backing test.

About one third of the antiprotons in the September 1985 run was used in a test where the normal 2.5 mm wide scintillator target backing was replaced by a 10 mm wide backing. The target consisted of a $2 \times 5\ mm^2$ large, $100\ \mu g/cm^2$ thick uranium spot deposited in the centre of the scintillator backing.

As can be seen from Table 5.1, the total number of fission events from the wide backing run was consistent with what was obtained with a target of the same size in the 2.5 mm backing run, taking the different number of incoming antiprotons into account. The number of fission events per 10^6

antiprotons were 16.6 and 14.7 for the wide and the narrow backing runs, respectively.

When all the cuts had been made, seven delayed fission events remained in the wide target run. Of these, two had their positions in the shadowed area within 0.5 mm of the selected separation line between the open and the shadowed regions. These seven events correspond to 7.3 delayed fission events per 10^9 antiprotons, to be compared to a yield of 21.9 per 10^9 antiprotons in the 2.5 mm backing run. Hence, the experimental ratio of yields was $R_{10/2.5} = 0.33 \pm 0.10$. The detection efficiency ratio, given by the Monte Carlo program for the same geometries, was $R_{MC} = 0.24$, i.e., the same within the experimental error.

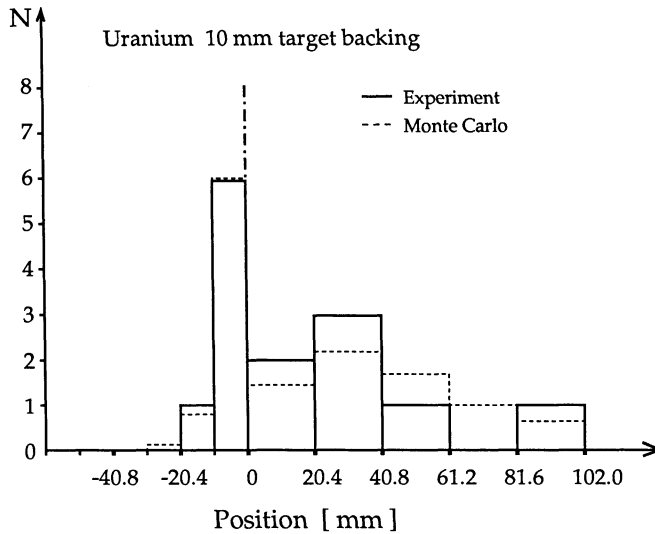

*Fig. 5.16 : Position distribution of the seven experimental delayed fission events (full drawn line) from the uranium 10 mm target backing run in September 1985. The Monte Carlo histogram (dashed line) was produced with a lifetime parameter of 0.12 ns and a recoil momentum given by N(p) = p * exp(-p/375 [MeV/c]). Note that the bin size in the open region is 20.4 mm.*

The Monte Carlo simulation gives an expected position distribution of the seven delayed fission events as shown in Fig. 5.16. Note that the bin size in the open region has been increased to 20.4 mm in this figure. These results were obtained with a lifetime parameter of 0.12 ns and a momentum distribution of the form $N(p) = p \cdot \exp(-p/375\ [MeV/c])$, as given by the

analysis presented in sub-section 5.2.4. There is a fair agreement between the experimental and the Monte Carlo distributions, especially in the shadowed region. The simulated opening-angle distribution is also consistent with the experimental data.

In conclusion, the wide target backing test clearly shows that the recoil-distance method works properly in the application presented in this thesis.

5.2.5.2 *Software geometrical tests.*

a) As mentioned before, in sub-section 5.2.2, a slight **rotation of the target** of about 0.3° around the vertical axis could be observed in the bismuth run of July 1986. Including such an effect in the simulation runs for the bismuth analysis had no effect on the final results of the analysis.

b) Two of the simplifying assumptions about the **beam spot geometry**, made in the simulation program, were tested.

I) The position of the beam spot was shifted from the centre of the target to other parts of the target surface. This led to higher X^2 - levels in the least-squares analysis, without changing the parameter estimates.

II) The uniform 2×2 mm^2 beam spot distribution was replaced by a Gaussian distribution with a standard deviation σ = 0.64 mm (FWHM = 1.5 mm) both horizontally and vertically, positioned at the centre of the target. Re-running the least-squares analysis with the combined uranium data-set, a shift of the best lifetime estimate of +0.02 ns, to 0.14 ns, was obtained, with no significant change in the p_0-parameter estimate. It should be noted that the 1.5 mm (FWHM) beam spot is smaller than what was usually observed experimentally. In reality, the beam was more uniformly distributed over the target surface and consequently a 0.02 ns uncertainty due to this effect is a quite conservative estimate.

c) In spite of the careful selection of the separation line between the shadowed and the open regions, described in sub-section 5.2.2, there is still a chance for some **background events** to be included in the final event sample. The sources of these background events could be:

i) Prompt events that, due to the finite position resolution of the chambers, are registered as striking the shadowed part of the chambers.

ii) An up-down asymmetry in the position distributions which, if not corrected for, will smear out the separation line.

iii) The possibility of having hypernuclei of fission fragments, i.e., a Λ particle attached to a prompt fission fragment. If the trajectory of such a

hyper-fragment is almost parallel to the target plane there is a possibility that the subsequent decay of the Λ might give a recoil to the residual fragment in such a way that the flight-path is deviated into the shadowed region.

All these effects have in common that they add an admixture of background events to the position distribution in the region closest to the separation line. Consequently, a cut rejecting the events in this region should eliminate this type of background.

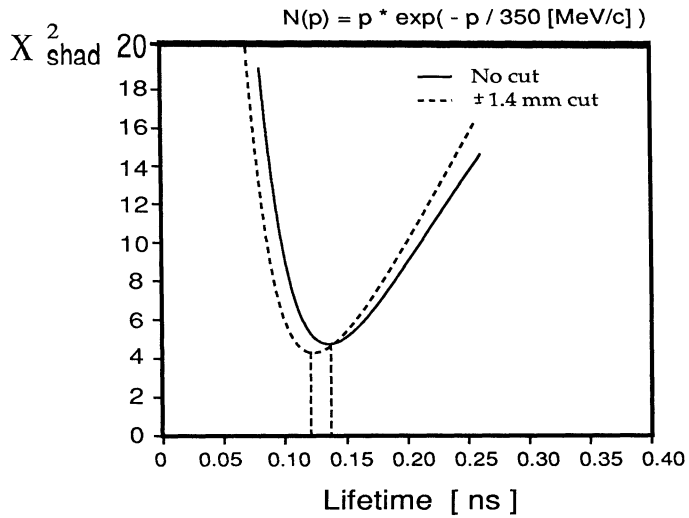

Fig. 5.17 : The residual sum of squares for the shadowed region, X^2_{shad}, as a function of the Monte Carlo lifetime parameter, τ, and for a fixed p_0 = 350 [MeV/c]. The solid line is for the full July 1986 uranium target data sample and the dashed line for a case where events from a region of ±1.4 mm around the separation line between the open and the shadowed regions have been excluded from the analysis.

Events from three successively larger areas around the separation line were in this way excluded from the analysis of the uranium target data of July 1986: ± 1.4 mm, ± 5.1 mm and ± 10.2 mm. The result for the X^2_{shad} - surface, for a fixed p_0 = 350 [MeV/c], is plotted in Fig. 5.17. For clarity, only the curves connecting the points for the no-cut and the smallest cut cases are shown. All the three curves with the cut give a lifetime estimate of about 0.12 ns, 0.02 ns shorter than for the full event sample. Moreover, the data-set with the smallest cut, ± 1.4 mm, even gives a lower minimum value and slightly narrower error limits than the full sample, in spite of the smaller

number of events. This improvement is also seen for the X^2_{angle} - and the X^2_{angle} - surfaces for this particular data-set. For the broader cuts the error intervals get increasingly larger, as a consequence of the reduced number of events.

It is not possible to identify whether the observed shift is a real background effect or a purely statistical fluctuation. Therefore, it was considered as part of the systematic uncertainty.

5.2.5.3 *Tests of the analysis method.*

a) One way to test the intrinsic resolution of the analysis method chosen is to apply the least-squares test to **Monte Carlo produced event samples.** In the literature, this procedure has also been suggested as a way to get an indication of the distributional properties of the parameter estimates when a non-linear model is used (Pre 86). However, in the test performed here only three Monte Carlo event samples were analyzed, for which reason nothing can be concluded on these distributional properties.

Data set	Lifetime estimate [ns]	1σ error [MeV/c]	95% CL	p_0	X^2/ν
MC 1	0.25	± 0.05	$^{+0.15}_{-0.08}$	350	4.1/5
MC 2	0.22	± 0.05	$^{+0.14}_{-0.08}$	300	5.5/5
MC 3	0.28	± 0.06	$^{+0.17}_{-0.09}$	400	7.4/5
Exp. Bi	0.24	$^{+0.06}_{-0.05}$	$^{+0.13}_{-0.08}$	350	6.5/5

*Table 5.4 : Results from parameter search tests on three Monte Carlo generated event samples. The Monte Carlo samples were all produced with fission parameters according to the bismuth case, a lifetime of 0.225 ns and a momentum distribution of the form N(p) = p * exp(-p/450 [MeV/c]). The results from the parameter search on the experimental bismuth target data from July 1986 are shown for comparison.*

The tests were made on data-sets simulating the bismuth target conditions. A remarkable result of the analysis was the great similarities

between the structure of the different X^2 - surfaces for the Monte Carlo data and the real experimental data. In particular, the X^2_{shad} - surfaces from the analysis of the Monte Carlo data samples also exhibit a number of local minima, close to the known, correct lifetime but for values of the p_0-parameter which were both larger and smaller than the one used to produce the data. For each Monte Carlo sample, however, only one of these minima was consistent with the p_0 -value given by the shapes of the X^2_{angle} - and the X^2_{open} - surfaces. The intersection method then gives, for the selected p_0 - value, the results presented in Table 5.4. The input for the simulation was $\tau = 0.225$ ns, and the form of the momentum distribution was $N(p) = p \cdot \exp(-p / 450\,[\mathrm{MeV/c}])$.

From this study one can conclude that the finite number of experimental events in combination with the geometry of the set-up seem to limit the sensitivity of the analysis roughly to the level presented here. The peculiar shape of the X^2_{shad} - surfaces, with several local minima where only one is consistent with the shapes of the X^2_{open} - and X^2_{angles} - surfaces, is reproduced in least-squares tests on Monte Carlo generated data.

b) The least-squares method is not the only method by which one can estimate certain parameters from a set of experimental data. Another method is the so called **maximum likelihood method** (Ead 71). Assuming that the number of entries in each bin are drawn from a Poisson distribution, the maximum likelihood method gives the best parameter estimate as that which maximizes the function :

$$ML = \prod_{i=1}^{N} \left[\frac{1}{y_i!} (f_i)^{y_i} \exp(-f_i) \right] \qquad (5.3)$$

or, equivalently, maximizes the logarithm of ML :

$$\ln ML = \sum_{i=1}^{N} \left[y_i \ln(f_i) - f_i \right] \qquad (5.4)$$

where the constant term $-\ln(y_i!)$ has been dropped from the sum.

Here, N is the number of histogram bins,
y_i is the experimental number of entries in bin i and
f_i is the "theoretical" number of entries in bin i, given by the Monte Carlo calculation.

The function 5.4 was used in one part of the analysis of the combined uranium data sample. The directions of the recoiling, heavy hypernuclei

were in this case restricted to a cone in the forward direction in the Monte Carlo simulation. The analysis of the prompt fission events, described in the next section, indicates that, due to the large energy losses experienced by the fragments when passing through the target, such a model would be realistic.

Rejecting all recoils making an angle of less than 15° to the target surface resulted in a ln(ML) surface in the τ/p_0- parameter space with a maximum at $\tau = 0.12$ ns, $p_0 = 400$ MeV/c. Fig. 5.18 shows a plot of ln (ML) - ln $(ML)_{max}$ as a function of the lifetime parameter for a fixed $p_0 = 400$ MeV/c. The statistical errors can be extracted from this plot by intersecting the ln(ML) curve at levels of 0.5 and 1.96 below the maximum for the 1σ error and 95 % CL, respectively.

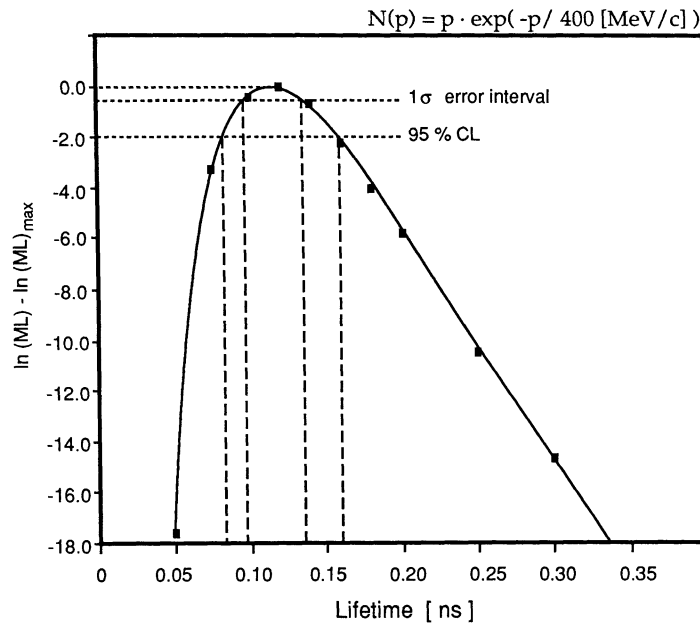

Fig. 5.18 : Log likelihood curve for the shadowed region as a function of the Monte Carlo lifetime parameter, τ, and for a fixed $p_0 = 400$ [MeV/c]. The recoils were required to make an angle of at least 15° to the target plane. The dashed lines indicate how the approximate 1σ and 95% confidence limits are determined. The combined uranium data sample from 1985 and 1986 was used.

The result thus obtained is:

$\tau\,(^{238}U)$ (Max.likelihood) $= \left(0.120\ ^{+0.020}_{-0.025} \right)$ ns : 1σ error interval

$\tau\,(^{238}U)$ (Max.likelihood) $= (\,0.12 \pm 0.04\,)$ ns : 95 % CL interval,

These results are in good agreement with what was obtained with the least-squares method, presented in sub-section 5.2.4. At the same time, this shows that, at the present state of accuracy, the final results are not sensitive to such a restriction in the directions of the outgoing recoils.

5.2.5.4 Variations of Monte Carlo input parameters.

a) The **mass of the fissioning, heavy hypernucleus** was varied over several tens of amu. In general, a weak rise in the minimum X^2_{shad} - value was observed for lower masses, but no significant change in the parameter estimates occurred.

b) To explain the shape of the Δx-distribution, discussed in sub-section 5.2.3, an **extra momentum** was added to the recoiling hypernucleus at the instant of decay. It was found that a fixed additional momentum of 300 - 400 MeV/c was needed to fit the Δx-distributions, Fig. 5.7, but that this had only a marginal effect on the levels of the X^2 -surfaces and no effect on the final parameter estimate.

c) A few other choices for **the power, i, in the recoil momentum distribution,** eq. 5.1, were tested in connection with the bismuth 1986 data. It turned out that the choices i=1, 2 and 3 all gave the same estimate for the lifetime parameter. For the momentum distribution it was observed that the higher the choice for i, the lower the estimate for p_0 turned out, as expected. This question is studied further in the analysis of the prompt fission data, where it is concluded that it is not possible to select one best i/p_0-combination. Rather, for every i there exists a p_0 that gives a reasonable fit to the data. This statement seems to hold also for the analysis of the delayed fission data, where, however, the choice i=2 gives a slightly better fit to the data.

d) All heavy hypernuclei, making a **recoil angle** of less than 6° and 15° to the target plane, were rejected in two separate tests on the combined uranium 2.5 mm target backing data. No indication of any significant change in the parameter estimates was observed, as has already been presented for

the 15° case in the previous paragraph. One should be aware, however, that to a certain extent this effect is taken care of by the phenomenological recoil momentum distribution.

5.2.6 Delayed fission yield.

The yield of delayed fission events per antiproton can be calculated with the following formula:

$$P_{del.fiss} = \frac{N_{del.fiss}}{N_{\bar{p}} \cdot \varepsilon_{stop} \cdot \varepsilon_{det} \cdot \varepsilon_{escape}} \qquad (5.5)$$

where $N_{del.fiss.}$ is the number of delayed fission events,
$N_{\bar{p}}$ is the number of antiprotons on the target,
ε_{stop} is the target antiproton stopping efficiency,
ε_{det} is the geometrical detection efficiency
and ε_{escape} is the heavy recoil escape efficiency.

Collecting the information from Tables 3.1, 5.1 and 5.3 and from Fig. 5.2 gives the necessary input for evaluating eq. 5.5, except for the recoil escape efficiency. This latter quantity was in sub-section 5.2.1 estimated to be about 0.6 for both targets used here. Due to the fact that the range of low-energy, heavy ions in heavy materials is very poorly known, the error in ε_{escape} is large, here put to 25%. The relative errors in ε_{stop} and ε_{det} are estimated to be 10%, respectively.

Run (backing)	$N_{\bar{p}}$ [$*10^9$]	N_{del} [%]	ε_{stop} [%]	ε_{det} [$*10^{-4}$]	$P_{del.fiss.}$ [$*10^{-4}$]	$\Delta P_{del.fiss.}$ [$*10^{-4}$]
U85(10 mm)	0.96	7	1.1	0.14	7.9	± 3.7
U85(2.5 mm)	2.10	46	1.1	0.58	5.7	± 1.8
U86(2.5 mm)	5.62	163	1.1	0.58	7.6	± 2.3
Bi86(2.5 mm)	11.75	156	1.2	0.85	2.2	± 0.7

Table 5.5 : Calculation of the delayed fission yield per stopped antiproton. The ε_{escape} was in all cases put to 60%, since the ε_{det} contains the assumption about a uniform, 4π, distribution of the recoils.

The results of this calculation for the different runs and targets are presented in Table 5.5. The ε_{det} was taken from the simulation program with a lifetime of 0.12 ns for uranium and 0.225 ns for bismuth. In both cases a p_0 of 375 MeV/c was used. Note that the lower probability for producing delayed fission events in the September 1985 run is consistent with the already observed lower total fission yield in this run, explained by a larger size of the beam spot in this period.

5.3 Prompt fission analysis.

The PS177 experiment was primarily designed to measure the lifetimes of heavy hypernuclei by means of the recoil-distance technique. In addition, the data contain a large sample of antiproton induced prompt fission events. The analysis of these data is described in this section. Two new results were extracted : i) the final momentum distribution of the residual nuclei produced in the annihilation and ii) the probability for antiproton induced prompt fission.

5.3.1 Acceptance.

Prompt fission events can only be recorded in the open area of the PPAC detectors. The solid angle covered by this region with respect to the centre of the target is easily evaluated using the Monte Carlo simulation program. It is found to be 5.1 % for the two chambers together, and the solid angle for 5.1 mm bins along the beam axis, x, is shown in Fig. 5.19a.

Comparing the solid angle dependence, Fig. 5.19a, with the experimental position distribution for single fission fragments, Fig. 5.19b, it is clear that a large fraction of the fragments are never recorded in the detectors. To study this effect in more detail, one can define an overall detection efficiency as

$$\varepsilon_{det}^{i} = \frac{N_{exp}^{i}}{N_{\Omega}^{i}} \qquad (5.6),$$

where N_{exp}^{i} is the experimentally registered number of single fission fragments for bin i,

N_{Ω}^{i} is the solid angle for bin i.

This detection efficiency, normalized to 100 % at the bin x = 53.55 mm, is shown in Fig 5.20. Three regions of different efficiency behaviour have been indicated in the figure :

Region I, from the target plane projection to 25 mm, where there is a sharp rise in efficiency from 0 % up to almost 100 %.

Region II, from 25 to 75 mm, where the efficiency is approximately flat.

Region III, from 75 mm to the chamber edge, with a slowly decreasing detection efficiency.

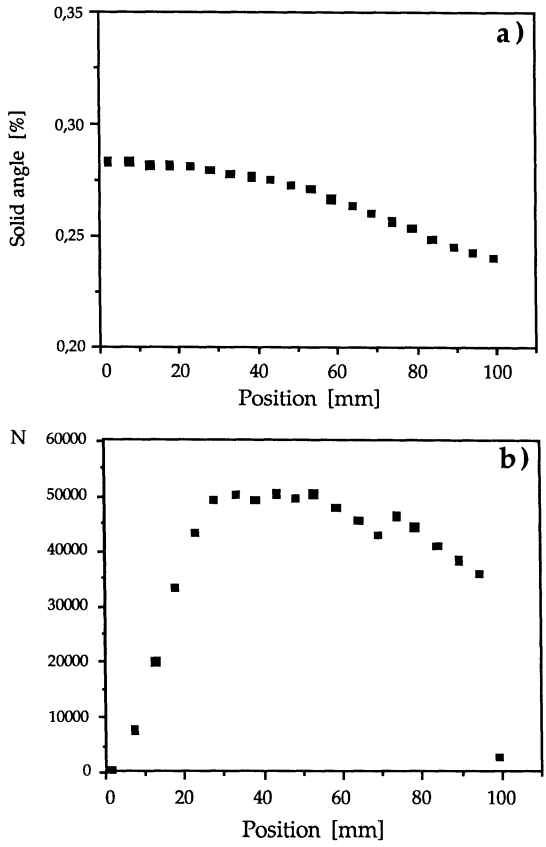

Fig. 5.19: a) The solid angle of the PPAC detectors with respect to the centre of the target, as calculated with the simulation program for 5.1 mm bins. Note that the vertical scale starts at 0.2 %. b) Experimental position distribution of single fission fragments for 5.1 mm bins. Both chambers summed.

The loss of fragments in region I can be understood in terms of multiple scattering of the fission fragments when passing through the target. As was shown in section 4.1, fission fragments are in general energetic enough to

pass through the whole depth of the target, even when travelling almost parallel to the target plane. Fragments lost due to insufficient range could explain a poor efficiency up to at most a few mm from the target plane projection, x = 0. Multiple scattering, on the other hand, can be expected to be most harmful to those fragments moving parallel to the target plane, directing some of these fragments towards the target backing where they will be lost. The size of this effect can be estimated by using the formula 5.7 (Agu 86).

$$\Theta_0 = \frac{14.1\,[\mathrm{MeV/c}]}{p_{inc}\,\beta_{inc}}\, z_{inc}\,\sqrt{\frac{L}{L_R}}\left(1+\frac{1}{9}\log_{10}\left(\frac{L}{L_R}\right)\right) \qquad (5.7)$$

where inc denotes the moving particle,
p is the momentum,
β is the velocity,
z is the charge (in units of e),
L is the path length traversed and
L_R is the radiation length of the medium, 6 g/cm^2 for U.

This Θ_0, given in radians, is the projected standard deviation of a Gaussian distribution of deflection angles. It is accurate to within 5 % for $10^{-3} < L/L_R < 10$.

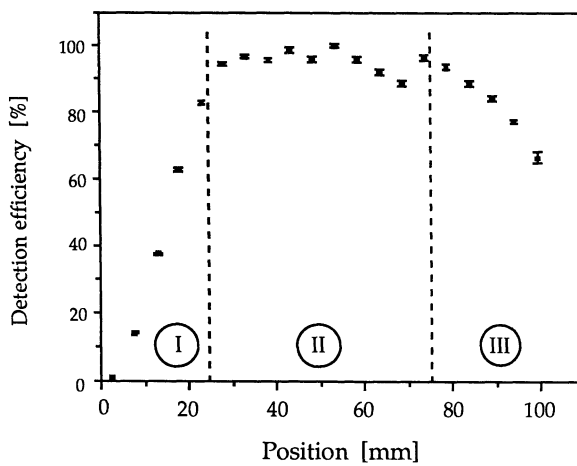

Fig. 5.20: The detection efficiency is the combined effect of target escape efficiency and the counting efficiency in the parallel plate chamber. Values normalized to 100 % at 53.55 mm. Three regions, with different efficiency behaviour, are indicated in the figure.

A typical fission fragment, moving inside the target, in a direction only a few tenths of a degree with respect to the target plane, might have to traverse several mg/cm^2 of the target material before escaping. Eq. 5.7 then gives a Θ_0 of a few degrees, enough to direct some fragments towards the target backing, where they are lost. For those fragments which reach the detectors, the same effect will tend to smear out the position distribution close to the target plane projection.

One explanation of the decreasing detection efficiency in region III could be the greater inclination of these tracks with respect to the detector planes. The maximum angle of a fragment trajectory with respect to the normal of the detector plane is 33°. The path length in the various detector foils for such a fragment is 20 % longer than for perpendicular tracks. Hence, these fragments lose a larger fraction of their energy in these foils, and will thus have a lower energy when passing through the gas-volumes. A lower kinetic energy gives a smaller amount of energy deposited in the gas-volume, as shown in Fig. 4.2. Due to the larger inclination the signal will also be spread over more wires, and the combined effect of a low energy deposited over a longer track could in some cases give an induced charge below the discriminator threshold.

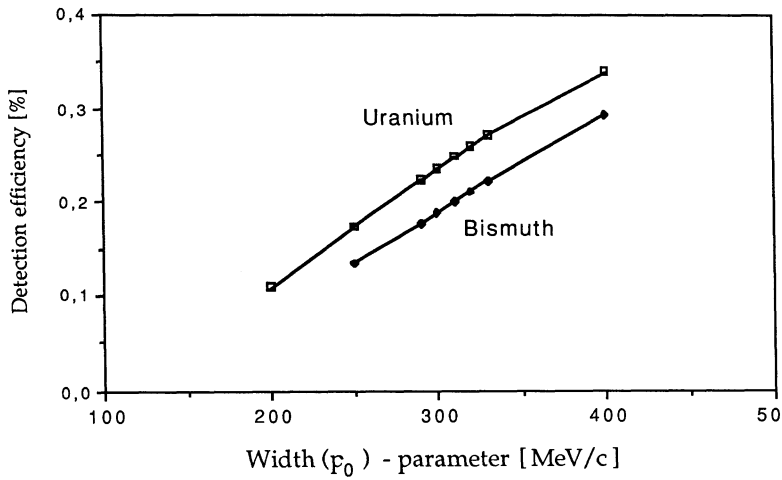

Figure 5.21 : Total detection efficiency for coincidences for different widths, p_0, of the momentum transfer function $N(p) = p^{3/2} \cdot \exp(-p / p_0)$, as given by the simulation program. The singles detection efficiency described in sub-section 5.4.1 has been used. All other fission process parameters are given in Table 5.2.

In the analysis of the prompt fission events it was sometimes useful to reproduce the efficiency behaviour of the chambers. Instead of introducing complicated and time-consuming relations for multiple scattering and energy straggling of heavy ions moving in heavy materials - relations that are quite uncertain in the low energy region - a simpler method was adopted: The probability for detection of each fragment was estimated from its impact position in the chambers.

The three regions identified in Fig. 5.20 were represented in the following way in the simulation program : Region I by a third-order polynomial, Region II by a constant efficiency of 100 % and Region III by a linearly decreasing efficiency function. The total effect of introducing these efficiencies into the Monte Carlo was that 82 % of the prompt, single fission fragments emitted towards the PPACs will actually be detected. For coincident events the detection efficiency depends on the assumptions about the momentum transfer. Fig. 5.21 shows this efficiency, as calculated with the simulation program, for one special case, where the momentum transfer function $N(p) = p^{3/2} \cdot \exp(-p/p_0)$ has been used.

5.3.2 Experimental distributions.

In this sub-section the main experimental distributions are collected as they emerge after all cuts described in sub-section 5.1.1 have been applied. Only data from the two runs in July 1986 are presented.

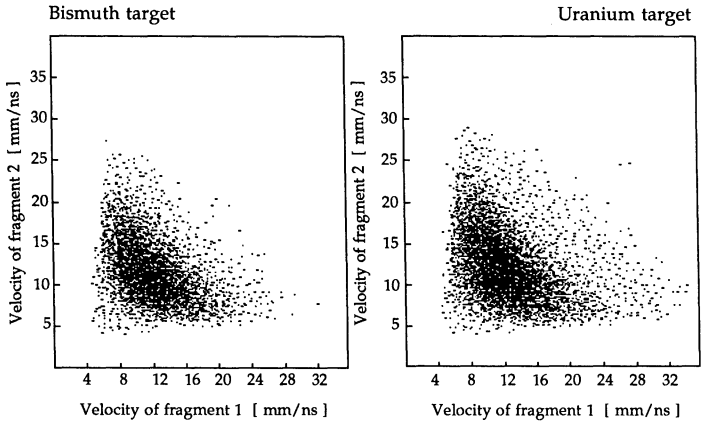

Fig 5.22 : Scatter plot of the correlation between velocities of coincident fission fragments for antiproton induced fission in bismuth and uranium.

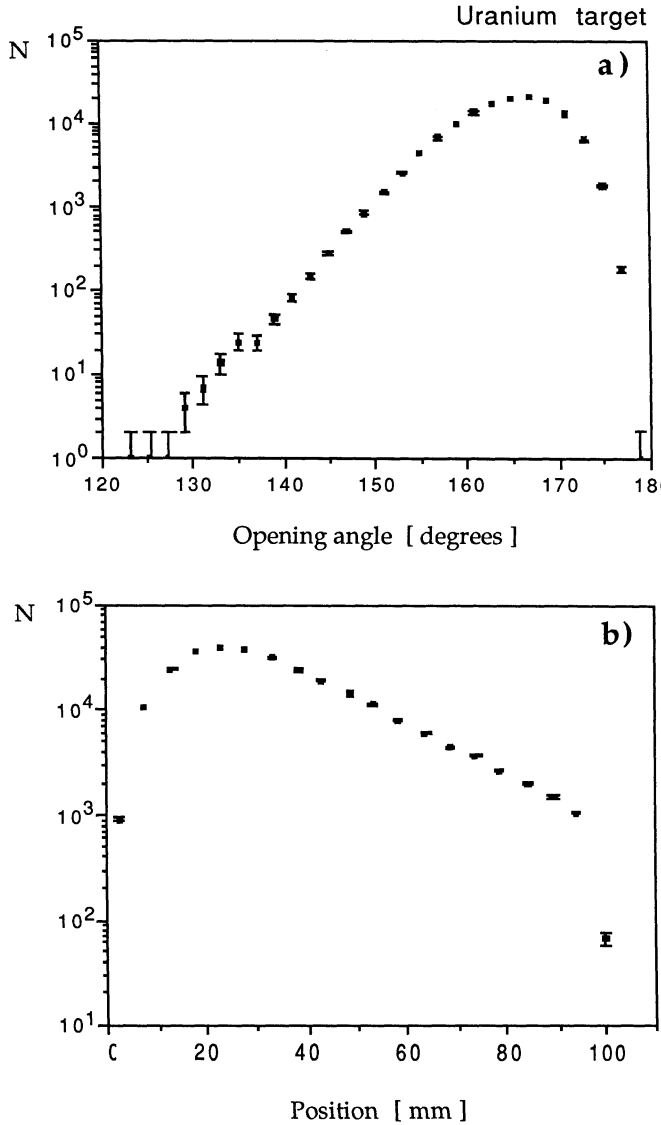

Fig. 5.23 : Experimental distributions for antiproton induced prompt fission events in uranium. Each distribution contains 138 500 events. The statistical errors are indicated. a) shows opening angles binned by 2°. The mean angle is 164.5 ° and the rms deviation is 5.5 °. b) shows the position distribution in the open area in 5.1 mm bins.

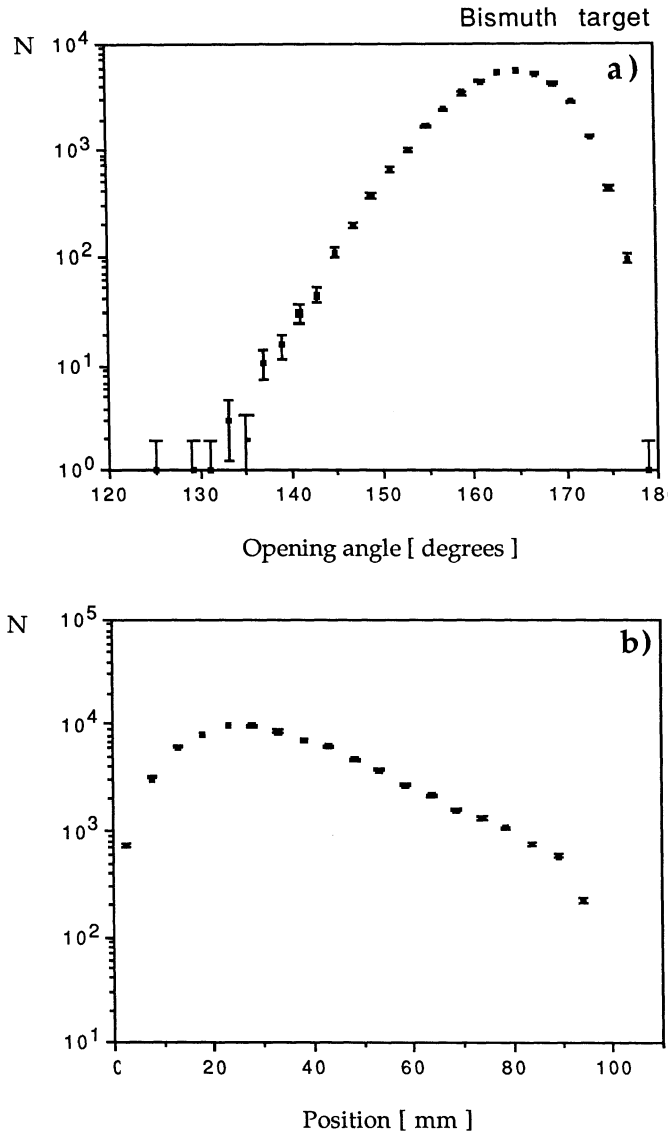

Fig. 5.24 : Experimental distributions for antiproton induced prompt fission events in bismuth. Each plot contains 39 400 events. The statistical errors are indicated. a) shows the opening angles binned by 2°. The mean opening angle is 163.4 ° and the rms deviation is 5.8 °. b) shows the position distribution in the open area in 5.1 mm bins.

One straightforward physics result is immediately obtained by correlating the velocity of one fragment with that of the other, as shown in Fig. 5.22. It is clear from this figure that the symmetric fission mode predominates, even though the distributions exhibit large wings of asymmetric fission. This observation lends support to the assumption of symmetric fission made in the simulation program, sub-section 5.1.2.

The experimental distributions for opening angle and position in the open area for antiproton induced prompt fission events in the uranium target are shown in Fig. 5.23. The corresponding distributions for the bismuth target are shown in Fig. 5.24. Note the logarithmic scales. The uranium data sample contains 138 500 events and the bismuth sample 39 400 events, as shown in Table 5.1.

5.3.3 Momentum transfer.

In the antiproton annihilation process linear momentum, as well as excitation energy, is transferred to the residual nucleus. The subsequent emission of nucleons in the early stages of the de-excitation can be expected to be more or less isotropic. The initial momentum transfer will therefore essentially be conserved and result in an opening angle between the two fission fragments that deviates from 180°. This angle, Θ in Fig. 5.25, can thus be regarded as an analyzer of the momentum transfer to the residual nucleus in antiproton annihilations. Additionally, in the analysis presented here the position distribution of the prompt fission events in the open area of the detectors has been used as a consistency check.

The same method as has been described in the analysis of delayed fission events could be applied to the prompt fission data, using the simulation program adapted to prompt fission as the "theoretical" prediction. Since the delayed and the prompt fission events are sub-sets of the same large data sample the geometrical conditions determined in the delayed event analysis also hold for the prompt fission events. In this analysis only the momentum transfer width, p_0 in eq. 5.1, was treated as a free parameter.

Two different approaches were used in the least-squares tests of the prompt fission data. The first made use of the full data sample, and consequently had to rely on the weighting of each simulation event according to the detection efficiency function described in sub-section 5.3.1. The second method tried to circumvent the problem of detection efficiency

altogether, by rejecting all events where the impact positions were in the Region I area of the detectors, shaded in Fig. 5.25.

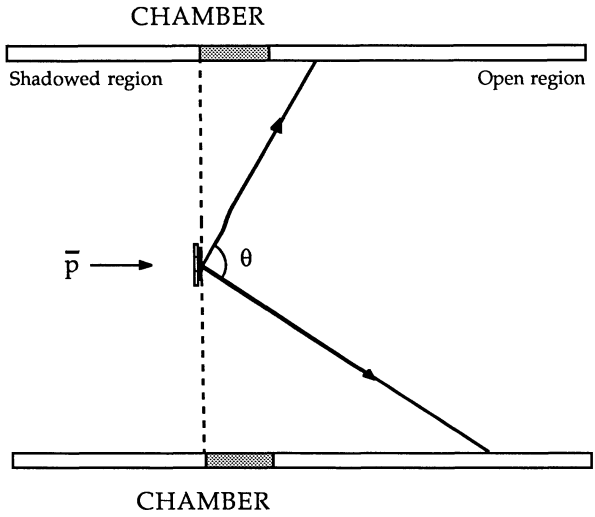

Fig. 5.25 : Schematic top view of the experimental set-up with the main components of a typical prompt fission event indicated. The drawing is not to scale.

The first approach has the benefit of a large event sample and many degrees of freedom in the least-squares formula (Appendix A, eq. A.1) but suffers from the uncertainty in treating the energy loss and angular straggling in the target correctly. The second method avoids the problems caused by the target to a large extent but to the expense of fewer events and a smaller number of degrees of freedom. One also has to be aware that the small-angle events selected by the second method, events with $\Theta \lesssim 164°$, correspond to the high momentum transfer part of the spectrum, thereby limiting the sensitivity of the analysis.

A limiting factor in the prompt fission event analysis was the speed of the computer used. The low detection efficiency for coincidence events in combination with the large sample of experimental prompt fission events made it practically impossible to generate enough simulation events to perform a full scale least-squares test. In the parameter search presented here the simulation histograms contain 50 - 100 % of the number of events found experimentally. The method still selects the best parameter values but no reliable goodness-of-fit and parameter error estimates can be obtained.

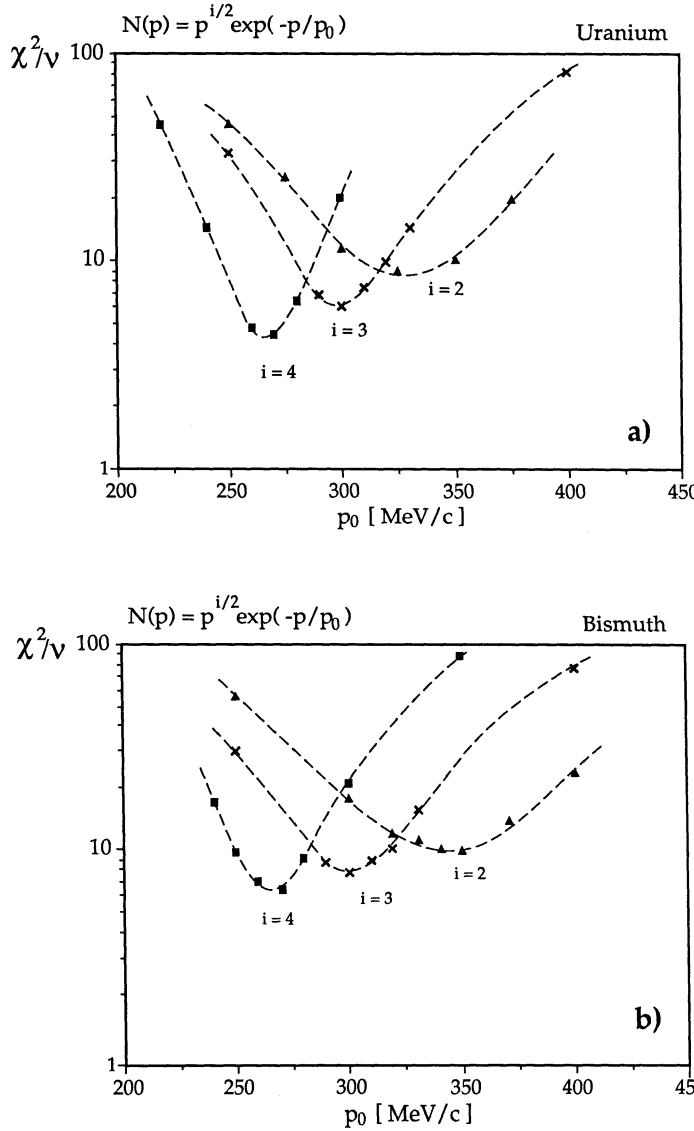

Fig. 5.26 : Reduced chi-square as a function of the momentum transfer width, p_0. The least-squares test was performed according to the method I where the full, weighted Monte Carlo opening-angle distributions were compared to the experimental ones, Figs 5.23a and 5.24a. A momentum transfer function given by eq. 5.1, with i = 2, 3 and 4, has been used as indicated in the figure.

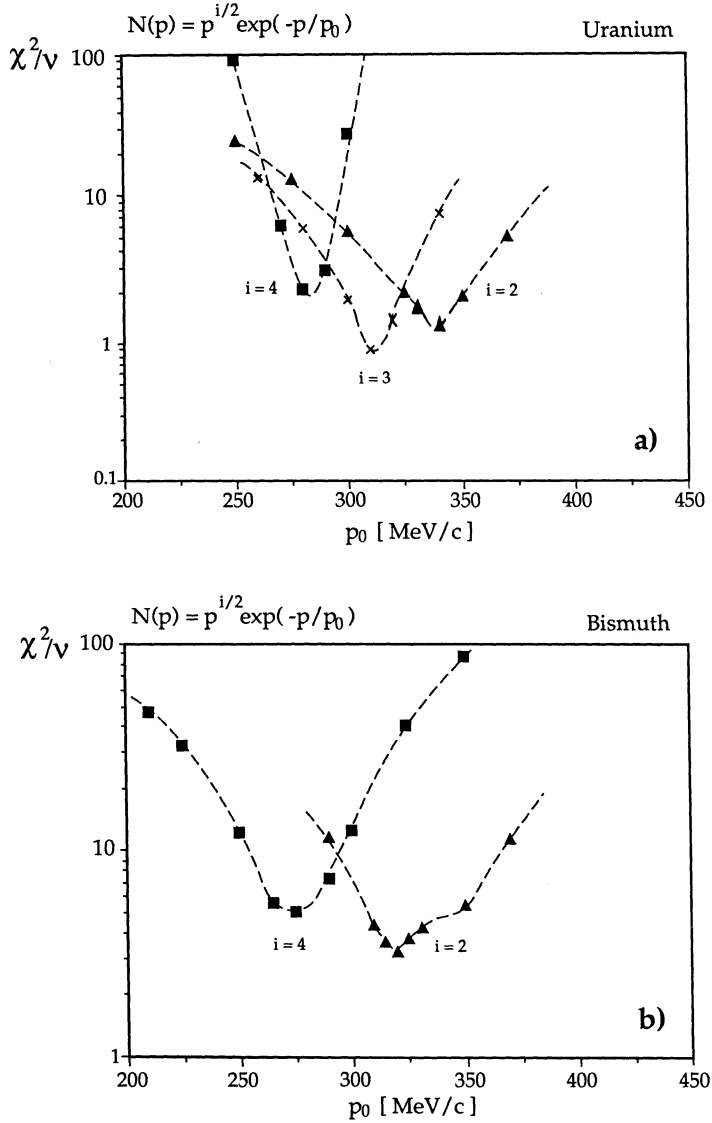

Fig. 5.27 : Reduced chi-square as a function of the momentum transfer width, p_0. The least-squares test was performed on the 140°-164° part of the opening-angle distributions, Figs 5.23a and 5.24a, according to the method II discussed in the text. A momentum transfer function given by eq. 5.1, with i = 2, 3 and 4, was used, as indicated in the figure.

The least-squares tests for the best parameter according to the two methods are presented in Figs 5.26 and 5.27. In these figures the reduced chi-square for the opening-angle distribution as a function of the width, p_0, of the momentum transfer function is plotted. Three different shapes of the momentum transfer function are shown, corresponding to the choices i = 2, 3 and 4 in eq. 5.1. The dashed lines only connect the points to guide the eye.

Full weighted opening-angle distribution (method I) :

	i	p_0 [MeV/c]	"Δp_0" [MeV/c]	X^2/ν (min)
Uranium				
	2	330	± 45	158/18
	3	300	± 25	121/22
	4	265	± 20	82/19
Bismuth				
	2	350	± 50	258/25
	3	300	± 30	194/24
	4	265	± 20	154/24

140° - 164° part of opening-angle distribution (method II) :

	i	p_0 [MeV/c]	"Δp_0" [MeV/c]	X^2/ν (min)
Uranium				
	2	340	$\pm^{10}_{15}$	13/10
	3	310	± 12	9.1/10
	4	285	± 9	19/10
Bismuth				
	2	320	$\pm^{40}_{20}$	31/10
	3	-	-	
	4	275	± 20	50/10

Table 5.6 : Numerical results from the least-squares search for the best width-parameter, p_0, in the momentum transfer function of the form given in eq. 5.1. The width, "Δp_0", is given by the intersection of the chi-square curve at a level of twice the minimum value.

The relatively low statistics of the simulation runs compared to the experimental number of events made it hard to determine the error, σ_i in eq. A.1, in the least-squares formula. For this reason, the curves in Figs 5.26 and 5.27 in some cases have rather high minimum values. This fact is also displayed in the X^2/ν(min)-column of Table 5.6. Nevertheless, the sharpness of the minima clearly gives a best choice for the p_0 - parameter for each choice of i. The "Δp_0" column of Table 5.6 gives the width of the X^2-curves at a level of twice the minimum. This quantity is only displayed to give a rough indication of the widths of the individual X^2 - curves; it is not a strictly statistical error.

For both methods, the corresponding curves for the position distribution in the open area give the same results as those for the opening-angle distribution, shown in the figures. This consistency increases the confidence in the final results. The level of the reduced chi-square, however, is slightly higher when using the position distribution.

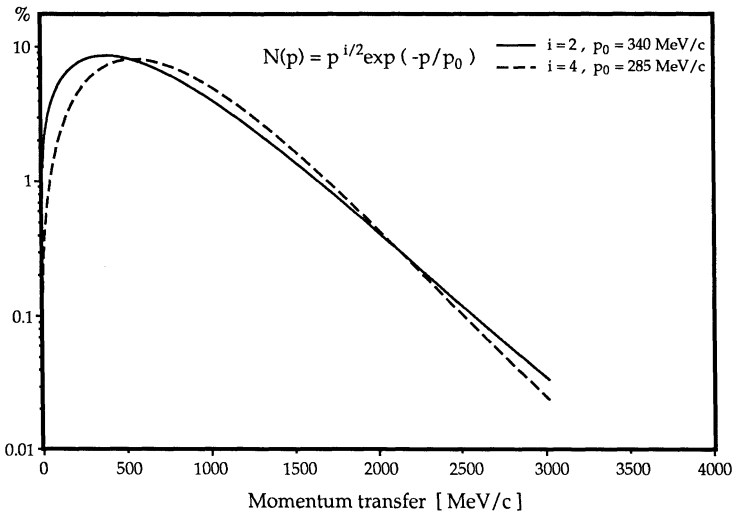

Fig. 5.28 : The momentum transfer function of eq. 5.1 with two specific choices for the i, p_0 - values, as given by the analysis of the uranium prompt fission data. The curves are normalized to an integral of 100%.

The numerical results are collected in Table 5.6. The two methods give quite consistent results and the difference between the uranium and the bismuth results is also small. As expected, the analysis of the 140° - 164° part gives slightly higher p_0 - values but in view of the large uncertainties

involved the differences between the two methods are not considered to be significant.

It should be pointed out that, at this level of the analysis, there is no contradiction between the different i,p_0 - combinations presented in Table 5.6. They all have very similar shapes, as is exemplified in Fig. 5.28, where the momentum transfer distributions with the best-choice p_0 as given by the uranium 140° - 164° analysis are presented. For clarity only the curves corresponding to the i-choices 2 and 4 are shown in this figure. The curve for i = 3 falls in between these two.

Hence, it is not possible to select one best i,p_0 - combination; rather, the method gives a best p_0 for each i. The combination i = 3, p_0 = 310 MeV/c, giving a lower minimum than the others in Fig. 5.27a, is used in the next sub-section to calculate the fission probabilities and later to compare this result with some intra-nuclear cascade calculations.

5.3.4 Fission probabilities.

Collecting information from different parts of this thesis now makes it possible to deduce the probability for fission induced by stopped antiprotons, given by the expression

$$P_{fiss} = \frac{N_{fiss} - N_{chance}}{N_{\bar{p}} \cdot \varepsilon_{stop} \cdot \varepsilon_{det}} \qquad (5.8)$$

where
- N_{fiss} is the number of prompt fission coincidences,
- N_{chance} is the estimated number of chance coincidences,
- $N_{\bar{p}}$ is the number of antiprotons striking the target,
- ε_{stop} is the efficiency for stopping antiprotons in the target,
- ε_{det} is the total detection efficiency in the chambers.

All the values needed to evaluate eq. 5.8 have already been given : N_{fiss} and $N_{\bar{p}}$ are found in Table 5.1, N_{chance} was discussed in section 4.4, ε_{stop} is given in Table 3.1 and ε_{det} is shown in Fig. 5.21. The total detection efficiency for coincident fission fragments, ε_{det}, is calculated by means of the simulation program and depends slightly on the assumptions therein. In particular, the effect of different choices for the momentum transfer width parameter, p_0, is shown in Fig. 5.21 for the two targets. The functional form used for the momentum transfer to the residual nucleus in this figure

corresponds to the best choice given by the analysis described in the previous sub-section.

Using ε_{stop} values for an antiproton momentum of 105 MeV/c the resulting antiproton induced fission probabilities are :

$$P_{fiss}^{U} = \frac{138\,500 - 200}{5.62 \cdot 10^{9} \cdot 2.00 \cdot 10^{-3} \cdot 1.07 \cdot 10^{-2}} = \frac{138\,300}{120\,300} = 1.15 \pm 0.17$$

$$P_{fiss}^{Bi} = \frac{39\,400 - 150}{11.75 \cdot 10^{9} \cdot 2.50 \cdot 10^{-3} \cdot 1.16 \cdot 10^{-2}} = \frac{39\,250}{339\,700} = 0.116 \pm 0.017$$

The 15 % relative error in the fission probabilities is based on an estimated relative error of 10 % in both ε_{stop} and ε_{det}. The statistical errors in N_{coinc} and $N_{\bar{p}}$ are negligible in comparison.

The ratio of the two fission probabilities is thus found to be

$$R_{U/Bi} = \frac{P_{fiss}^{U}}{P_{fiss}^{Bi}} = 10 \pm 2$$

which agrees well with what was found in the earlier 45° target test, briefly described in sub-section 3.3.2.

Chapter 6 : SUMMARY AND CONCLUSIONS

In the PS177 experiment, low-energy antiprotons were brought to rest in thin targets of ^{209}Bi and ^{238}U. A detector system, designed according to the principles of the recoil-distance technique, recorded the positions of single and coincident heavy fragments emitted in the annihilation reactions. By a careful selection procedure, clean samples of fission events were extracted. Using the least-squares method made it possible to extract physics information about both delayed and prompt, antiproton induced fission.

The results obtained in this thesis are summarized and compared with previously obtained experimental and theoretical results. Prompt fission is discussed first. Even though these results are more or less a by-product of the main, delayed-fission experiment, they can nevertheless contribute to our understanding of antiproton-nucleus interactions.

6.1 Prompt fission summary and conclusions.

6.1.1 Summary

Two main results were extracted from the analysis of the prompt fission data. Firstly, the least-squares method was used to make an estimate of the parameters pertaining to the recoil-momentum distribution of the residual nuclei, following antiproton annihilation. Secondly, the numbers of registered fission events for the two targets, ^{209}Bi and ^{238}U, were used to deduce the fission probabilities in antiproton annihilation.

Target	# events	Recoil momentum distribution: i	p_0 [MeV/c]	Fission probability (per stopped $\bar{p}$)
^{209}Bi	39 400	2	$320 \pm ^{40}_{20}$	0.116 ± 0.017
^{238}U	138 500	3	310 ± 12	1.15 ± 0.17

Table 6.1 : Summary of the results for antiproton-induced prompt fission. The form of the recoil-momentum distribution function is $N(p) = p^{i/2} \cdot exp(-p / p_0)$. *See Table 5.6 for the complete set of momentum distribution parameter values and comments on the error determination.*

The final numerical results are collected in Table 6.1. The detailed analysis is described in section 5.3.

The velocity correlation scatter plot (Fig. 5.22) should also be considered as an experimental result, since it can be compared, at least qualitatively, with previous experimental data from high-energy proton induced fission.

6.1.2 Discussion and conclusions.

It was already pointed out in section 5.3 that the results for the recoil momenta of residual nuclei in the two targets are consistent with each other, within the quoted errors. Furthermore, in spite of the apparent difference in the parameters describing the momentum distribution, the actual curves are quite similar in shape, as shown in Fig. 5.28. Therefore, the best uranium result can be taken as the recoil momentum distribution for both targets :

$$N(p) = p^{3/2} \cdot \exp(- p/ \{ 310 \pm 12 \, [\mathrm{MeV/c}] \}) \qquad (6.1).$$

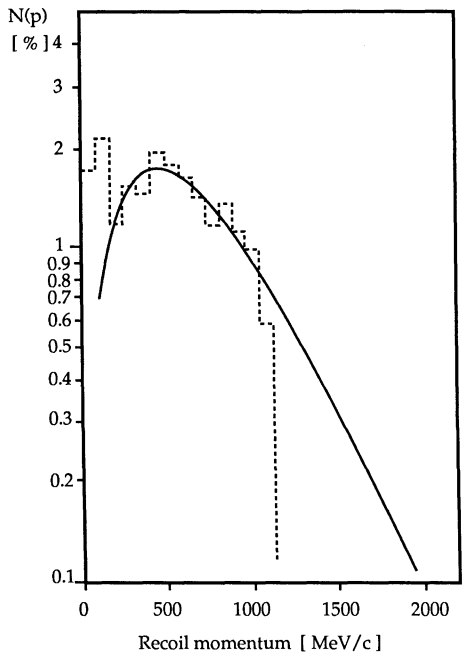

Fig. 6.1 : Comparison between the recoil momentum distribution for antiproton annihilation in heavy targets obtained in the present experiment (solid line) and in an intranuclear-cascade calculation (dashed histogram), performed by Iljinov et al. (Ilj 82).

In Fig. 6.1 the recoil-momentum distribution of eq. 6.1 is compared with the result of an intranuclear-cascade (INC) calculation, performed by Iljinov et al. (Ilj 82) for antiprotons stopped in ^{208}Pb. In their paper, Iljinov et al. only present the recoil momentum distribution up to 1120 MeV/c, resulting in the sharp cut-off in the INC calculation histogram. Note also that the first 6 bins of 40 MeV/c in the histogram have been recombined into 3 bins of 80 MeV/c in Fig. 6.1. The function of eq. 6.1 is normalized to the histogram in the interval 240 - 1120 MeV/c. It should be added that Cugnon et al. in a recent paper (Cug 88) have obtained results that are highly consistent with those of Iljinov et al.

Clearly, the agreement between the INC calculation and our result is quite good for recoil momenta higher than about 300 MeV/c. For small recoil momenta, however, the discrepancy is large. The reasons for this are twofold. Firstly, the INC result takes into account all recoiling nuclei, not only those which undergo fission. Then, the difference for slow recoils might be due to the fact that these do not acquire enough excitation energy for fission to occur. This conclusion is further corroborated by correlation studies, also made by Iljinov et al. These concern the dependence of excitation energy and recoil momentum on the number of pions interacting with the residual nucleus. Secondly, the sharp decrease in the experimental detection efficiency for fragments moving parallel to the target plane, shown in Fig. 5.19, limits the sensitivity of the present analysis in the slow-recoil region. To give an indication of the size of the effect, the 50% efficiency level, reached about 15 mm from the target plane projection (Fig. 5.19b), corresponds roughly to a recoil momentum of 350 MeV/c.

In conclusion, the difference between eq. 6.1 and the INC calculation for slow recoils is readily understood. The good agreement between experiment and calculation for recoil momenta larger than about 300 MeV/c shows that the intranuclear-cascade approach is well suited to give the gross features of low-energy antiproton annihilation on complex nuclei.

The present results on the fission probability in antiproton annihilation can be compared both to previously reported, relative fission yields from stopped-antiproton interactions (Ber 85) and to measurements using high-energy protons and other projectiles (And 87, Bec 83 and Bat 76). Qualitatively, it is also interesting to note that no trace of nuclides close to the mass of A=238 was found in a radio-chemical analysis of the residual nuclei after antiproton annihilation in uranium (Egi 88). Only radio-nuclides corresponding to fission fragments were found, and it was

concluded that fission is dominant in stopped antiproton annihilation on uranium.

A number of different results on fission probabilities, including the present study, are shown in Fig. 6.2. The central value of 115% fission probability in uranium, obtained in this thesis, is clearly unphysical even though the lower error bound includes 100%. An underestimate of the antiproton stop rate would give rise to such an effect and, considering the large uncertainties involved, cannot be ruled out.

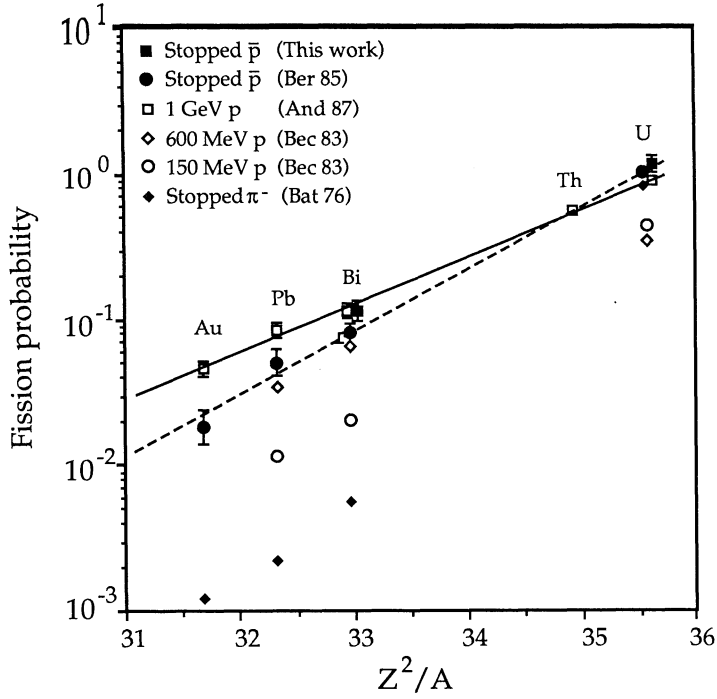

Fig. 6.2 : Deduced fission probabilities from a number of different experiments. Note the logarithmic scale. For the measurements with energetic protons the probability is given by the ratio of the fission cross-section to the total geometrical reaction cross-section. The values for 150 and 600 MeV protons are extracted from Fig. 2.18 and those for stopped π^- from the figure in the original paper (Bat 76). The two straight lines are exponential fits to the 1 GeV proton data (solid line) and the stopped antiproton data of Ber 85 (dashed line).

An earlier measurement of antiproton induced prompt fission, made by the PS177 group, was already presented in Fig. 3.6. Both measurements with stopped antiprotons make use of the nuclides ^{209}Bi and ^{238}U. The results

show a fair agreement, although one has to bear in mind that the fission probabilities in the work shown in Fig. 3.6 are normalized to a presumed 100% fission probability in ^{238}U, while those obtained here are absolute values. The ratio between the fission probabilities in bismuth and uranium is in both studies about 0.1. Comparing the antiproton induced fission probability with what is obtained with high-energy protons gives an indication of the excitation energy involved. The stopped antiproton data clearly exhibit close similarities with the 0.6 and 1 GeV proton data, and one can use the latter as a qualitative guide. In the analysis of the data from proton-nucleus interactions at 1 GeV it was concluded that an excitation energy of 200-350 MeV (And 87) was transferred to the residual nucleus. Cugnon and co-workers use their INC model to deduce a somewhat higher excitation energy, about 400 MeV, for both 1 GeV proton (Cug 87a) and stopped antiproton (Cug 87b) interactions with heavy nuclei. Our finding, that the excitation energy of the residual nucleus after antiproton annihilations is of the same order as that from 1 GeV protons, lends qualitative support to the results of their calculation.

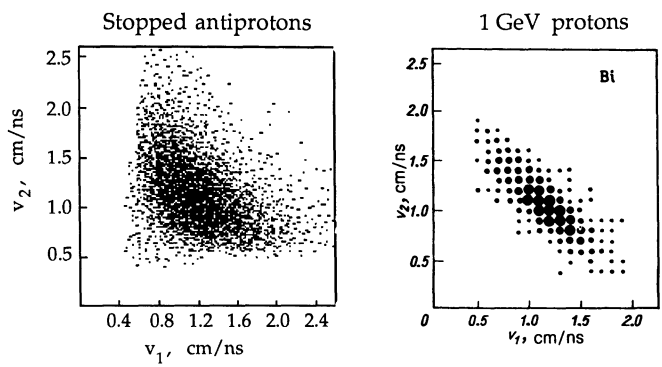

Fig. 6.3 : Comparison of the velocity correlations of coincident fragments from fission induced in ^{209}Bi. The left figure shows the result for stopped antiprotons (this work) and the right figure is obtained with 1 GeV protons (And 87).

This conclusion is further strengthened by studying the velocity correlations of coincident fission fragments in stopped antiproton and 1 GeV proton (And 87) induced reactions. The antiproton and proton results give very similar, symmetric distributions (Fig. 6.3). It is pointed out by

Andranenko et al. that the velocity distributions should reflect the structure of the more fundamental fragment-mass distributions very closely. Thus, the concentration of velocity ratios in the symmetric region is quantitative evidence for a symmetric distribution of fission fragment masses. The slightly broader distribution, obtained in the present study, can be explained by a wider range of masses for the fissioning residual nuclei in antiproton annihilations.

To summarize, our results on prompt fission of heavy nuclei, induced by stopped antiprotons, are in good agreement with what is obtained from modern intranuclear-cascade calculations for these reactions.

Following antiproton annihilation at rest on ^{209}Bi and ^{238}U, the distribution of recoil momenta of the residual nuclei is described by the function :

$$N(p) = p^{3/2} \cdot \exp(- p/ \{ 310 \pm 12 \, [MeV/c] \}) \qquad (6.1).$$

Fission probabilities and mass distributions, obtained in stopped antiproton annihilation on heavy nuclei, follow closely what is observed in fission reactions induced by high-energy protons. This points to an excitation energy of around 400 MeV for the residual nuclei in both of these processes.

6.2 Delayed fission summary and conclusions.

6.2.1 Summary

The main effort in the analysis of the antiproton-induced, delayed-fission events was devoted to a determination of the lifetime of the process. The least-squares method for parameter estimation was used, where the model predictions, with which the experimental distributions had to be compared, were supplied by a Monte Carlo simulation program. The model is based on the assumption that the observed fission activity originates from the decay of heavy nuclei, slowly recoiling out of the target. The only free parameters in the estimation procedure were those pertaining to the lifetime and the momentum of the recoiling nuclei. It might seem surprising that the momentum-distribution parameters deduced in the prompt-fission analysis are not used here. However, there is no a priori reason to believe that the processes leading to delayed and prompt fission are similar in this respect. In

all other respects, the Monte Carlo model reflected well-known physical processes.

As an additional piece of information, the numbers of events for each target give the probability for producing delayed fission in stopped-antiproton annihilation on heavy nuclei.

The results from the analysis of the delayed fission events are collected in Table 6.2.

Target	# events	Lifetime [ns]	p_0 [MeV/c]	X^2/ν (shadowed)	Y [$\cdot 10^{-4}$]
^{209}Bi	156	$0.24\ ^{+0.06}_{-0.05} \pm 0.02$	350	6.5/5	2.2 ± 0.7
^{238}U	209	$0.120\ ^{+0.025}_{-0.020} \pm 0.020$	375	2.9/4	6.6 ± 1.3 *

Table 6.2 : Summary of the results for delayed fission, induced by stopped antiprotons. See the text for details about the error in the lifetime determination. The parameter p_0 determines the width of the recoil momentum distribution of the residual nuclei, given by the function $N(p) = p \cdot exp(-p / p_0)$. Column five, X^2/ν, gives the residual sum of squares and the number of degrees of freedom for the shadowed region fit. Column six, Y, contains the yields of delayed fission events per stopped antiproton.

* *This entry is calculated using all uranium data, i.e., including also the 10 mm target backing run. For all the other uranium results, only the two 2.5 mm runs were used.*

There are two contributions to the errors quoted for the lifetimes in Table 6.2. The first is the statistical uncertainty, as given by the intersection method described in Appendix A. The second contribution is an estimate of the systematical error based on the findings in sub-section 5.2.5. There it was shown that in particular two effects seem to influence the parameter estimate: the assumption about the beam spot distribution over the target surface and the exclusion of events from a region close to the target plane projection. Tests on both effects shifted the parameter estimate by approximately 0.02 ns, although in opposite directions. For this reason, ±0.02 ns is taken as a guide for the systematical error in the lifetime determination.

For uranium, the result for the delayed fission yield, Y in Table 6.2, is a weighted average of the values obtained in all three runs, i.e., including the 10 mm backing data.

6.2.2 Interpretation of the delayed-fission activity.

In practice, there are only two presently known physical processes which could give rise to a delayed-fission activity with a lifetime in the 0.1 ns region. One possibility is that fission isomers are observed. The physics of these objects is briefly discussed in sub-section 2.3.2. The other candidate is the formation and decay of hypernuclei, the basic physics of which is given in section 2.2.

The hypothesis of fission-isomer production has several drawbacks.

Firstly, a delayed-fission activity is in the present experiment observed both when using a uranium and a bismuth target. Until now, no fission isomers have been observed in the mass region around bismuth; neither are they theoretically predicted.

Secondly, the only fission isomer which could conceivably be produced in this experiment is that of ^{235}U. This isomeric state has a lifetime of 167 ns (Fig. 2.21) which is more than a thousand times longer than the lifetime extracted from the present analysis of the uranium target data. Moreover, from Fig. 2.21 it is also clear that no presently known fission isomer has a lifetime that would fit those reported here.

Thirdly, the production rates of fission isomers are, even under the most favourable conditions, a few orders-of-magnitude below the yields presented in Table 6.2. Additionally, the velocity correlation plot for delayed-fission events in the present experiment points to a symmetric split of the fissioning nucleus, indicating a rather high excitation energy. Fission isomers, on the other hand, give rise to asymmetric mass distributions, typical of low-energy fission.

Based on these arguments, it does not seem likely that fission isomers are responsible for the observations made here. A much more plausible explanation is given by the production and decay of hypernuclei. Precisely those arguments which were used against fission isomers can now be turned in favour of hypernuclei.

Firstly, similar yields of delayed-fission events for bismuth and uranium are expected in this case. There is no reason to believe that the probability of forming hypernuclei should be very different for these two nuclei ; only their inclination to decay through the fission channel will differ.

Secondly, the lifetimes observed here, 0.12 ns and 0.24 ns for the uranium and the bismuth targets, respectively, are very close to the free Λ lifetime,

being 0.263 ns, and also to the lifetimes of previously studied light hypernuclei, found to be in the range 0.09 - 0.28 ns (see Fig. 2.10).

Thirdly, as was discussed in sub-section 2.2.2, Λ-particles are quite frequently produced in low-energy antiproton annihilation. The order-of-magnitude estimate for hypernuclear formation in stopped-antiproton annihilation, presented in eq. 2.10, agrees surprisingly well with the yields presented in Table 6.2. Furthermore, the indication of a symmetric mode of fission for the delayed activity fits into the scheme of hypernuclei. The large energy released, about 160 MeV, in the non-mesonic decay of the Λ is taken up by two nucleons deeply embedded in the nucleus. These decay nucleons may transfer some of their energy to the residual, heavy nucleus, leaving it in a highly excited state, the fission decay of which gives a symmetric mass distribution.

Finally, theoretical calculations for the decay of heavy hypernuclei predict lifetime values in the range 0.3 - 2 times that of the free Λ-particle (Fig. 2.16). Our results fit nicely into this interval. The theoretical implications of the results presented here are further discussed below.

In conclusion, it seems safe to assume that the delayed-fission activity observed in the present experiment has its origin in the decay of heavy hypernuclei.

6.2.3 Discussion and conclusions.

Accepting the hypothesis that the formation and decay of heavy hypernuclei are responsible for the delayed-fission activity, the results of Table 6.2 can be discussed in more detail.

The uranium target run gives a three times higher yield than for bismuth. This is not unexpected, considering that these values only reflect the probability for the heavy hypernuclei to decay through fission. The substantially higher fission barrier for bismuth, somewhat balanced by the larger probability for prompt fission decay in uranium, can probably account for the observed difference.

The two p_0-parameter estimates are practically the same, and they also agree with what was obtained from the prompt fission analysis (see Table 5.6 for the full compilation). Our data do not suggest any difference in the momentum transferred to the residual nucleus in hypernuclear-production and prompt-fission reactions, induced by stopped antiprotons.

In Fig. 6.4, the delayed-fission lifetimes obtained here, both for the uranium and the bismuth target, are compared to previous experimental results. Both lifetime estimates from the present experiment fall in the region of previous measurements.

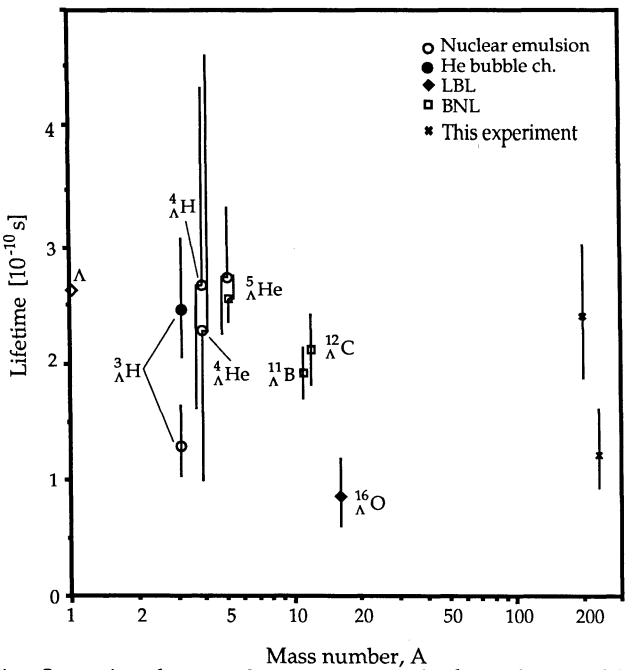

Fig. 6.4 : Comparison between the present result for heavy hypernuclei and earlier measurements on light and medium-heavy hypernuclei. See sub-section 2.2.4 for a review of the previous experiments. The error bars for the two data-points from this experiment include the systematical error, added in quadrature.

The value obtained in the analysis of the bismuth data is close to the free Λ lifetime, and hence similar to the lifetimes of the lightest hypernuclei, up to mass A = 5. However, the large error interval associated with this measurement also includes the recent data on ${}^{11}_{\Lambda}B$ and ${}^{12}_{\Lambda}C$ (Gra 85, Szy 87). Scaling our result to the decay rate of the free Λ gives :

$$\Gamma_{nm}(A \approx 200) = \left(1.10 \, {}^{+0.25}_{-0.23} \right) \cdot \Gamma_{\Lambda} \qquad (6.2).$$

The lifetime extracted from the analysis of the uranium target data is only one half of what is observed for the lightest hypernuclei and for the free Λ

decay. On the other hand, it is quite close to the result for the second-heaviest hypernucleus studied, i.e., $^{16}_{\Lambda}$O. There is no overlap between the 1σ error intervals of the present uranium result and those for $^{11}_{\Lambda}$B and $^{12}_{\Lambda}$C. In terms of the free Λ decay rate the uranium measurement gives

$$\Gamma_{nm}(A \approx 230) = \left(2.19 \, ^{+0.67}_{-0.46} \right) \cdot \Gamma_{\Lambda} \qquad (6.3).$$

A comparison between the experimental decay rates obtained here and the theoretical calculations for Λ decay in nuclear matter, discussed in sub-section 2.2.5, is shown in Fig. 6.5. The error bars associated with our measurements are quite large and they incorporate more or less the full range of theoretical predictions. Thus, it is very hard to differentiate between the various models.

Studying Fig. 6.5 in more detail, one observes that the only full-model result which agrees with our bismuth target measurement is the Dubach (Dub 86) calculation, including the full set of meson-exchange contributions. It should be mentioned, however, that in a recent critical review, McKellar (McK 86) has raised some questions about details in this calculation.

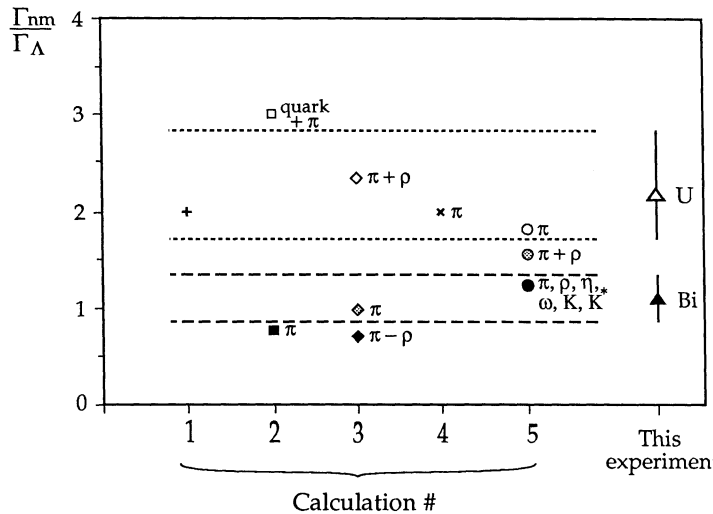

Fig. 6.5 : The results from the present experiment are compared to the theoretical calculations presented in sub-section 2.2.5. The calculations are performed by 1) Dalitz, 2) Heddle et al., 3) McKellar and Gibson, 4) Oset and Salcedo, 5) Dubach. The target used is given for the experimental points. The experimental 1σ error limits are indicated by dotted (uranium) and dashed (bismuth) parallel lines.

In the uranium case, both Dalitz (Dal 64) and McKellar-Gibson (McK 84), the latter in their calculation using a constructive, $\pi+\rho$-interference, find non-mesonic decay rates which fit the experimental result nicely. The Oset and Salcedo (Ose 85) result also fits well, although one has to bear in mind that this calculation takes into account pion-exchange only. The authors themselves use the Dubach result to infer a 25% reduction in the decay rate when the full set of meson-exchange contributions is added.

The results of the hybrid quark-hadron model (Hed 86) fall outside the range of our 1σ-error limits both for the pion-only contribution and for the complete calculation, including the quark-contribution.

In view of the large error bars for the present experimental data it is hardly meaningful to try to select one best model. Furthermore, the lifetime estimates from the uranium and the bismuth analyses differ by a factor two, a fact which needs to be understood. The 1σ errors assigned to the two data points, where the systematical error has been added in quadrature, do not overlap. Furthermore, due to the sharp uranium X^2-minimum and the rapid rise of the bismuth X^2-values towards the low-lifetime side, the error intervals start to overlap only at the 90% confidence level. Thus, the difference in the two results has a very small probability of being a statistical fluctuation. On the other hand, no significant difference in the lifetimes of hypernuclei in the mass regions of uranium and bismuth is expected.

However, the result presented by Noga et al. (Nog 86), discussed in subsection 2.2.4, suggests that there exists a second system with mass A=209, which also decays through delayed fission, but with a longer lifetime. In their experiment the long lifetime component was determined to be about 2.5 ns. It should be noted that there is no contradiction between the Kharkov result and ours : their measurement was not sensitive to lifetimes of the order of 0.2 ns. In our case, an activity of the order of 2 ns and with about the present yield would give very few registered events. Furthermore, our finding agrees qualitatively with theirs in so much as both groups measure lifetimes that are longer than expected in the mass region near bismuth.

In view of this complication, the result obtained with the uranium target can be taken as the estimate of the heavy-hypernuclear lifetime from this experiment. Three separate analyses, performed on the uranium data-sets presented here, all give the same result, within errors. Additionally, the same estimate was obtained in an earlier analysis, where data from a measurement with a slightly different experimental geometry was included (Appendix B). Moreover, the lifetime result has proven to be very stable

under the variation of several analysis parameters, as discussed in subsection 5.2.5.

The scenario discussed above also offers a quantitative explanation of the longer lifetime extracted for delayed fission in bismuth. If low-energy antiproton annihilation on bismuth is able to produce both "normal" heavy hypernuclei, characterized by a lifetime close to that found for uranium, and the long-lived objects, observed by Noga et al., then the extracted lifetime could be the best estimate based on the Monte Carlo model used here, where only one lifetime component is taken into account. At present it is not known in which proportion the two effects have to be detected to reproduce the present experimental result ; neither is it known if such a two-component approach would at all give a satisfactory explanation to the longer lifetime observed for delayed fission in bismuth.

In conclusion, we interpret the delayed-fission activity observed in the present experiment as due to the decay of heavy hypernuclei. The measured production rate, of the order 10^{-3} - 10^{-4}, is consistent with earlier findings of an enhanced Λ production in low-energy antiproton annihilation. The momentum distribution of the recoiling heavy hypernuclei is the same as that found for promptly-fissioning heavy nuclei, and it is given by :

$$N(p) = p \cdot \exp(- p/ \{375 \ [MeV/c]\}) \qquad (6.4).$$

In view of the recent observations of delayed-fission activity with two lifetime components in the mass region of bismuth, we take our uranium target result as a guide for the non-mesonic decay rate of heavy hypernuclei :

$$\Gamma_{nm}(_{\Lambda}A \approx 230) = \left(2.19 \, ^{+0.67}_{-0.46} \right) \cdot \Gamma_{\Lambda} \qquad (6.3).$$

The large error bars associated with the measurement makes a conclusive comparison with existing theoretical calculations difficult. However, some modern meson-exchange calculations do predict a value of this order, while others result in smaller rates. A hybrid quark-hadron model gives a higher decay rate value. It is interesting to note that already more than 20 years ago, Dalitz, in a simple calculation, obtained a value very close to that given in eq. 6.3.

The difference between the uranium and bismuth target results found in the present experiment should, and will, be subject to further studies.

Chapter 7 : APPENDIXES.

A. The least-squares method.

In this appendix the basics of the least-squares method will be treated. Most of the information has been collected from the books "Probability and statistics in particle physics" (Fro 79) and "Statistical methods in experimental physics" (Ead 71).

The aim of the work presented in this thesis is to estimate a set of parameters from a certain set of experimental data. Several methods exist to make such an estimation, such as the maximum likelihood method, the least-squares method and the moments method. The choice of the least-squares method in this work is to a certain extent arbitrary. However, it is clear that this method possesses some very attractive qualities : it is easy to use and to understand, it gives under certain conditions estimates that are consistent and of minimum variance and it also has the unique possibility to give a goodness-of-fit test. Furthermore, the least-squares method doeas not require any a priori knowledge about the distributional properties of the observations.

A.1 The basic principle.

The least-squares principle states that the best estimate of a set of unknown parameters $\underline{\theta} = \theta_1, \theta_2, \ldots \theta_L$ is that which minimizes the quantity

$$X^2 = \sum_{i=1}^{N} \left[\frac{y_i - f_i (\underline{\theta} ; x_i)}{\sigma_i} \right]^2 \qquad \text{(A.1)}$$

where x_i is an observational point,
y_i is the experimentally measured value at point x_i ,
f_i is the theoretically calculated value at point x_i for a certain set of $\underline{\theta}$,
σ_i is the estimated error in the i:th measurement.

As an example, take the case when the measurement y_i is the number of entries in a histogram bin. The calculated $f_i (\underline{\theta} ; x_i)$ is then given by

$$f_i (\underline{\theta} ; x_i) = n * p_i (\underline{\theta} ; x_i) \qquad \text{(A.2)}$$

where n is the total number of entries in the histogram,

x_i is the i:th class, i.e., bin,

p_i is the probability to get an observation in class i.

Under the condition of independent, Poisson distributed observations, the quantity to minimize is in this case

$$X^2 = \sum_{i=1}^{N} \left[\frac{y_i - np_i}{\sqrt{np_i}} \right]^2 \qquad \text{(A.3)}$$

where N is the total number of bins used in the calculation.

Asymptotically, for large number of entries, the Poisson distribution converges to the normal distribution. If the observations y_i are normally distributed about $f_i(\underline{\theta}; x_i)$, uncorrelated and with variance σ_i^2, then there is a direct connection between the least-squares method and the theoretically better founded maximum likelihood method.

The likelihood function to maximize is then

$$L(\underline{y}, \underline{\theta}) = \prod_{i=1}^{N} \frac{1}{\sqrt{2\pi\sigma_i^2}} \exp\left[-\left(\frac{y_i - f_i(\underline{\theta}; x_i)}{\sqrt{2}\sigma_i} \right)^2 \right] \qquad \text{(A.4).}$$

Taking the logarithm of this gives

$$\ln L(\underline{y}, \underline{\theta}) = -\frac{1}{2}\sum_{i=1}^{N} \ln(2\pi\sigma_i^2) - \frac{1}{2}\sum_{i=1}^{N} \left(\frac{y_i - f_i(\underline{\theta}; x_i)}{\sigma_i} \right)^2 \qquad \text{(A.5).}$$

The first term in this expression is a constant, and hence the whole $\ln L(\underline{y}, \underline{\theta})$ finds it maximum when the second term,

$$X^2 = \sum_{i=1}^{N} \left(\frac{y_i - f_i(\underline{\theta}; x_i)}{\sigma_i} \right)^2 \qquad \text{(A.6)}$$

is minimum.

Thus, under the specified conditions, the least-squares method is equivalent to the maximum likelihood method.

The set of parameters that minimizes X^2 is in what follows denoted by $\underline{\theta}_0$.

A.2 Confidence intervals and errors - the intersection method.

The question of errors in the parameter estimate, $\underline{\theta}_0$, can only be given an exact answer in the case of a theoretical model linear in the parameters. In such a case the calculated values at each observational point can be written as

$$f_i = \sum_{j=1}^{L} a_{ij}\,\theta_j \qquad \text{or in matrix notation} \qquad \underline{f} = A\,\underline{\theta} \tag{A.7}$$

where A is called the **design matrix.**

The function to minimize is then

$$X^2(\underline{\theta}) = [\,\underline{y} - A\,\underline{\theta}\,]^T\, V(\underline{y})^{-1}\,[\,\underline{y} - A\,\underline{\theta}\,] \tag{A.8}$$

where $V(\underline{y})^{-1}$ is the inverse of the symmetric covariance matrix. Each element in the matrix $V(\underline{y})$ is defined as $V_{ij} = \rho_{ij}\,\sigma_i\,\sigma_j$, where ρ_{ij} is the **correlation coefficient**. For uncorrelated variables only the diagonal elements are non-zero: $V_{ii} = \sigma_i^2$.

Differentiating X^2 with respect to the parameters gives the condition for the minimum as

$$\nabla_{\underline{\theta}}\, X^2(\underline{\theta}) = -\,2\,A^T\, V(\underline{y})^{-1}\,[\,\underline{y} - A\,\underline{\theta}_0\,] = \underline{0} \tag{A.9}$$

$$\therefore \qquad \underline{\theta}_0 = [\,A^T\, V(\underline{y})^{-1}\, A\,]^{-1}\, A^T\, V(\underline{y})^{-1}\;\underline{y} \tag{A.10}$$

i.e., the estimate $\underline{\theta}_0$ is a linear function of the observations $\underline{y}$.

The general formula for error propagation now gives the uncertainty in the linear least-squares estimate $\underline{\theta}_0$ as a function of the errors in the observations

$$V(\underline{\theta}_0) = S\,V(\underline{y})\,S^T \quad \text{where} \qquad \underline{\theta}_0 = S\,\underline{y} \tag{A.11}$$

$$\therefore \qquad S = [\,A^T\, V(\underline{y})^{-1}\, A\,]^{-1}\, A^T\, V(\underline{y})^{-1} \tag{A.12}.$$

Some straightforward matrix algebra then gives

$$V(\underline{\theta}_0) = [\,A^T\, V(\underline{y})^{-1}\, A\,]^{-1} \tag{A.13}$$

which already has been calulated when determining $\underline{\theta}_0$. Note, however, that $V(\underline{y})$ has to be completely known in order to determine $V(\underline{\theta}_0)$.

In the linear case there is a direct connection between the shape of the X^2 function and the error in the parameter estimate. Rewriting $\underline{\theta} = \underline{\theta}_0 + (\underline{\theta} - \underline{\theta}_0)$ and inserting this in the least-squares expression A.8 gives

$$X^2(\underline{\theta}) = [\, \underline{y} - A\,(\,\underline{\theta}_0 + (\underline{\theta} - \underline{\theta}_0)\,)\,]^T\, V(\underline{y})^{-1}\, [\, \underline{y} - A\,(\,\underline{\theta}_0 + (\underline{\theta} - \underline{\theta}_0)\,)\,] =$$

$$= [\, \underline{y} - A\underline{\theta}_0 - A(\underline{\theta} - \underline{\theta}_0)\,)\,]^T\, V(\underline{y})^{-1}\, [\, \underline{y} - A\underline{\theta}_0 - A(\underline{\theta} - \underline{\theta}_0)\,)\,] \qquad \text{(A.14).}$$

Carrying out the multiplication, the "quadratic" terms give

$$[\, \underline{y} - A\underline{\theta}_0\,]^T\, V(\underline{y})^{-1}\, [\, \underline{y} - A\underline{\theta}_0\,] = \quad X^2_{min} \qquad \text{(A.15)}$$

$$[\, A(\underline{\theta} - \underline{\theta}_0)\,]^T\, V(\underline{y})^{-1}\, [\, A(\underline{\theta} - \underline{\theta}_0)\,] = (\underline{\theta} - \underline{\theta}_0)^T\, V(\underline{\theta}_0)^{-1}\, (\underline{\theta} - \underline{\theta}_0) \qquad \text{(A.16)}$$

The cross-terms disappear due to the condition from the differentiation, expression A.9, and the symmetry property of the covariance matrix. Collecting the remaining terms gives

$$X^2\,(\underline{\theta}) = X^2_{min} + (\underline{\theta} - \underline{\theta}_0)^T\, V(\underline{\theta}_0)^{-1}\, (\underline{\theta} - \underline{\theta}_0) \qquad \text{(A.17).}$$

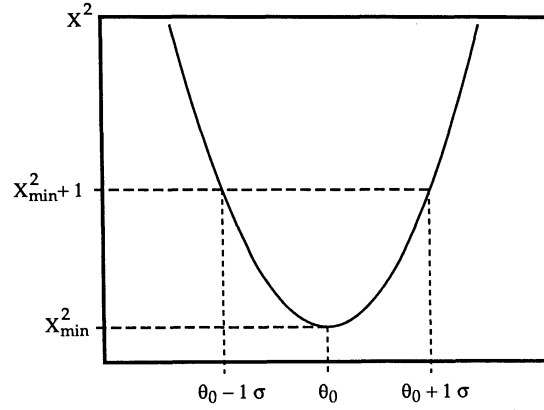

Fig. A.1 : Principle of the intersection method.

It can be shown under quite general conditions (Ead 71) that for a large number of observations the parameter estimate, $\underline{\theta}_0$, will asymptotically be normally distributed around the true value. Consequently, when the observations are independent, multinormally distributed variables (Fro 79, pg 316) all terms in expression A.17 are chi-square distributed. It is immediately clear that the residual sum of squares at the minimum, X^2_{min}, and the error in the parameters, $V(\underline{\theta}_0)$, are independent of each other. Thus, the X^2_{min} value can be used in a goodness-of-fit test, as explained in the next section, while the shape of the X^2 function, as given by the $(\underline{\theta} - \underline{\theta}_0)^T\, V(\underline{\theta}_0)^{-1}\, (\underline{\theta} - \underline{\theta}_0)$ term, is directly connected to the error in $\underline{\theta}_0$.

The expression A.17 suggests a graphically very illustrative way to evaluate the error in the parameter estimate. By intersecting the X^2_{min} curve with straight lines at certain levels, **a**, above the minimum, the corresponding confidence regions can be determined. This can be seen by the following identities (assuming only one parameter for simplicity) :

$$X^2(\theta) = X^2_{min} + a \qquad where \qquad a = \frac{(\theta - \theta_0)^2}{V(\theta_0)} \tag{A.18}$$

$$\therefore \quad \theta - \theta_0 = \sqrt{a}\ \sigma(\theta_0) \quad since \quad \sigma(\theta_0)^2 = V(\theta_0) \tag{A.19}.$$

Hence, intersecting the X^2 curve at a level $\mathbf{a} = 1^2$ above the minimum gives the 1σ region, at a level $\mathbf{a} = 2^2$ gives the 2σ region and so on. The procedure is schematically shown in Fig. A.1. The confidence levels (CL) corresponding to the different choices of **a** are extracted from the ordinary normal distribution according to Table A1. The confidence level is defined as shown in Fig. A.2.

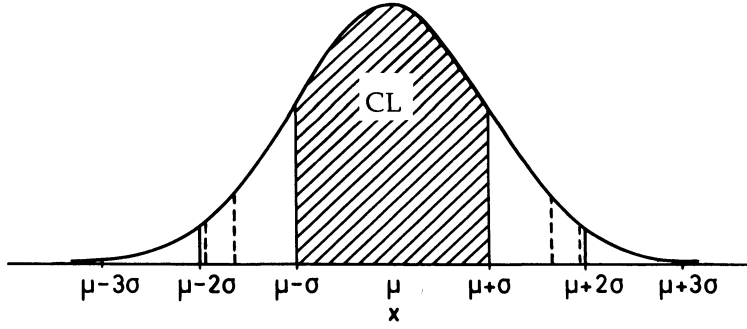

Fig. A.2 : Definition of confidence interval for the normal distribution. The integral over the shaded area gives the 1σ confidence level (CL). From ref. Fro 79.

For the linear model, the identities in expressions A.18 and A.19 are exact under the conditions of a constant covariance matrix $V(\underline{\theta}_0)$ and unbiassed, uncorrelated and multinormally distributed observations (Fro 79, pg 316).

CL (%)	a	CL (%)	a
68.3	1 (1σ)	90.0	2.69 (1.64σ)
95.4	4 (2σ)	95.0	3.84 (1.96σ)
99.7	9 (3σ)	99.0	6.66 (2.58σ)

Table A1 : Confidence intervals for the normal distribution certain choices of a.

For the non-linear case, or when the covariance matrix is not independent of $\underline{\theta}$, the distributional properties of the terms in expression A.17 are not known. Nevertheless, it is still customary to use the intersection method to give approximate confidence intervals also in this case. Making a Taylor expansion around the minimum gives

$$X^2(\theta) = X^2_{min} + \frac{1}{2}\left[\frac{\delta^2 X^2}{\delta\theta^2}\right]_{\theta=\theta_0} (\theta - \theta_0)^2 + \ldots \qquad \text{(A.20).}$$

Since the expansion is made around the minimum the second derivative is clearly positive. If the higher order terms in expression A.20 are small, corresponding to an approximately parabolic shape of the X^2 curve, one can make the identification

$$V(\underline{\theta}_0) = 2\left[\frac{\delta^2 X^2}{\delta\theta^2}\right]^{-1}_{(\underline{\theta}=\underline{\theta}_0)} \qquad \text{(A.21).}$$

Thus, under these conditions the intersection method gives a good approximation of the error also in the case of a non-linear model. How good this approximation is, will in general depend on the magnitude of the higher-order terms in expression A.20 as well as on the validity of the assumption of normally distributed observations.

The intersection method to deduce the errors in the estimated parameters has been adopted in this thesis.

A.3 Goodness-of-fit test.

To evaluate the f_i's in, e.g., the X^2 expression A.6 one has to invent a model which is believed to reproduce the experimental conditions. If the assumptions made in this model are correct then, in the limit of large numbers of events, the $X^2(\underline{\theta})$ in expression A.6 is a sum of squared standard normal variables. Such a sum is distributed as a chi-square variable with ν degrees of freedom, $\chi^2(\nu)$. When the least-squares method is applied to binned data, $\nu = N - 1$ with N equal to the number of bins. In this case one degree of freedom has been lost due to the normalization of the model calculation to the experimental number of events.

More specifically, the residual sum of squares at the minimum, X^2_{min}, is distributed as a $\chi^2(\nu=N-1-L)$ variable, where L is the number of independent parameters. The χ^2 function is shown in Fig. A.3 for $\nu=1$ to $\nu=20$. The mean of the $\chi^2(\nu)$ distribution is ν and the variance is 2ν.

On the other hand , if the assumptions in the model are <u>not</u> correct, the X^2_{min} will, on average, tend to become larger than if they were true. This then offers a possibility to use the appropriate cumulative $\chi^2(\nu)$ distribution to test the hypothesis made.

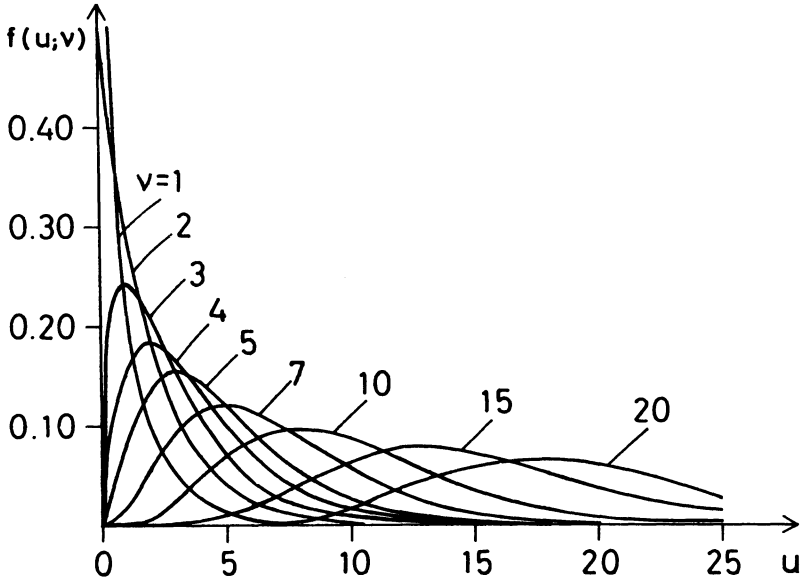

Fig. A.3 : The chi-square distribution for n = 1 - 20. From ref. Fro 79.

Define the quantity α as

$$\alpha = \int_{X^2_{min}}^{\infty} \chi^2(u\,;\,\nu)\,du = 1 - F(u = X^2_{min}\,;\,\nu) \qquad \text{(A.22)}$$

where F is the cumulative integral of the $\chi^2(\nu)$ distribution from 0 to X^2_{min} (see Fig.A.4). The quantity α then expresses the probability to get a higher value of X^2_{min} in a new measurement. If this probability is smaller than a certain fixed α_0 then there is a good reason to be sceptical about the underlying model.

Since the mean of the chi-square distribution is equal to the number of degrees of freedom, ν, this is also the X^2_{min} value one expects to find. This is the basis for the popular "rule-of-thumb" saying that the reduced chi-square, $\chi^2(\nu)/\nu$, should be approximately unity. For a large number of degrees of freedom, $\nu \gtrsim 5$, $\chi^2(\nu)/\nu \approx 1$ corresponds to an α of close to 50%.

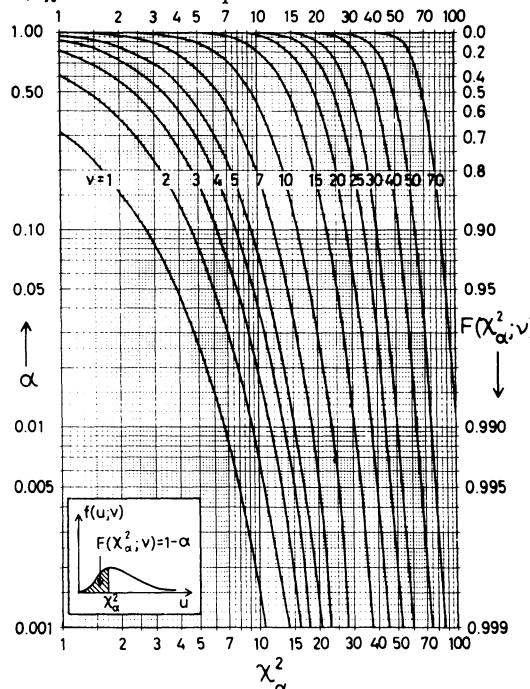

Fig. A.4 : The probability contents of the chi-square distribution for different number of degrees of freedom. F and α are defined in the text, expression A.22. From ref. Fro 79.

B. OBSERVATION OF THE DELAYED FISSION INDUCED BY ANTOPROTON ANNIHILATION IN ^{238}U.

Physics Letters *B182* (1986) 146.

OBSERVATION OF THE DELAYED FISSION INDUCED BY ANTIPROTON ANNIHILATION IN ^{238}U

J.P. BOCQUET [a,1], M. EPHERRE-REY CAMPAGNOLLE [b,2], G. ERICSSON [c], T. JOHANSSON [c], J. KONIJN [d], T. KROGULSKI [e], M. MAUREL [a], E. MONNAND [a], J. MOUGEY [f,3], H. NIFENECKER [a], P. PERRIN [a], S. POLIKANOV [g], C. RISTORI [a] and G. TIBELL [c]

[a] *Centre d'Etudes Nucléaires de Grenoble, BP 85X, F-38041 Grenoble Cedex, France*
[b] *Laboratoire René Bernas du CSNSM, BP 1, F-91406 Orsay, France*
[c] *Gustaf Werner Institute, P.O. Box 531, S-751 21 Uppsala, Sweden*
[d] *NIKHEF, P.O. Box 4395, NL-1009 AJ Amsterdam, The Netherlands*
[e] *University of Warsaw, Branch in Bialystok, PL-15-424 Bialystok, Poland*
[f] *Centre d'Etudes Nucléaires de Saclay, F-91191 Gif-sur-Yvette, France*
[g] *GSI, Postfach 110541, D-06100 Darmstadt, Fed. Rep. Germany*

Received 25 July 1986

Delayed fission following the annihilation of antiprotons at rest in ^{238}U nuclei has been observed with a yield of approximately 10^{-3}. By means of the recoil-distance technique a lifetime of about 10^{-10} s has been determined for the delayed fission; this is interpreted as due to the non-mesonic decay of heavy hypernuclei.

Present values for the lifetimes of lambda hypernuclei were mainly measured in experiments with kaon beams. The most accurate results have been obtained for $^{12}_{\Lambda}$C and $^{11}_{\Lambda}$B [1], for which the lifetime was found to be somewhat shorter than that of the free Λ hyperon. It was also shown that for $^{12}_{\Lambda}$C the mesonic channel of decay $\Lambda \rightarrow N+\pi$ is strongly suppressed in comparison with the non-mesonic channel $\Lambda+N \rightarrow n+N$. One can expect that for heavier hypernuclei the non-mesonic decay mode will dominate even more.

In the decay of heavy Λ-nuclei the de-excitation of the residual nucleus can proceed through the fission channel. Accordingly, the decay can be recognized by the observation of delayed fission: measuring the lifetime of heavy hypernuclei in the region of U can be done by measuring the lifetime for delayed fission.

However, the well-established electronic methods of hypernuclear spectroscopy and lifetime measurements do not seem promising in this particular case. The formation of a heavy hypernucleus would be difficult to tag by the strangeness-exchange reaction $K^- + A \rightarrow {}_{\Lambda}A + \pi^-$ since no well-resolved low excited states of hypernuclei are expected here. Consequently, the decay of heavy hypernuclei which is to be observed through delayed fission would be measured in the presence of a substantial background of prompt events. In addition, measuring lifetimes of the order of 10^{-10} s by means of electronic techniques involves rather complicated procedures (see for example, ref. [1]).

In the work described here we have searched for delayed fission following the annihilation of antiprotons in a ^{238}U target. Indeed, the annihilation is in some cases accompanied by the emission of K^+, K^- pairs, and a Λ hyperon can be produced in a secondary interaction of K^- with a nucleon in the residual nucleus: $K^- + N \rightarrow \Lambda + \pi$. Cugnon and Vandermeulen [2] investigated the annihilation of antiprotons by two nucleons inside a nucleus. Their calculations, which were inspired by an earlier remark by Rafelski

[1] Present address: Institut Laue-Langevin, F-38041 Grenoble, France.
[2] Present address: CERN, CH-1211 Geneva 23, Switzerland.
[3] Present address: CEBAF, 12070 Jefferson Ave., Newport News, VA 23606, USA.

0370-2693/86/$ 03.50

[3], predict a substantial increase in the production of Λ particles and were experimentally confirmed by Condo et al. [4].

The experimental method used is based on the recoil-distance technique, which was developed for the study of short-lived fission isomers [5]. Fig. 1a recalls the principle of the recoil-distance method.

Since prompt fission of nuclei, following the annihilation of antiprotons, occurs after about 10^{-18} s, the fissioning nucleus remains in the target. As a result, the fragments are emitted from the target plane, and those directed towards the upstream hemisphere will be stopped in the target or its backing and will not be recorded in the detectors (fig. 1a). On the other hand, hypernuclei with lifetimes of the order of 10^{-10} s can leave the target and decay at some distance from the target plane. Some of the fragments produced in this decay are emitted towards the upstream hemisphere, shadowed by the target backing, and will hit the detector.

The distribution of recoil distances, and therefore of the positions of events recorded in the shadowed area of the detector, depends on the lifetime of the hypernuclei and on their velocity. Hence, on the basis of the measured position distribution we can evaluate the lifetime of the hypernuclei. The accuracy of the result of such an evaluation will depend on the extent to which the momentum distribution of hypernuclei is known. In the case where the stopped antiproton is annihilated, the momentum of the recoil nucleus, in our case the hypernucleus, results from adding the momenta of particles emitted in the annihilation of the antiproton. We cannot rely on any calculation of the momentum distribution of hypernuclei produced in the antiproton annihilation. In our analysis we only made use of that information of the momenta of hypernuclei which was contained in our experimental data.

Our experiment was carried out in an antiproton beam from the Low Energy Antiproton Ring (LEAR) at CERN. The beam momentum was 200 and 100 MeV/c, respectively, in two different experimental periods. A schematic view of our experimental set-up is shown in fig. 1b. After passing through two thin windows separating our set-up from the LEAR vacuum, and through the hole in the scintillator veto counter, the antiprotons were slowed down mainly in the 200 μm thick plastic scintillator on which the U target was deposited as a spot 2×5 mm^2 and 0.1 mg/cm^2 thick. This scintillator was also used to detect

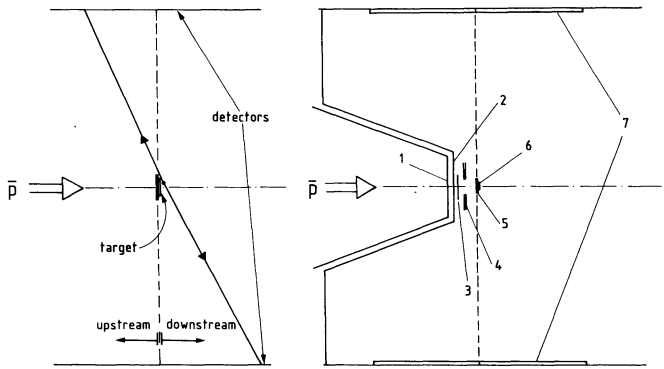

Fig. 1. (a) Principle of the recoil-distance method. (b) Schematic view of the experimental set-up. 1: Be window (100 μm thick). 2: Kapton window (25 μm thick). 3: Degrader, variable in steps of 5 μm mylar foils. 4: 1 mm thick plastic scintillator with a 6 mm×3 mm hole. 5: 200 μm thick plastic scintillator. 6: 0.1 mg/cm^2 thick U target. 7: parallel-plate avalanche counters with dimensions 190 mm×290 mm.

the antiprotons, thus providing a zero-time signal. The U targets were deposited on backings of two different widths, 2.5 and 10 mm. They were flat to within 1 μm over their surfaces. An adjustable degrader made of Mylar foils was used to optimize the stopping rate of antiprotons in the target. Fission fragments were recorded by two parallel-plate avalanche counters which were filled with isobutane at a pressure of 7 mb and placed symmetrically with respect to the target at a distance of 250 mm.

A fission event could be identified unambiguously by the registration of the time of flight of coincident fragments, as well as by the ionization which these produce in the counters.

Fig. 2 shows the two position distributions of fission events along the beam direction. The sharp edges of measured profiles define a position of the target plane which is consistent with the position determined in the setting-up. It is clearly seen from the figure that the distribution for the 2.5 mm wide backing contains more events in the shadowed area. These latter events can only by explained as a result of delayed fission. A total of 100 delayed-fission events have been recorded with the 2.5 mm wide target backing.

The measured positions of events permit one to determine the distribution of angles between fragment trajectories (opening angles). For binary fission these angles depend on the initial momenta of the fissioning nuclei and on the total kinetic energy release (one can neglect a small effect due to the emission of neutrons from the fragments). In our experimental technique the detection efficiency of delayed-fission fragments is a function of the distance which hypernuclei travel before they decay. Consequently, the measured distribution of opening angles is also dependent on the lifetime of hypernuclei.

The measured distributions of positions and angles were compared with the results of Monte Carlo calculations with two parameters pertaining to the fissioning recoil nuclei: their lifetime and one parameter describing their momentum distribution. We assumed this distribution to be approximated by the formula $N(p) = \exp(-p/p_0)$, with one free parameter p_0. This is a purely phenomenological approach, in which we ignore details of the various processes governing the momentum distribution of hypernuclei. However, by choosing an exponential we try to take into account the fact that some of the recoil nuclei may lose a considerable amount of energy before leaving the target.

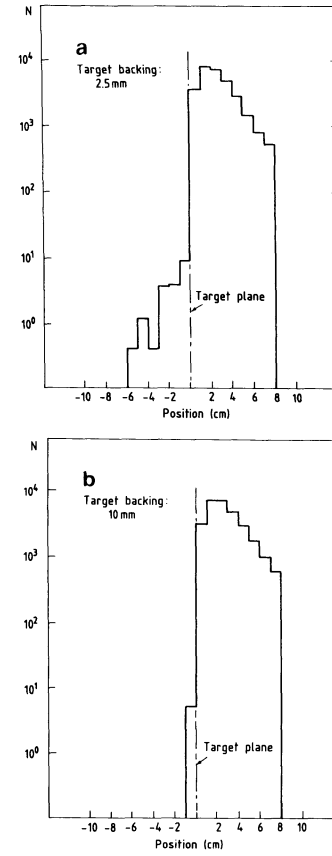

Fig. 2. Distributions of the fission-fragment positions in the detectors along the beam direction, obtained from the U targets with (a) 2.5 mm, and (b) 10 mm wide backing. The two distributions are normalized to the same total number of events.

For delayed fission the measured distribution of

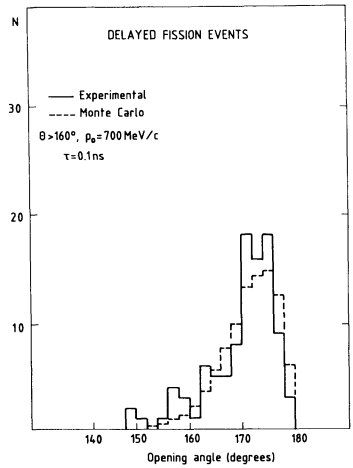

Fig. 3. Distributions of opening angles for the delayed fission fragments. The calculated distribution (dashed line, reduced $\chi^2 = 1.23$) is normalized to the number of experimental events with opening angles larger than 160° (89 events).

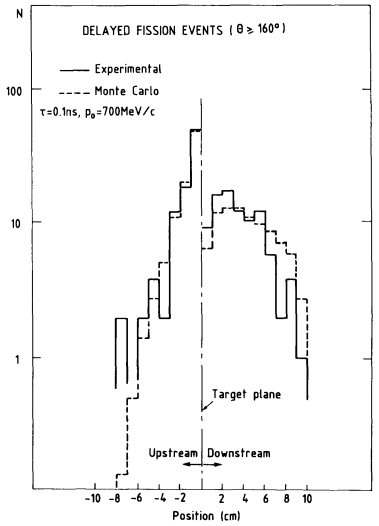

Fig. 4. Measured and calculated distributions of the delayed fission fragment positions along the beam direction. The experimental distribution (solid line) shows the total number of events obtained with opening angles larger than 160°, using the U target with 2.5 mm wide backing. It should be noted that each event is represented by entries in the distributions on either side of the target plane. The values of the reduced χ^2 for upstream and downstream ranges are, respectively, 0.82 and 1.36.

opening angles is presented in fig. 3 together with the best fit from the Monte Carlo calculation (dashed line). We can see a substantial disagreement for events with an opening angle less than 160°. The formula which was chosen for the momentum distribution in the Monte Carlo calculations obviously does not represent these events in an adequate way. These events correspond to high momenta of the recoil nuclei, possibly due to fragmentation processes. Therefore, we have excluded from the fitting procedure angles less than 160°. Fig. 4 gives the position distribution of the remaining 89 events along the beam direction, and the dashed line is the best fit to the experimental distribution. The two calculated distributions shown in figs. 3 and 4 give the following values of the parameters:

$$\tau = (0.1^{+0.1}_{-0.05})\ \text{ns}, \quad p_0(700 \pm \tfrac{500}{300})\ \text{MeV}/c,$$

where the errors correspond to 95% confidence level in χ^2, and the two parameters were considered as uncorrelated.

Therefore, our results indicate that some products of the annihilation of antiprotons in ^{238}U undergo delayed fission with a lifetime of about 10^{-10} s. The yield of these products is about 10^{-3} per stopped antiproton, and the measurement of fragment velocities indicates a symmetric mode of fission.

Fission isomers with lifetimes close to 10^{-10} s have been observed for a few Pu isotopes. However, even in the most favourable reactions induced by protons, deuterons, or alpha particles, their yield is several orders of magnitude less than in our experiment. In addition, the decay of fission isomers is characterized by asymmetric fission.

The lifetime for delayed fission measured in our experiment is close to the lifetime measured for light hypernuclei [1,6] and is also within the range of values predicted by different models [7], for the non-

mesonic decay which is expected to predominate in heavy hypernuclei. Therefore, one plausible explanation of our results is that we observe delayed fission arising from the decay of hypernuclei of isotopes in the U region which were produced in the annihilation of antiprotons in ^{238}U nuclei. This conclusion is consistent with recent observations of the enhanced emission of Λ hyperons when antiprotons are annihilated at rest in complex nuclei [4]. It could be checked experimentally by recording the delayed-fission events in coincidence with the K^+ produced simultaneously with the Λ hyperon in the annihilation process. This measurement was not possible with the present intensity of the antiproton beam, but it will be feasible in the future, after improvements of the antiproton beams.

We are indebted to the LEAR staff for providing a low-energy antiproton beam of very high quality. Special thanks are due to N. Mezin and J. Place from the CERN West Workshop who performed the precision mechanics of the apparatus. We also thank D. Ledu and R. Meunier from the PARIS implanter at the CSNSM who prepared the U targets.

References

[1] R. Grace et al., Phys. Rev. Lett. 55 (1985) 1055.
[2] J. Cugnon and J. Vandermeulen, Phys. Lett. B 146 (1984) 16.
[3] J. Rafelski, Proc. Workshop on Physics at LEAR with low-energy cooled antiprotons (Erice, 1982), eds. U. Gastaldi and R. Klapisch (Plenum, New York, 1984) p.507.
[4] G.T. Condo et al., Phys. Rev. C 29 (1984) 1531.
[5] W. Metag et al., Nucl. Instrum. Methods 114 (1974) 445.
[6] R.J. Prem and P.H. Steinberg, Phys. Rev. 136 (1964) B1803; G. Bohm et al., Nucl. Phys. B 16 (1970) 46, B 23 (1970) 93; G. Keyes et al., Nucl. Phys. B 67 (1973) 269; K.J. Nield et al., Phys. Rev. C 13 (1976) 1263.
[7] M.M. Block and R.J. Dalitz, Phys. Rev. Lett. 11 (1963) 96; C.Y. Cheung et al., Phys. Rev. C 27 (1983) 335; B.H.J. McKellar and B.F. Gibson, Phys. Rev. C 30 (1984) 335.

C. DELAYED FISSION FROM THE ANTIPROTON ANNIHILATION IN ^{209}Bi - EVIDENCE FOR HYPERNUCLEAR DECAY.

Physics Letters *B192* (1986) 312.

DELAYED FISSION FROM THE ANTIPROTON ANNIHILATION IN ^{209}Bi - EVIDENCE FOR HYPERNUCLEAR DECAY

J.P. BOCQUET [a,1], M. EPHERRE-REY-CAMPAGNOLLE [b,2], G. ERICSSON [c], T. JOHANSSON [c], J. KONIJN [d], T. KROGULSKI [e], M. MAUREL [a], E. MONNAND [a], J. MOUGEY [f,3], H. NIFENECKER [a], P. PERRIN [a], S. POLIKANOV [g], C. RISTORI [a] AND G. TIBELL [c]

[a] *Centre d'Études Nucléaires de Grenoble, BP 85X, F-38041 Grenoble Cedex, France*
[b] *Laboratoire René Bernas du CSNSM, BP 1, F-91406 Orsay, France*
[c] *Gustaf Werner Institute, Box 531, S-75121 Uppsala, Sweden*
[d] *NIKHEF, P.O. Box 4395, NL-1009 AJ Amsterdam, The Netherlands*
[e] *University of Warsaw, Branch in Bialystok, PL-15-424 Bialystok, Poland*
[f] *Centre d'Études Nucléaires de Saclay, F-91191 Gif-sur-Yvette, France*
[g] *Gesellschaft für Schwerionenforschung, Postfach 110541, D-6100 Darmstadt, Fed. Rep. Germany*

Received 26 January 1987

Delayed fission following the annihilation of stopped antiprotons in ^{209}Bi has been observed with a yield of approximately 3×10^{-4}. The lifetime for delayed fission as measured by the recoil-distance technique is $(2.5^{+2.0}_{-1.0})\times10^{-10}$ s. The observed delayed fission is interpreted as resulting from the decay of hypernuclei in the region of masses near 200 produced in the annihilation of antiprotons in ^{209}Bi.

In a previous paper [1] we have reported the observation of delayed fission following the annihilation of antiprotons at rest in ^{238}U. We used the recoil-distance technique, where the lifetime is inferred from a distribution of fission fragment impacts in a detector placed in such a geometry that one can distinguish events with different decay points with respect to the target plane. (See ref. [1] for details of the experimental technique.)

The value of the lifetime reported in ref. [1], $\tau=(1.0^{+1.0}_{-0.5})\times10^{-10}$ s, was determined from comparing the experimentally measured position distribution of events with a calculated one using the Monte Carlo method. The yield of delayed-fission events was found to be close to 10^{-3} per stopped antiproton. The interpretation given in ref. [1] is that the delayed fission results from the decay of hypernuclei produced in the annihilation of antiprotons in the ^{238}U nuclei.

In the present work we report results obtained with a ^{209}Bi target in an experiment carried out at the Low Energy Antiproton Ring (LEAR) at CERN, with the same set-up that we used in our previous experiment [1]. The antiproton beam momentum was 100 MeV/c. With a Bi target, 0.1 mg/cm^2 thick and 2 mm wide, deposited on a 2.5 mm wide backing, 155 delayed-fission events have been collected.

As in our previous work the detection system consisted of two parallel-plate avalanche counters filled with isobutane at a pressure of 7 mb. For each of those two fragments recorded in coincidence the following information was obtained: (i) two coordinates determining the position of each fragment in the detector with an accuracy of the order of 1 mm; (ii) the time-of-flight value (the zero-time signal being provided by the scintillation counter recording antiprotons); and (iii) the ionization produced in the counter. By calibrating the counters with a Cf source of spontaneous fission, we were able to determine the region of ionization and time-of-flight val-

[1] Present address: Institut Laue Langevin, F-38041 Grenoble, France.
[2] Present address: CERN, EP Division, CH-1211 Geneva 23, Switzerland.
[3] Present address: CEBAF, Newport News, VA 23606, USA.

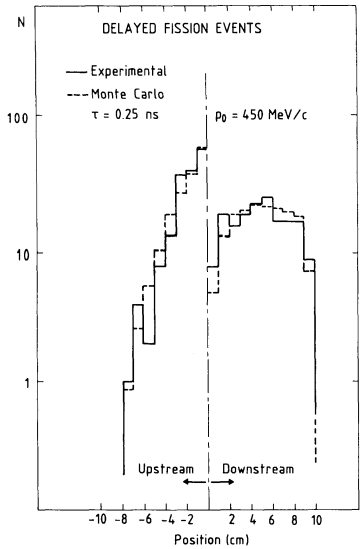

Fig. 1. Measured and calculated distributions of the positions of delayed-fission fragments along the beam direction. The values of the reduced χ^2 for upstream and downstream ranges are 1.53 and 0.89, respectively. The 1 cm bin width, adopted because of the low statistics, is much larger than the resolution of the detector (~ 1 mm).

ues corresponding to fission fragments. Consequently, the delayed and prompt fission events recorded in our experiment were unambiguously separated from the background arising from the low-ionization particles produced in the annihilation of antiprotons in nuclei.

Fig. 1 shows the position distribution of fission fragments registered in the detector area shadowed by the target (negative values of coordinates), as well as the position distribution of coincident complementary fragments (positive values of coordinates). According to the principle of the recoil-distance technique, all these fragments correspond to delayed-fission events. Fig. 2 shows the distribution of the angles between the delayed-fission fragment trajectories (opening angles). It was determined from the positions of fragment impacts in the fission chambers.

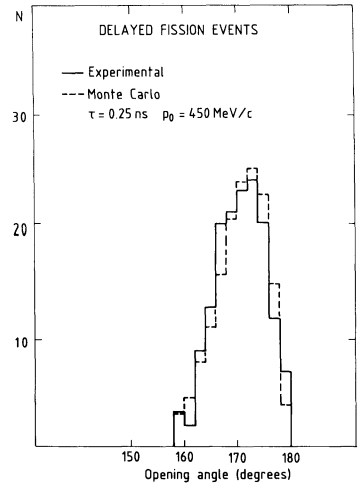

Fig. 2. Measured and calculated distributions of the opening angles of the delayed-fission fragments. In the Monte Carlo calculation, events with an angle smaller than 158° have been eliminated. The corresponding reduced χ^2 has a value of 0.71.

In the analysis of our present data the main purpose was the determination of the lifetime for delayed fission, and we followed the same procedure as in ref. [1]. Remaining within the framework of a phenomenological approach and using, as in ref. [1], a purely exponential momentum distribution of recoil nuclei knocked out from the target $N(p) = \exp(-p/p_0)$, we obtained a lifetime of

$$\tau = (2.5^{+2.5}_{-1.0}) \times 10^{-10} \text{ s},$$

where the errors correspond to the 95% confidence level in χ^2. It turned out that all three measured distributions were characterized by a rather flat dependence of χ^2 on p_0.

Using a different momentum distribution, of the form $N(p) = p \exp(-p/p_0)$, we obtained the same value of the lifetime (and its uncertainty) but a more pronounced dependence of χ^2 on p_0. The distributions calculated with this modified expression for the momentum distribution are shown in figs. 1 and 2; they correspond to the overall best fit to the experimental results.

As an additional check of the consistency of our procedure, the previously published data for uranium [1] were re-analysed with the modified momentum distribution $N(p)=p\exp(-p/p_0)$. The following values of the parameters were found:

$$\tau=(1.0^{+0.8}_{-0.4})\times10^{-10}\ \text{s}\,,\quad p_0=300\ \text{MeV}/c\,.$$

The value of the lifetime reproduces the estimate given in ref. [1]. On the other hand, the value of p_0 for uranium is somewhat different from the value of p_0 for bismuth, given in figs. 1 and 2.

Slightly different momentum distributions of hypernuclei undergoing delayed fission can be expected for uranium and bismuth for the following reasons:

(i) the probability of survival of an excited heavy hypernucleus is determined by the branching ratio for the fission channel which is a function of the excitation energy, and this dependence is different for nuclei in the regions of bismuth and uranium;

(ii) as indicated by calculations [2] some correlation may exist between the excitation energy and the momentum of residual nuclei.

The yield of delayed-fission events for ^{209}Bi is about 3×10^{-4} per stopped antiproton, which is lower by a factor of 3 than observed with ^{238}U [1]. Whereas a difference in yields could be explained by different fissility of nuclei in the regions of bismuth and uranium, the lifetimes measured for uranium and bismuth are still equal within the limits of quoted errors.

As in ref. [1] we cannot suggest any other interpretation of our present results than that we observe delayed fission arising from the decay of hypernuclei, produced in the annihilation of $\bar{p}$ in bismuth. Note that in ref. [1] we rejected the decay of fission isomers as an extremely unlikely explanation. Our present result completely excludes this hypothesis since no fission isomers are known to exist in the region of bismuth.

The present measurement does not show direct evidence for strangeness production in the investigated process. However, Condo et al. [3] observed Λ production in $\bar{p}$ annihilation on complex nuclei, with a yield of about 2%. Assuming the probability of attachment of the Λ hyperon to a heavy nucleus to be of the same order of magnitude whether it is produced in $\bar{p}$ annihilation or with stopping K^- [4], the yield of delayed fission observed in our experiment is quite reasonable.

In a recent experiment performed at the Kharkov linear electron accelerator [5], delayed fission was observed following the interaction of 1.2 GeV electrons with a ^{209}Bi target. It was likewise interpreted as resulting from hypernuclear decay. The reported lifetime is (2.7 ± 0.5) ns. The yield of delayed fission per nuclear reaction is 100 times higher in our experiment than in the experiment with electrons. For that reason we cannot exclude the possible production of long-lived hypernuclei at a level two orders of magnitude below our experimental result. On the other hand, with the set-up used in Kharkov, a 0.5 mm systematic error is quoted for the recoil ranges which could prevent the observation of any short lifetime. Consequently, it seems worthwhile to investigate both components in the same experiment.

References

[1] J.C. Bocquet et al., Phys. Lett. B 182 (1986) 146.
[2] A.S. Iljinov et al., Nucl. Phys. A 382 (1982) 378.
[3] G.T. Condo et al., Phys. Rev. C 29 (1984) 1534.
[4] M. Csejthey-Barth et al., Nucl. Phys. B 14 (1969) 330.
[5] V.I. Noga et al., Yad. Fiz. 43 (1986) 1332.

Chapter 8 : ACKNOWLEDGEMENTS.

This thesis would not have been possible without the kind assistance, encouragement and help from a number of people. Only some of them will be mentioned here, but no-one is forgotten.

I wish to express my deep gratitude to my supervisor Gunnar Tibell for all his support during the years we have worked together. Not only did he introduce me to the PS177 experiment and to CERN, but he has also been continuously available to share his knowledge and ideas about every aspect of the work presented here.

My sincere thanks also go to my assistant supervisor Tord Johansson, who helped me get along both professionally and practically during my years at CERN. He also introduced me to the PS185 experiment, working for which has been an rewarding experience.

The hard work of the whole PS177 collaboration is gratefully acknowledged; without all these people the experiment could never have been accomplished. Special thanks are due to Marcelle Rey-Campagnolle, for all her enthusiasm and help during all this time, to Sergei Polikanov, for sharing his great knowledge about the physics of our experiment, and to Tadek Krogulski and Christian Ristori, who helped me understand parts of the equipment.

I am very thankful for the support of everybody at the Department of Radiation Sciences (former Gustaf Werner Institute). In particular I wish to mention Teddy Törnlund who made the photos and Birgitta Holmgren and Birgitta Olsson for helping me with a lot of important practical things.

I also wish to express my appreciation to all my friends in Geneva who made the long stays in Switzerland a pure pleasure. In particular I'm grateful to Marie Owens, Robin Martini, Anna-Lena Andersson, Claes Looft and Jörg Rickstein for the hospitality they showed me during various periods of work at CERN.

A special thanks also go to my friend Rikard Erlandsson for many interesting discussions about the research methods used in different branches of natural science.

REFERENCES.

Ait 82 I.J.R.Aitchison and A.J.G. Hey, "Gauge Theories in Particle Physics", Adam Hilger Ltd 1982.

And 87 L.N.Andronenko et al., Sov. J. Part. Nucl. *18 (4)* (1987) 289.

Ang 88 A.Angelopoulos et al., Phys. Lett. *B205* (1988) 590.

Arm 69 R.Armenteros and B.French, in High Energy Physics, Vol. 4, ed. E.H.S.Burhop, Academic Press 1969, p.309.

Agu 86 M.Aguilar-Benitez et al., (Particle Data Group), "Particle Properties Data Booklet", North-Holland 1986.

Bal 86 F.Balestra et al., Nucl. Phys. *A452* (1986) 573.

Bal 87 F.Balestra et al.,Phys. Lett. *B194* (1987) 192.

Ban 86 H.Bandō, O.Hashimoto, K.Ogawa (editors), Proc. 1986 INS Int. Symp. on Hypernuclear Physics, Toseisha Printing Co. 1986.

Bar 86 P.D.Barnes and J.J.Szymanski, Proc. 1986 INS Int. Symp. on Hypernuclear Physics, Toseisha Printing Co. 1986, eds H.Bandō, O.Hashimoto, K.Ogawa, p.136.

Bar 88 P.D.Barnes, Nucl. Phys. *A479* (1988) 89c.

Bat 76 Y.A.Batusov et al., Sov. J. Nucl. Phys. 23, no 6 (1976) 621.

Bec 83 F.D.Becchetti et al., Phys. Rev. *C28* (1983) 276.

Ber 85 M.Berrada et al., Proc. Workshop on Physics with Antiprotons at LEAR in the ACOL Era, Editions Frontière 1985, eds U.Gastaldi, R.Klapisch, J.M.Richard, J.Tran Thanh Van, p. 33.

Bod 87 A.R. Bodmer and Q.N. Usmani, Nucl. Phys. *A463* (1987) 221c.

Bog 84a A.Bogaerts, M.Dehnert and J.Petersen, "DAS Users Guide", DD/OC/ND/MAN1, CERN 1984.

Bog 84a A.Bogaerts, M.Dehnert and J.Petersen, "DAS Reference Manual", DD/OC/ND/MAN2, CERN 1984.

Boh 70a G.Bohm et al., Nucl. Phys *B16* (1970) 46.

Boh 70b G.Bohm et al., Nucl.Phys. *B23* (1970) 93.

Bou 80 A.Bouyssy, Phys.Lett. *B91* (1980) 15.

Bre 79 A.Breskin et al., Nucl. Instr. Meth. *165* (1979) 125.

Bre 82 A.Breskin, Nucl. Instr. Meth. *196* (1982) 11.

Bre 86 T.Bressani, "Hadronic Physics at Intermediate Energy", Elsevier Science Publ. B.V. 1986, eds T.Bressani, R.A.Ricci, p. 259.

Brü 78 W.Brückner et al., Phys. Lett. *79B* (1978) 157.

Bur 88 A.J.Buras, Proc. Workshop on Physics at LEAR with Low Energy Antiprotons, Harwood Academic Publ. 1988, eds C.Amsler, G.Backenstoss, R.Klapisch, C.Leluc, D.Simon, L.Tauscher, p. 581.

Byc 84 A.S.Bychkov, Sov. J. Nucl. Phys. *40* (1984) 259.

Che 83 C.-Y.Cheung, D.P.Heddle and L.S.Kisslinger, Phys. Rev. *C27* (1983) 335.

Chr 88 R.E.Chrien, Nucl. Phys. *A478* (1988) 705c.

Clo 82 M.R.Clover et al.,Phys Rev. *C26* (1982) 2138.

Con 84 G.T.Condo, T.Handler and H.O.Cohn, Phys. Rev. C29 (1984) 1531.

Cug 84 J.Cugnon and J.Vandermeulen, Phys. Lett. *B146* (1984) 16.

Cug 85 J.Cugnon and J.Vandermeulen, Nucl. Phys. *A445* (1985) 717.

Cug 87a J.Cugnon, Nucl. Phys. *A462* (1987) 751.

Cug 87b J.Cugnon, P.Jasselette and J.Vandermeulen, Nucl. Phys. *A470* (1987) 558.

Dal 64 R.H.Dalitz, Proc. Intern. Conf. on Hyperfragments, CERN yellow rep. 64-1, 1964, p. 147.

Dor 86 S.Dore de Magalhães, Nucl. Instr. Meth. *A251* (1986) 134.

Dov 82 C.B.Dover and G.E.Walker, Phys. Rep. *89*, nr 1 (1982).

Dub 86 J.F.Dubach, Nucl. Phys. *A450* (1986) 71c.

Ead 71 W.T.Eadie et al., "Statistical Methods in Experimental Physics", North-Holland 1971.

Egi 87 T.von Egidy, Nature *328* (1987) 773.

Egi 88 T.von Egidy, Proc. Workshop on Physics at LEAR with Low Energy Antiprotons, Harwood Academic Publ. 1988, eds C.Amsler, G.Backenstoss, R.Klapisch, C.Leluc, D.Simon, L.Tauscher, p. 729.

Eya 78 Y.Eyal and H.Stelzer, Nucl. Instr. Meth. *155* (1978) 157.

Fla 83 V.Flaminio et al. (High Energy Reactions Analysis Group), "Compilation of cross-sections II: K^+ and K^- induced reactions", CERN-HERA 83-02, CERN 1983.

Fro 79 A.G.Frodesen, O.Skjeggestad and H.Tøfte, "Probability and Statistics in Particle Physics", Universitetsforlaget 1979.

Ghe 74 C.Ghesquière, Proc. Symp. on Antinucleon-Nucleon Interactions, CERN yellow report 74-18, 1974, p. 436.

Gil 79 F.J. Gilman and M.B.Wise, Phys. Rev. *D20* (1979) 2392.

Gra 85 R.Grace et al., Phys. Rev. Lett. *55* (1985) 1055.

Gra 86 R.Grace, "Weak Decay of P Shell Lambda Hypernuclei", Ph.D. dissertation, Carnegie Mellon University 1986.

Gua 88 C.Guaraldo, Proc. Workshop on Physics at LEAR with Low Energy Antiprotons, Harwood Academic Publ. 1988, eds C.Amsler, G.Backenstoss, R.Klapisch, C.Leluc, D.Simon, L.Tauscher, p. 797.

Har 79 D.von Harrach and H.J.Specht, Nucl. Instr. Meth. *164* (1979) 477.

Has 86 O.Hashimoto, Proc. 1986 INS Int. Symp. on Hypernuclear Physics, Toseisha Printing Co. 1986, eds H.Bandō, O.Hashimoto, K.Ogawa, p.196.

Hay 88 R.S.Hayano, Nucl. Phys. *A478* (1988) 113c.

Hed 86 D.P.Heddle and L.S.Kisslinger, Phys. Rev. *C33* (1986) 608.

Hsi 83 S.S.Hsiao and S.R.Cotanch, Phys. Rev. *C28* (1983) 1668.

Ilj 82 A.S.Iljinov, V.I.Nazaruk and S.E.Chigrinov, Nucl. Phys. *A382* (1982) 378.

Jan 82 J.F.Janni, Atomic Data and Nuclear Data Tables 27 (1982) 147.

Joh 80 T.Johansson, J.Konijn, S.Polikanov and G.Tibell, CERN / PSCC / 80 - 74.

Joh 84 T.Johansson, Proc. Workshop on Physics at LEAR with Low-Energy Cooled Antiprotons, Plenum Press 1984, eds U.Gastaldi and R.Klapisch, p. 589.

Jon 84 E.Jones, Proc. Workshop on Physics at LEAR with Low-Energy Cooled Antiprotons, Plenum Press 1984, eds U.Gastaldi and R.Klapisch, p. 5.

Kan 65 Y.W.Kang et al., Phys. Rev. *139* (1965) B401.

Key 73 G.Keyes et al., Nucl. Phys. *B67* (1973) 269.

Lag 64 J.P.Lagnaux et al., Nucl. Phys. *60* (1964) 97.

Lef 84 P.Lefèvre, Proc. Workshop on Physics at LEAR with Low-Energy Cooled Antiprotons, Plenum Press 1984, eds U.Gastaldi and R.Klapisch, p. 15.

Lef 85 P.Lefèvre, Proc. Workshop on Physics with Antiprotons at LEAR in the ACOL Era, Editions Frontière 1985, eds U.Gastaldi, R.Klapisch, J.M.Richard, J.Tran Thanh Van, p. 33.

Lit 80 U.Littmark and J.F.Ziegler, "Handbook of Ranges for Energetic Ions in All Elements", vol. 6 of "The Stopping and Ranges of Ions in Matter", ed. J.F.Ziegler, Pergamon Press 1980.

Man 83 M.A.Mandelkern et al.,Phys. Rev. *D27* (1983) 19.

McG 86 P.L.McGaughey et al., Phys. Rev. Lett. *56* (1986) 2156.

McK 84 B.H.J.McKellar and B.F.Gibson, Phys. Rev. *C30* (1984) 322.

McK 86 B.H.J.McKellar, Proc. 1986 INS Int. Symp. on Hypernuclear Physics, Toseisha Printing Co. 1986, eds H.Bandō, O.Hashimoto, K.Ogawa, p. 146.

Met 74 V.Metag et al., Nucl. Instr. Meth. *114* (1974) 445.

Met 80 V.Metag, D.Habs and H.J.Specht, Phys. Rep. *65*, nr. 1 (1980).

Miy 84 K.Miyano et al., Phys. Rev. Lett. *53* (1984) 1725.

Mos 86 E.F. Moser et al.,Phys. Lett. *B179* (1986) 25.

Meu 81 R.Meunier et al., Nucl. Instr. Meth. *186* (1981) 7.

Nie 76 K.J.Nield et al., Phys Rev. *C13* (1976) 1263.

Nog 86 V.I.Noga et al., Sov. J. Nucl. Phys. *43* (1986) 856.

Nog 88 V.I.Noga et al., Proc. Conf. on Nucleus-Nucleus Collisions, Saint-Malo 1988.

Nor 70 L.C.Northcliffe and R.F.Schilling, Nuclear Data Tables vol. *A7*, no 3-4 (1970) 233.

Ose 85 E.Oset and L.L.Salcedo, Nucl. Phys. *A443* (1985) 704.

Ose 86 E.Oset and L.L.Salcedo, Nucl. Phys. *A450* (1986) 371c.

Pei 83 A.Peisert, Nucl. Instr. Meth. *217* (1983) 229.

Phi 69 R.E.Phillips and J.Schneps, Phys. Rev. *180* (1969) 1307.

Pir 86 G.Piragino, "Hadronic Physics at Intermediate Energy", Elsevier Science Publ. B.V. 1986, eds T.Bressani, R.A.Ricci, p. 293.

Poe 77 D.N.Poenaru, Ann. Phys. *2* (1977) 133.

Pol 62 S.M.Polikanov et al., Sov. Phys. JETP *15* (1962) 1016.

Pov 87 B.Povh, Progr. in Part. Nucl. Phys. *18* (1987) 183.

Pov 88 B.Povh, Progr. in Part. Nucl. Phys. *20* (1988) 353.

Pre 64 R.J.Prem and P.H.Steinberg, Phys. Rev. *136* (1964) B1803.

Pre 86 W.H.Press et al., "Numerical recipes : the art of scientific computing", Cambridge University Press 1986.

Raf 80 J.Rafelski, Phys. Lett. *B91* (1980) 281.

Ric 74 P.Rice-Evans, "Spark, streamer, proportional and drift chambers", Richelieu Press 1974.

Ris 88 Ch.Ristori, CEN Grenoble, private communication.

Ros 88 A.S.Rosenthal et al., Ann. Phys. *184* (1988) 33.

Roy 75 J.Roy, Proc. IV Int. Symp. on Nucleon-Antinucleon Interactions, Syracuse 1975, p. III-1.

Sau 77 F.Sauli, "Principle of operation of multi-wire proportional and drift chambers", CERN yellow report 77-09, 1977.

Sch 66 H.W.Schmitt, J.H.Neiler and F.J.Walters, Phys. Rev. *141* (1966) 1146.

Sch 83 C.Schandera, C.Lauterbach and J.de Boer, Nucl. Instr. Meth. *217* (1983) 128.

Seg 77 E.Segrè, "Nuclei and particles", 2nd ed., Benjamin/Cummings 1977.

Sle 76 G.Sletten, V.Metag and E.Liukkonen, Phys. Lett. *B60* (1976) 153.

Ste 76 H.Stelzer, Nucl. Instr. Meth. *133* (1976) 409.

Spe 72 H.J.Specht et al., Phys. Lett. *B41* (1972) 43.

Spe 88 J.Speth (editor), Proc. Int. Symp. on Strangeness in Hadronic Matter, Nucl. Phys. *A479* (1988).

Szy 87 J.J.Szymanski, "The Weak Decay of Lambda Hypernuclei", Ph.D. dissertation, Carnegie Mellon University 1987.

Van 73 R.Vandenbosch and J.R.Huizenga, "Nuclear Fission", Academic Press 1973.

Wal 88 T.Walcher, Nucl. Phys. *A479* (1988) 63c.

Yam 87 T.Yamazaki, Nucl. Phys. *A463* (1987) 39c.

Zie 80 J.F.Ziegler, "Handbook of Stopping Cross-Sections for Energetic Ions in All Elements", vol. 5 of "The Stopping and Ranges of Ions in Matter", ed. J.F.Ziegler, Pergamon Press 1980.

Zie 85 J.F.Ziegler, J.P.Biersack and U.Littmark, "The Stopping and Range of Ions in Solids", vol. 1 of "The Stopping and Ranges of Ions in Matter", ed. J.F.Ziegler, Pergamon Press 1985.

ACTA UNIVERSITATIS UPSALIENSIS

Uppsala Dissertations from the Faculty of Science

Editor: The Dean of the Faculty of Science

1–6: 1970–1973

7. *Tor Löfgren:* The Interval Condition. A new condition governing atomic parameters and F phases. A structure determination according to the "*B* method". 1974.
8. *Hedvig von Bahr-Lindström:* Human Immunoglobulin E. Structural Studies on the Epsilon Chain ND. 1974.
9. *Sverker Norrby:* Association and Shear Dissociation of Carboxy-Ended Polystyrene in Dilute Solution. 1975.
10. *Kaluba Mwansa Chitumbo:* Sorption and Diffusion in Dilute Cellulosic Networks. 1975.
11. *Bo Jägersten:* 3-substituerade 5-nitrofuraner. Syntes, antimikrobiella effekter och omlagring till pyridazoner. 1975.
12. *Lars Thofelt:* Studies on leaf temperature recorded by direct measurement and by thermography. 1975.
13. *Monica Henricsson:* Nutritional studies on Chara globularis Thuill., Chara zeylanica Willd., and Chara haitensis Turpin. 1976.
14. *Göran Kloow:* Studies on Regenerated Cellulose by the Fluorescence Depolarization Technique. 1976.
15. *Carl-Magnus Backman:* A High Pressure Study of the Photolytic Decomposition of Azoethane and Propionyl Peroxide. 1976.
16. *Lennart Källströmer:* The significance of biotin and certain monosaccharides for the growth of Aspergillus niger on rhamnose medium at elevated temperature. 1977.
17. *Staffan Renlund:* Identification of Oxytocin and Vasopressin in the Bovine Adenohypophysis. 1978.
18. *Bengt Finnström:* Effects of pH, Ionic Strength and Light Intensity on the Flash Photolysis of L-tryptophan. 1978.
19. *Thomas C. Amu:* Diffusion in Dilute Solutions: An Experimental Study with Special Reference to the Effect of Size and Shape of Solute and Solvent Molecules. 1978.
20. *Lars Tegnér:* A Flash Photolysis Study of the Thermal Cis–Trans Isomerization